

A hybrid model of the proton structure functions

S. A. Kulagin*

Institute for Nuclear Research of the Russian Academy of Sciences, Moscow 117312, Russia

V. V. Barinov†

*Physics Department, M. V. Lomonosov Moscow State University,
Leninskie Gory, Moscow 119991, Russia and*

Institute for Nuclear Research of the Russian Academy of Sciences, Moscow 117312, Russia

Abstract

We develop a “hybrid” model of the proton inelastic structure functions applicable for a wide region of invariant masses of produced states W and invariant momentum transfer Q including deep inelastic scattering (DIS), nucleon resonance production as well as the region close to inelastic threshold. In the DIS region, we compute the structure functions in terms of the parton distributions together with higher-twist corrections which are determined from a global QCD fit. The resonant part is addressed in terms of the Breit-Wiegner contributions from five states: $\Delta(1232)$ resonance, $N(1440)$ Roper resonance, and three effective resonances describing the second and third resonance regions. The couplings of the nucleon resonances to photon are described in terms of helicity amplitudes. The nonresonant background is treated in terms of a smooth extrapolation of the DIS structure functions to low- W and low- Q values with a proper inelastic threshold behavior and the real photon limit $Q^2 = 0$ constrained by the photoproduction data. We independently treat the transverse, F_T , and the longitudinal, F_L , structure function and fix the model parameters from a global analysis of the electron-proton differential cross section data together with data on the total photoproduction cross section. We demonstrate a very good performance of the model by comparing our predictions with data on cross sections and the structure functions F_2 and $R = F_L/F_T$ in the resonance and the DIS region.

* kulagin.physics@gmail.com

† barinov.vvl@gmail.com

I. INTRODUCTION

Deep inelastic scattering (DIS) at high invariant momentum transfer $Q \gg 1$ GeV is successfully described in terms of QCD framework of the operator product expansion (OPE) together with renormalization group equations. The proton structure functions (SF) in this region are driven by the parton distribution functions (PDFs) supplemented by higher-twist (HT) power corrections whose impact increases as the scale Q decreases. PDFs together with HT corrections are determined from global QCD analyses of a wide set of high-energy data (for more detail see recent reviews [1, 2]).

However, available QCD methods based on OPE as well as perturbative analysis fail at low scale $Q \lesssim 1$ GeV. In addition, if the invariant mass of produced states $W < 2$ GeV the nucleon inelastic scattering is dominated by the production of resonant states. Unlike the DIS region, the resonance region is usually addressed in terms of hadronic degrees of freedom. Starting from Ref.[3] a number of phenomenological analyses are available in which the resonance production is considered as a superposition of the Breit-Wiegner poles and the resonance couplings are described in terms of helicity amplitudes [4–6] (for a recent review see Ref.[7]). Along with the resonance production, the inelastic scattering is accompanied by non-resonant background processes whose contribution is rising with W . The background is treated either empirically [5] or using effective meson-nucleon model [4]. The region of applicability of the cross section and structure function models inferred from these approaches is limited to the values of Q^2 and W^2 up to a few GeV².

In this study we develop a combined (“hybrid”) quantitative model for the proton transverse (F_T) and longitudinal (F_L) SF spanning both the nucleon resonance and DIS region. In the DIS region our model is based on the PDFs and HT terms determined from the global QCD fit [8, 9], which was performed with particular emphasis on a low- Q region. The nucleon resonance region is addressed in terms of five Breit-Wiegner states, $\Delta(1232)$ resonance, $N(1440)$ Roper resonance, and three more heavy states describing the second and the third resonance regions. It should be commented in this context that there are many excited nucleon resonance states contributing to inclusive inelastic cross section. A detailed treatment of all those states goes beyond the scope of this study. For the sake of describing the observed resonance picture of inclusive spectra, we treat the resonances heavier than $\Delta(1232)$ state not as physical particles but rather as effective Breit-Wiegner resonances which incorporate contributions from many physical states. Nevertheless, we assign them the particle quantum numbers, such as spin and mass, and describe their couplings to photons in terms of helicity amplitudes.

The nonresonant background is computed in terms of the DIS structure functions properly continued into a low- Q and low- W region. The background for F_T match smoothly the real photon limit at $Q^2 = 0$ which is constrained by data on the total photoproduction cross section. For F_L our extrapolation method provides vanishing $R = F_L/F_T$ in the real photon limit. We also ensure the background contributions to smoothly vanish at the inelastic production threshold $W_{\text{th}}^2 = (M + m_\pi)^2$ with M and m_π the proton and the pion mass, respectively. On the other hand, our extrapolation model for F_T and F_L matches smoothly the corresponding DIS SF at a scale Q_0 which is determined from analysis of data.

The parameters of our model, such as the resonance masses, widths, parameters of helicity amplitudes, the transition scale factor Q_0 , are determined from a global fit to the combined data on the electron-proton inelastic differential cross section and the total photoproduction cross section. We then verify our model by comparing our predictions for F_2 and R with the

corresponding measurements from various experiments.

The article is organized as follows. In Sec. II we outline the basic framework for the cross sections and SF to be used in further analysis, in Sec. II A we summarize our model for the DIS SF while in Sec. II B we address the resonance SF in terms of the Breit-Wiegner poles and helicity amplitudes. In Sec. III we discuss in detail our model of the resonance and background contributions. In Sec. IV we describe the details of data analysis. Our results and observations are discussed in Sec. V, in Sec. VI we summarize. Section A provides a detailed comparison of our predictions with cross section data from various experiments used in our analysis.

II. FRAMEWORK

The scattering of charged leptons by hadrons in the leading order in the electromagnetic coupling constant $\alpha = e^2/(4\pi)$ is determined by the standard one-photon exchange process. In inclusive scattering, the final hadronic state is not detected and the differential cross section is given by hadronic tensor $W_{\mu\nu}$ (see, *e.g.*, [10]):

$$W_{\mu\nu}(p, q) = \frac{1}{8\pi} \sum_{\lambda, n} (2\pi)^4 \delta(p + q - p_n) \langle P, \lambda | J_\mu^{\text{em}}(0) | n \rangle \langle n | J_\nu^{\text{em}}(0) | P, \lambda \rangle, \quad (1)$$

where J_μ^{em} is the electromagnetic current, the sum is taken over all final hadronic states n , and p is the proton four-momentum and q is four-momentum transfer. We do not consider the polarization effects and explicitly average over proton polarization λ . Only the symmetric part of the hadronic tensor contributes to the spin-averaged cross section. Because of the current conservation, time reversal invariance and parity conservation, the symmetric hadronic tensor has only two independent Lorentz structures which are usually written as follows

$$W_{\mu\nu}(p, q) = \left(\frac{q_\mu q_\nu}{q^2} - g_{\mu\nu} \right) F_1 + \frac{F_2}{p \cdot q} \left(p_\mu - q_\mu \frac{p \cdot q}{q^2} \right) \left(p_\nu - q_\nu \frac{p \cdot q}{q^2} \right), \quad (2)$$

where $F_{1,2}$ are the Lorentz-invariant dimensionless structure functions.¹ The structure functions depend on two independent Lorentz-invariant variables. In DIS region, the Bjorken variable $x = Q^2/(2p \cdot q)$ and the four-momentum transfer squared $Q^2 = -q^2$ are usually used. In the discussion of the resonance and a transition region, we will also consider the structure functions as a function of the invariant mass of produced states

$$W^2 = M^2 + Q^2 (1/x - 1). \quad (3)$$

The differential cross section in terms of x and Q^2 is as follows

$$\frac{d^2\sigma}{dx dQ^2} = \frac{4\pi\alpha^2}{xQ^4} \left[xy^2 \left(1 - \frac{2m_l^2}{Q^2} \right) F_1 + \left(1 - y - \frac{M^2 x^2 y^2}{Q^2} \right) F_2 \right], \quad (4)$$

where m_l is the lepton mass and $y = p \cdot q/p \cdot k$ is inelasticity parameter (here k is the four-momentum of incoming lepton). The variable y is not independent but related to x and

¹ We use the following normalization $\langle p|p' \rangle = 2E_{\mathbf{p}}(2\pi)^3 \delta(\mathbf{p} - \mathbf{p}')$ for both the boson and the fermion states.

Q^2 as $xy = Q^2/(2p \cdot k)$. In the laboratory frame, the differential cross section is measured as a function of scattering angle and the outgoing lepton energy E' and related to Eq.(4) as

$$\frac{d^2\sigma}{d\Omega dE'} = \frac{x E'}{\pi y} \frac{d^2\sigma}{dx dQ^2}. \quad (5)$$

The structure functions $F_{1,2}$ can be related to the virtual photon helicity cross sections by projecting the hadronic tensor onto the photon polarization vectors of definite helicity $m = \pm 1, 0$. It is convenient to chose the z -axis along the momentum transfer, $q_z = |\mathbf{q}|$. Then we have

$$\varepsilon^{(\pm 1)} = (0, 1, \pm i, 0)/\sqrt{2}, \quad (6a)$$

$$\varepsilon^{(0)} = (q_z, \mathbf{0}_\perp, q_0)/Q. \quad (6b)$$

where $Q = \sqrt{Q^2}$. The polarization vectors $\varepsilon^{(+1)}$ and $\varepsilon^{(-1)}$ describe two transversely polarized states with helicity $m = +1$ and $m = -1$, while the vector $\varepsilon^{(0)}$ corresponds to the longitudinally polarized virtual photons. Note that the polarization vectors $\varepsilon^{(m)}$ are orthogonal to the photon momentum, $\varepsilon^{(m)} \cdot q = 0$, and normalized as $\varepsilon^{(0)} \cdot \varepsilon^{(0)} = 1$ and $\varepsilon^{(m)*} \cdot \varepsilon^{(m)} = -1$ for $m = \pm 1$, where ε^* is the complex conjugate. The transverse, F_T , and the longitudinal, F_L , SF are

$$F_T = x \sum_{m=\pm 1} \varepsilon^{(m)\mu*} W_{\mu\nu} \varepsilon^{(m)\nu} = 2xF_1, \quad (7)$$

$$F_L = 2x \varepsilon^{(0)\mu*} W_{\mu\nu} \varepsilon^{(0)\nu} = \gamma^2 F_2 - F_T, \quad (8)$$

where $\gamma^2 = 1 + 4x^2 M^2/Q^2$. The transverse and longitudinal cross sections in terms of Eq.(7) and (8) can be written as follows (see, *e.g.*, Ref.[10])

$$\sigma_{T,L} = \frac{4\pi^2\alpha F_{T,L}}{(1-x)Q^2}. \quad (9)$$

Note that the definition of the virtual photon flux is somewhat uncertain. In Eq.(9) we assume the virtual photon flux equals the real photon one with the condition that the mass of produced hadronic states W is the same for the real and virtual photon.

Let us briefly discuss the real photon limit. It is convenient to consider the SF as a function of W^2 and Q^2 . At $Q^2 = 0$ the longitudinal cross section vanish. This in turn suggests F_L to vanish faster than Q^2 as $Q^2 \rightarrow 0$. On the other hand, the cross section σ_T for transverse virtual photons goes to the total photo-production cross section in this limit:

$$\sigma_\gamma(W) = 4\pi^2\alpha \lim_{Q^2 \rightarrow 0} F_T(W^2, Q^2)/Q^2. \quad (10)$$

For this reason, the ratio $F_T(W^2, Q^2)/Q^2$ (as well as the ratio F_2/Q^2) is finite in the real photon limit and driven by the photo-production cross section. We will use this observation to constrain a low- Q behavior of our model in Sec. III.

A. Deep inelastic scattering region

In the region $W > 2$ GeV and $Q > 1$ GeV, which is referred to as deep-inelastic scattering (DIS), the cross section is driven by scattering off quasi-free (anti)quarks in hadrons described

by the parton distribution functions (PDFs). In QCD, a common framework to describe DIS is the operator product expansion (OPE), a procedure producing the power series in Q^{-2} (twist expansion). In the first order, i.e. in the leading twist (LT), SFs are fully determined by the parton distribution functions (PDFs). The power corrections can be of two different types: (i) contributions from higher-twist (HT) operators describing quark-gluon correlations and (ii) correction arising from a finite nucleon mass (target mass correction, or TMC). Summarizing, we write the proton SF as follows

$$F_i^{\text{DIS}}(x, Q^2) = F_i^{\text{TMC}}(x, Q^2) + H_i(x)Q^{-2} + O(Q^{-4}), \quad (11)$$

where $i = T, L$ and the superscript TMC labels the LT SF corrected for the target mass effects and the functions H_i describe the dynamical twist-4 contribution (for brevity, we suppress explicit notation to the twists higher than 4).

The PDFs are usually determined in a global QCD analysis of high-energy data including DIS, muon pair production in proton-proton collisions (DY), W boson production at colliders. In this study we use the proton PDFs from a global QCD fit of Ref.[8, 9], which was performed to the next-to-next-to-leading-order (NNLO) approximation in QCD coupling constant. It should be noted that an updated analysis is available [11], as well as the results of other PDF analyses (see, *e.g.*, discussion in Ref.[1]). However, in this study we use the results of Ref.[8, 9] as the base, as that analysis emphasizes a low- Q region. The fit of Ref.[8, 9] utilized the cuts $Q^2 > 2.5 \text{ GeV}^2$ and $W > 1.8 \text{ GeV}$, however the SF of Ref.[8, 9] are available at significantly lower values of Q^2 owing the extrapolation procedure.

Along with PDFs the analysis of Ref.[8, 9] provides the determination of HT terms. In order to account for TMC, we follow Ref.[12]. It should be remarked, that TMC procedure of Ref.[12] violates the inelastic threshold behavior of SF leading to nonzero values at $x = 1$ (see, *e.g.*, discussion in Ref.[13]). The region of large Bjorken x corresponds to low values of W . Therefore, by increasing x at some point we leave DIS region even at high values of Q^2 . At practice, since we use the DIS SF for $W > 2 \text{ GeV}$ we do not run into the threshold problem. In Sec. III we discuss an extrapolation of the DIS structure functions into a low- W region respecting the inelastic threshold behavior (see also Ref.[14]).

B. Excitation of nucleon resonances

At low energy $W < 2 \text{ GeV}$ and low momentum transfer $Q \lesssim 2 \text{ GeV}$ the inelastic cross section is dominated by excitation of nucleon resonance states. Resonant contributions to hadronic tensor Eq.(1) can be written as

$$W_{\mu\nu}^{\text{Res}} = \frac{1}{4} \sum_{R, \lambda, \lambda'} \delta(W^2 - M_R^2) \langle P, \lambda | J_\mu^{\text{em}}(0) | R, \lambda' \rangle \langle R, \lambda' | J_\nu^{\text{em}}(0) | P, \lambda \rangle, \quad (12)$$

where the sum is taken over the resonance states and M_R is the mass of the state R . For the moment we consider narrow resonance states with zero width, the effect of a finite width will be discussed below. In Eq.(12) we also explicitly sum over the polarization λ' of the intermediate state.

The contribution to F_T and F_L from the given resonance state R is given by contracting the hadronic tensor (12) with photon polarization vector $\varepsilon^{(m)}$. The corresponding matrix elements can be described in terms of the helicity amplitudes [3, 7, 15]:

$$\langle R, h' | \varepsilon^{(m)} \cdot J^{\text{em}}(0) | P, h \rangle = H_{h'h}^m, \quad (13)$$

where h' and h are the helicities of the resonance state and the proton, respectively. As the helicity conserves, $h' = h + m$. In the parity transformation the helicity changes its sign, and, because of symmetry under parity transformation, we have the relation $H_{-h'-h}^{-m} = H_{h'h}^m$ (see also Ref.[3]). We consider the helicity amplitudes in the center-of-mass frame (CM) and chose the spin quantization axis along the photon momentum. Then the proton helicity h has the sign opposite to its polarization, as the proton momentum balances the photon momentum, and the helicity of the intermediate resonance state h' corresponds to its polarization.

Consider Eq.(13) for the proton polarization $\lambda = 1/2$ and respectively $h = -1/2$. The helicity amplitudes can be related to the standard electrocouplings $A_{1/2}$, $A_{3/2}$ and $S_{1/2}$, which are commonly used to describe electroexcitation of the resonance states (see, *e.g.*, Ref.[7]):

$$H_{\frac{1}{2}, -\frac{1}{2}}^{+1} = c_R A_{1/2}(Q^2), \quad (14)$$

$$H_{-\frac{3}{2}, -\frac{1}{2}}^{-1} = c_R A_{3/2}(Q^2), \quad (15)$$

$$H_{-\frac{1}{2}, -\frac{1}{2}}^0 = c_R S_{1/2}(Q^2)(Q/|\mathbf{q}|_{\text{CM}}), \quad (16)$$

where $|\mathbf{q}|_{\text{CM}}$ is the photon momentum in the CM frame.² The normalization factor c_R can be determined by requiring the electromagnetic decay width of the resonance $R \rightarrow P\gamma$ to be [7, 16]

$$\Gamma(R \rightarrow P\gamma) = \frac{2K_R^2 M}{\pi(2S_R + 1)M_R} (|A_{1/2}^R(0)|^2 + |A_{3/2}^R(0)|^2), \quad (17)$$

where we assume the averaging over the resonance polarization and sum over the photon polarization, S_R is the resonance spin, $K_R = (M_R^2 - M^2)/(2M_R)$ is the energy of a real photon in the CM frame needed to produce the state with the mass M_R . Using Eq.(14) and (15) we have

$$c_R^2 = \frac{M(M_R^2 - M^2)}{\pi\alpha}. \quad (18)$$

Note that the electromagnetic current in Eq.(1) is normalized for the electric charge $e = 1$. The electric charge is absorbed in the amplitudes $A_{1/2}$, $A_{3/2}$, $S_{1/2}$, and for that reason we have α in the denominator in Eq.(18).

We now apply the results of the present discussion to compute the resonant contribution to F_T and F_L in terms of the amplitudes $A_{1/2}$, $A_{3/2}$ and $S_{1/2}$. From Eq.(7) and (8) we have

$$F_T^{\text{Res}} = \frac{xM}{2\pi\alpha} \sum_R \delta(W^2 - M_R^2)(M_R^2 - M^2) (|A_{1/2}^R(Q^2)|^2 + |A_{3/2}^R(Q^2)|^2), \quad (19)$$

$$F_L^{\text{Res}} = \frac{xM}{\pi\alpha} \sum_R \delta(W^2 - M_R^2)(M_R^2 - M^2) \frac{Q^2}{|\mathbf{q}|_{\text{CM}}^2} |S_{1/2}^R(Q^2)|^2, \quad (20)$$

where x is the Bjorken variable and the sum is taken over the resonance states.

We now discuss the effect of finite resonance width in Eq.(12) in some more detail. Following a traditional approach, we replace $\delta(W^2 - M_R^2)$ with the standard Breit-Wigner factor:

$$\delta(W^2 - M_R^2) \rightarrow \frac{1}{\pi} \frac{M_R \Gamma_R}{(W^2 - M_R^2)^2 + M_R^2 \Gamma_R^2}, \quad (21)$$

² Note also, that in the CM frame $|\mathbf{q}|_{\text{CM}}$ is the magnitude of the proton momentum. For completeness, $|\mathbf{q}|_{\text{CM}}^2 = E_{\text{CM}}^2 - M^2$, where $E_{\text{CM}} = (W^2 + Q^2 + M^2)/(2W)$ is the proton CM energy.

where Γ_R is the resonance total width. At practice, we will assume that the width Γ_R is saturated by contributions from single-meson decay modes ($R \rightarrow \pi N$ and $R \rightarrow \eta N$) and two-pion decay $R \rightarrow 2\pi N$:

$$\Gamma_R = \beta_R^\pi \Gamma_R^\pi + \beta_R^\eta \Gamma_R^\eta + \beta_R^{2\pi} \Gamma_R^{2\pi}, \quad (22)$$

where $\beta_R^{\pi,\eta,2\pi}$ are the corresponding branching fractions.

Generally, the resonances can be excited off the resonance pole, $W^2 \neq M_R^2$, and in Eq.(12) one has to consider off-mass-shell effects on the resonance parameters. In particular, the resonance width becomes a function of W , $\Gamma_R = \Gamma_R(W)$. Indeed, near the inelastic threshold $W_{\text{th}} = M + m_\pi$ the cross section should vanish that in turn requires vanishing resonance width. On the other hand, $\Gamma_R(W)$ increases with W as the phase space available for the resonance decay increases. In order to account for this effect, we parameterize the energy dependence of $\Gamma_R(W)$ following Ref.[3]:

$$\Gamma_R^\pi = \Gamma_R^0 \left(\frac{p_\pi(W)}{p_\pi(M_R)} \right)^{2L+1} \left(\frac{p_\pi(M_R)^2 + X_R^2}{p_\pi(W)^2 + X_R^2} \right)^L, \quad (23)$$

where Γ_R^0 is intrinsic resonance width, $p_\pi(W)$ is the meson CM momentum in the decay $R \rightarrow \pi P$ of the resonance with mass W , L is angular momentum of the resonance, and X_R is a phenomenological parameter (damping factor). The parametrization of the η decay mode is similar to Eq.(23) with p_η the η meson CM momentum. For the 2π decay mode we use [7]

$$\Gamma_R^{2\pi} = \Gamma_R^0 \left(\frac{p_{2\pi}(W)}{p_{2\pi}(M_R)} \right)^{2L+4} \left(\frac{p_{2\pi}(M_R)^2 + X_R^2}{p_{2\pi}(W)^2 + X_R^2} \right)^{L+2}, \quad (24)$$

where $p_{2\pi}$ is effective two-pion momentum in CM frame which is computed similar to p_π but replacing m_π with $2m_\pi$. Apparently, $p_{2\pi} = 0$ below 2π production threshold and, respectively, $p_\eta = 0$ below the η production threshold.

Also the γPR vertex, or helicity amplitudes, acquire W dependence in the resonance off-pole region. It should be commented that the off-shell continuation is somewhat uncertain. Indeed, in the right side of Eq.(19) and (20) M_R can be replaced with W and then the factor $W^2 - M^2$ can be taken out of the sum over the resonance states. However, this operation does not commute with Eq.(21) and then the result would depend on the order of these operations. Keeping this in mind we phenomenologically account for the off-shell effect following Ref.[3] with the factor f_R^γ :

$$f_R^\gamma(W) = \frac{K^2 K_R^2 + X_R^2}{K_R^2 K^2 + X_R^2}, \quad (25)$$

where $K = K(W) = (W^2 - M^2)/(2W)$ is the equivalent photon CM momentum, $K_R = K(M_R)$ and X_R is the same damping parameter as in Eq.(23) and (24). At the resonance pole $f_R^\gamma(M_R) = 1$.

Summarizing, we have for the resonant contribution to F_T and F_L :

$$F_T^{\text{Res}} = \frac{xM}{\pi^2\alpha} \sum_R \frac{M_R^2 \Gamma_R K_R f_R^\gamma(W)}{(W^2 - M_R^2)^2 + M_R^2 \Gamma_R^2} (|A_{1/2}(Q^2)|^2 + |A_{3/2}(Q^2)|^2), \quad (26)$$

$$F_L^{\text{Res}} = \frac{2xM}{\pi^2\alpha} \frac{Q^2}{|\mathbf{q}|_{\text{CM}}^2} \sum_R \frac{M_R^2 \Gamma_R K_R f_R^\gamma(W)}{(W^2 - M_R^2)^2 + M_R^2 \Gamma_R^2} |S_{1/2}(Q^2)|^2, \quad (27)$$

where we sum over the resonance states and $\Gamma_R = \Gamma_R(W)$ is the total resonance width by Eq.(22). For completeness we also present the corresponding contributions to the virtual photon cross section σ_T and σ_L by Eq.(9). Using Eq.(26) and (27) and also the relation $Q^2(1-x) = x(W^2 - M^2)$ we have

$$\sigma_T^{\text{Res}} = \frac{2M}{W} \sum_R \frac{M_R^2 \Gamma_R(K_R/K) f_R^\gamma(W)}{(W^2 - M_R^2)^2 + M_R^2 \Gamma_R^2} (|A_{1/2}(Q^2)|^2 + |A_{3/2}(Q^2)|^2), \quad (28)$$

$$\sigma_L^{\text{Res}} = \frac{4M}{W} \frac{Q^2}{|\mathbf{q}|_{\text{CM}}^2} \sum_R \frac{M_R^2 \Gamma_R(K_R/K) f_R^\gamma(W)}{(W^2 - M_R^2)^2 + M_R^2 \Gamma_R^2} |S_{1/2}(Q^2)|^2. \quad (29)$$

The explicit parameterization of the Q^2 dependence of the helicity amplitudes entering Eq.(26) to (29) is discussed in Sec. III.

III. DESCRIPTION OF THE MODEL

The full structure functions include contributions from both, the resonance states discussed in Sec. II B, and the continuum states produced non-resonantly [background contributions (BG)]:

$$F_i = F_i^{\text{Res}} + F_i^{\text{BG}}, \quad (30)$$

where $i = T, L$. In what follows it will be convenient to consider the structure functions as a function of Q^2 and W^2 . From Eq.(3) the Bjorken variable $x = Q^2/(Q^2 + W^2 - M^2)$. While the resonance part dominates in the region of low W , the BG contribution rises with W and prevails for $W > 2$ GeV. If W and Q are sufficiently high then the BG contributions are driven by DIS, $F_i^{\text{BG}} = F_i^{\text{DIS}}$. We will use this simple observation to also model the BG contributions in the whole region of W and Q with suitable extrapolation of the DIS structure functions outside the region of their applicability.

A. Resonance contributions

We first consider the resonant contributions and apply Eq.(26) and (27) in order to compute the contribution to the transverse and the longitudinal structure functions. Note that the unpolarized scattering is not sensitive to individual amplitudes $A_{1/2}$ and $A_{3/2}$ and only their sum in quadrature is relevant. For this reason, for each of the resonance state in Eq.(26) and (27), we will discuss the average amplitude $A(Q^2)$ defined as

$$|A(Q^2)|^2 = |A_{1/2}(Q^2)|^2 + |A_{3/2}(Q^2)|^2. \quad (31)$$

In our model, in order to describe the observed resonant picture of inclusive spectra, we include five resonant contributions in Eq.(26) and (27). The first resonance region is described by a well separated $\Delta(1232)$ state. The second and third resonance regions are described in terms of $N(1440)$ Roper resonance and three more heavier states R_1 , R_2 , and R_3 . As outlined in Sec. I, we treat these states as effective Breit-Wigner resonances incorporating contributions from many physical excited-nucleon states. The relevant resonance parameters are listed in Table I. The parameter values (the standard deviation is listed in parenthesis) are determined from a fit to the hydrogen inclusive differential cross-section data together with photoproduction data, as described in Sec. IV.

TABLE I. The best fit values (uncertainty in per cent shown in parentheses) for the mass M_R , the intrinsic width Γ_R , the angular momentum L , the damping parameter X and the decay branching fractions β for each of the resonant state. The dimensional parameters are in GeV units. The estimate of standard deviation on each of the parameters is given in parenthesis.

	M_R	Γ_R	L	X	$\beta_{1\pi}$	$\beta_{2\pi}$	β_η
$\Delta(1232)$	1.2254(0.015)	0.1136(0.532)	1	0.0710(1.561)	1.00	0.00	0.00
$N(1440)$	1.4265(0.146)	0.3498(1.576)	1	0.0264(5.599)	0.65	0.35	0.00
R_1	1.5127(0.021)	0.1012(1.543)	2	1.2103(9.609)	0.75	0.25	0.00
R_2	1.5337(0.082)	0.3562(1.506)	0	0.2444(2.692)	0.15	0.85	0.00
R_3	1.6992(0.022)	0.1119(1.383)	2	0.3464(6.422)	0.15	0.60	0.25

In order to parameterize the Q^2 dependence of the transverse and the longitudinal amplitudes in Eq.(26) and (27), we use the following model:

$$A(Q^2) = (a_1 + a_2 Q^2) / (1 + a_3 Q^2)^{a_4} \quad (32)$$

$$S_{1/2}(Q^2) = (c_1 + c_2 Q^2) \exp(-c_3 Q^2) \quad (33)$$

The determination of the parameters a_i , c_i , as well as other model parameters entering Eq.(26) and (27), will be discussed in Sec. IV.

B. Background contributions

In the discussion of the BG contributions we first consider the extrapolation of the DIS structure functions to low Q^2 . Note that the pQCD framework of Sec. II A applies at $Q > Q_0$, where the scale $Q_0 \sim 1$ GeV. Going into the region $Q < Q_0$, we make use of the constrains on low- Q behavior of F_T and F_L at $Q^2 \rightarrow 0$ (see discussion after Eq.(9)). In what follows we consider extrapolation of F_T and F_L from the scale Q_0^2 down to $Q^2 = 0$. Let us first discuss the function F_T which vanishes as Q^2 as $Q^2 \rightarrow 0$. From Eq.(10) we conclude that the ratio F_T/Q^2 in the photon limit $Q^2 \rightarrow 0$ is driven by the total photoproduction cross section $\sigma_\gamma(W^2)$. Taking this into account, we consider the following model interpolating between $Q^2 = 0$ and Q_0^2 (for Q^2 we use a more handy notation t):

$$F_T^{\text{Ext}}(W^2, t) = f_0 t + f_1 t^m + f_2 t^n, \quad (34)$$

where f_0 , f_1 and f_2 are the functions of W , and we assume $m > 1$ and $n > 1$. Taking the limit $t \rightarrow 0$ we have

$$f_0(W) = \sigma_\gamma(W)/(4\pi^2\alpha), \quad (35)$$

where $\sigma_\gamma(W)$ is the total photo-production cross section corresponding to the mass W of the produced hadronic states. The functions f_1 and f_2 are determined from a requirement that Eq.(34) smoothly match the DIS structure function F_T^{DIS} by Eq.(11) at $t = t_0 = Q_0^2$, *i.e.* we require continuity of the function and its derivative at the matching point. We have

$$f_1 = t_0^{-m} (n F_T^{\text{DIS}} - t_0 \partial_t F_T^{\text{DIS}} - (n-1) f_0 t_0) / (n-m), \quad (36)$$

$$f_2 = t_0^{-n} (m F_T^{\text{DIS}} - t_0 \partial_t F_T^{\text{DIS}} - (m-1) f_0 t_0) / (m-n), \quad (37)$$

where F_T^{DIS} and its derivative $\partial_t F_T^{\text{DIS}}$ are computed at $t = t_0$ for given W^2 . The exponents m and n controlling transition to low- t region are adjusted from data analysis in Sec. IV. Note Eq.(36) and (37) have the pole at $n = m$. However, Eq.(34) is finite in the limit $n \rightarrow m$. Taking this limit we see that a low- t behavior is given by a combination of t^m and $t^m \ln t$ terms, and Eq.(34) can be written as follows:

$$F_T^{\text{Ext}} = f_0 t + \left(\frac{t}{t_0}\right)^m \left[F_T^{\text{DIS}} - f_0 t_0 + (m F_T^{\text{DIS}} - t_0 \partial_t F_T^{\text{DIS}} - (m-1) f_0 t_0) \ln \frac{t_0}{t} \right]. \quad (38)$$

At practice this is an important case preferred by data as described in Sec. IV.

In order to extrapolate the longitudinal SF in the region $0 < t < t_0$ we use a model similar to Eq.(34) with $f_0 = 0$ as the longitudinal cross section vanishes for real photon:

$$F_L^{\text{Ext}}(W^2, t) = f'_1 t^{m'} + f'_2 t^{n'}. \quad (39)$$

The functions $f'_{1,2}(W)$ are fixed from the condition of smoothness of the function Eq.(39) at $t = t_0$, similar to F_T case. On the functions f'_1 and f'_2 we obtain the equations similar to Eq.(36) and (37) with F_T replaced with F_L and $f_0 = 0$. The case $n' = m'$, which is preferred by data in our analysis from Sec. IV, is given by equation

$$F_L^{\text{Ext}} = \left(\frac{t}{t_0}\right)^{m'} \left[F_L^{\text{DIS}} + (m' F_L^{\text{DIS}} - t_0 \partial_t F_L^{\text{DIS}}) \ln \frac{t_0}{t} \right]. \quad (40)$$

In Sec. IV we use Eq.(38) and (40) with the exponents m and m' adjusted from a fit to differential cross section data.

Note that in global QCD fits the PDFs are parameterized in the full region of Bjorken $0 < x < 1$ and for this reason the DIS structure functions by Eq.(11) can be computed in the full region of W . However, for $W < 2$ GeV, and therefore in the region of large x , the structure functions are not directly constrained by data as the PDFs fits apply the cut on W from below ($W > 1.8$ GeV in Ref.[8, 11]). We also recall that, as discussed in Sec. II A, the target mass correction of Ref.[12] violates the threshold behavior at $x \rightarrow 1$. Taking these into account we introduce a correction factor and model the BG contribution to structure functions in the full kinematic range of W^2 and Q^2 as follows

$$F_i^{\text{BG}}(W^2, Q^2) = B_i(W^2) \begin{cases} F_i^{\text{DIS}}(W^2, Q^2), & \text{for } Q^2 \geq Q_0^2, \\ F_i^{\text{Ext}}(W^2, Q^2), & \text{for } Q^2 < Q_0^2, \end{cases} \quad (41)$$

where $i = T, L$ and F_T^{Ext} and F_L^{Ext} are given by Eq.(34) and (39). The functions B_T and B_L are responsible for extrapolation of the corresponding DIS SF to low W^2 region. These functions are positively defined and have the following properties. They vanish at the pion production threshold $W \rightarrow M + m_\pi$. On the other hand, they rise with W and $B_{T,L} \rightarrow 1$ above the resonance region. In order to respect this requirement, we use the following model

$$B = 1 - \exp(-b_1(W^2 - W_{\text{th}}^2)^{b_2}), \quad (42)$$

where $W_{\text{th}} = M + m_\pi$ and for simplicity, we suppress the explicit subscript of B . The parameters b_1 and b_2 , which are assumed to be positive, are adjusted from a fit to cross-section data in Sec. IV. We independently treat the background (parameters $b_{1,2}$) for transverse and longitudinal SF.

C. Real photon limit

In the real photon limit of $Q^2 = 0$ the longitudinal cross section vanishes and the photoproduction cross section σ_γ is given by Eq.(10). Note that σ_γ receives contributions from the resonance production process as well as from a nonresonant background scattering:

$$\sigma_\gamma(W^2) = \sigma_\gamma^{\text{Res}}(W^2) + \sigma_\gamma^{\text{BG}}(W^2), \quad (43)$$

where $W^2 = M^2 + 2ME_\gamma$ and E_γ is the photon energy in the target rest frame. The resonant part is given by $Q^2 \rightarrow 0$ limit of Eq.(28) and we have

$$\sigma_\gamma^{\text{Res}}(W^2) = \frac{2M}{W} \sum_R \frac{M_R^2 \Gamma_R (K_R/K) f_R^\gamma(W)}{(W^2 - M_R^2)^2 + M_R^2 \Gamma_R^2} |A(0)|^2, \quad (44)$$

where the notations are similar to those in Eq.(28).

At high energy the total cross section is dominated by nonresonant processes. We model the background cross section $\sigma_\gamma^{\text{BG}}$ in the full region of W by extrapolating a high-energy photoproduction cross section using Eq.(41). Note that for $W^2 > 10 \text{ GeV}^2$ the photoproduction cross section data can be phenomenologically described to a high accuracy in terms of two Regge poles [17]. We will use the result of the Regge fit of Ref.[17]:

$$\sigma_\gamma^{\text{Regge}}(s) = 0.0598s^{0.0933} + 0.1164s^{-0.357} \text{ mb}, \quad (45)$$

where $s = W^2$. In order to obtain the BG cross section in the full energy region, we apply a correction function by Eq.(41) to Eq.(45):

$$\sigma_\gamma^{\text{BG}}(W^2) = B_T(W^2) \sigma_\gamma^{\text{Regge}}(W^2). \quad (46)$$

IV. DATA SETS AND FIT

We adjust parameters of our model by fitting to data on the differential cross-section of inelastic electron scattering on hydrogen together with photoproduction cross section data. The data sets used in our analysis are listed in Table II and Table III. Note that our hybrid model is designed to smoothly match the DIS region. For this reason we do not include in the fit DIS data from CERN NMC [18] and BCDMS [19] and DESY H1 [20] and ZEUS [21], which were included in a global QCD analysis of Ref.[8, 9] whose PDFs and HT terms are used in our study.

The electron beam energy of SLAC experiments in Table II span the region from 2 to 20 GeV and the data cover a wide region including the resonance production and DIS. The beam energy of JLab experiments in Table II was in the range from 1.15 to 5.5 GeV and their data cover the resonance and transition region. The data sets of Table II agree in overlap region. The kinematics as well as statistics coverage of electron cross section data sets are illustrated in the (W^2, Q^2) plane in Fig. 1. The photoproduction cross section data at $Q^2 = 0$ are listed in Table III.

The parameters of our model are adjusted from minimization of the χ^2 function

$$\chi^2 = \sum_i (v_i^{\text{exp}} - v_i^{\text{mod}})^2 / d_i^2, \quad (47)$$

TABLE II. The hydrogen electroproduction cross-section data sets used in our analysis. Listed are the experiments with corresponding number of data points (NDP) and kinematics coverage. The values of Q^2 and W^2 are in GeV^2 units. The cut $W^2 > 1.16 \text{ GeV}^2$ was applied. “DIS” label indicates data which are mostly in the DIS region while “RES” label is for data samples which are mostly in the resonance region. The last two columns are the values of χ^2 normalized per NDP computed, respectively, in our model and in the model of Ref.[5], for comparison.

Data set	NDP	Q_{\min}^2	Q_{\max}^2	W_{\min}^2	W_{\max}^2	χ^2	χ_{CB}^2
SLAC-E49a (DIS) [22]	117	0.586	8.067	3.130	27.19	0.75	N/A
SLAC-E49b (DIS) [22]	208	0.663	20.08	3.010	27.51	1.90	N/A
SLAC-E61 (DIS) [22]	32	0.581	1.738	3.210	16.00	0.85	N/A
SLAC-E87 (DIS) [22]	109	3.959	20.41	3.280	17.18	0.94	N/A
SLAC-E89a (DIS) [22]	77	3.645	30.31	3.300	20.43	0.61	N/A
SLAC-E89b (DIS) [22]	118	0.887	19.18	3.100	27.75	1.33	N/A
SLAC-E004 (DIS) [23]	198	0.249	20.07	3.561	26.84	0.64	N/A
SLAC-NE11 (RES) [24]	113	1.606	6.855	1.164	1.788	2.20	5.78
SLAC-Onen1half ^a (RES) [23]	669	0.026	0.263	1.153	4.000	2.43	3.72
SLAC-E49a6 (RES) [23]	460	0.146	3.708	1.177	3.992	0.69	1.16
SLAC-E49a10 (RES) [23]	541	0.445	8.593	1.171	4.000	0.92	1.04
SLAC-E49b (RES) [23]	366	1.018	16.74	1.153	3.992	0.86	1.15
SLAC-E61 (RES) [23]	1075	0.061	1.839	1.160	4.000	0.98	1.76
SLAC-E87 (RES) [23]	22	1.821	20.54	3.183	3.988	0.20	N/A
SLAC-E891 (RES) [23]	90	7.124	32.39	1.156	4.000	0.11	N/A
SLAC-E8920 (RES) [23]	492	0.395	20.66	1.197	3.984	1.19	N/A
SLAC-E133 (RES) [23]	178	2.287	9.914	1.153	3.037	3.17	5.04
SLAC-E140 (RES) [23]	87	0.717	20.41	3.010	3.950	1.70	N/A
SLAC-E140X (RES) [23]	153	1.118	8.871	1.200	3.720	2.90	3.27
Jlab-CLAS E1 ^b (RES) [25–28]	509	0.225	0.925	1.162	2.544	1.12	19.5
Jlab-CLAS E2 (RES) [25–28]	1443	0.475	2.175	1.162	3.987	1.25	11.3
Jlab-CLAS E3 (RES) [25–28]	2484	1.325	4.175	1.162	5.537	1.16	2.73
Jlab-CLAS E4 (RES) [25–28]	2637	1.325	4.425	1.164	5.643	1.01	1.93
Jlab-CLAS E5 (RES) [25–28]	2681	1.375	4.725	1.162	5.971	1.01	1.51
JLab-E94-110 (RES) [23, 29]	1273	0.181	5.168	1.225	3.850	4.00	1.86
JLab-E00-116 (RES) [30]	261	3.585	7.384	1.243	5.131	1.78	2.15
JLab-E00-002 (RES) [23, 31]	1477	0.055	2.079	1.163	7.932	1.12	0.88

^a Data points with the beam energy $E = 5 \text{ GeV}$ are excluded.

^b The JLab-CLAS data sets E1, E2, E3, E4, E5 correspond to the beam energy 1.515, 2.567, 4.056, 4.247, 4.462 GeV, respectively.

TABLE III. The hydrogen photoproduction data sets used in our analysis. Listed are the experiments with corresponding number of data points (NDP) and kinematics coverage. The cut $W^2 > 1.16 \text{ GeV}^2$ was applied. The values of W^2 are in GeV^2 units. The last two columns are the values of χ^2 normalized per NDP computed in our model and in the model of Ref.[5], respectively.

Data set	NDP	W_{\min}^2	W_{\max}^2	χ^2	χ_{CB}^2
Armstrong [32]	159	1.378	8.790	1.21	1.34
Maccormick [33]	57	1.263	2.361	2.28	7.12
Meyer [34]	18	3.038	12.61	0.35	0.54
Hilpert [35]	6	2.121	9.212	2.08	1.66
Dieterle [36]	5	2.382	11.67	0.83	N/A
Ballam [37]	3	6.135	14.95	0.28	N/A
Bingham [38]	1	18.33	18.33	0.26	N/A
Caldwell [39]	9	8.518	31.62	1.19	N/A
Caldwell [40]	30	35.22	343.7	0.64	N/A
Michalowski [41]	6	4.633	18.73	0.77	N/A
Alexander [42]	1	14.95	14.95	0.01	N/A
Aid [43]	2	39999	43681	0.27	N/A
Vereshkov [44]	4	2065	17822	0.24	N/A
GRAAL [45]	62	1.950	3.564	6.09	6.50

where the sum runs over the cross section data points used in our fit, and v_i^{exp} and v_i^{mod} are the corresponding experimental and model values, and d_i^2 is the experimental uncertainty squared, for which we take the quadrature sum of statistical and systematic error.

We use the MINUIT program [46] in order to minimize χ^2 and find parameters of our fit. In preliminary trials we have 72 free parameters: the masses, widths, orbital momenta, damping parameters, and the branching fractions of resonance states in Table I; the parameters a_i and c_i of Eq.(32) and (33) describing the resonance amplitudes; the parameters b_i for the nonresonant background in Eq.(42) for transverse and longitudinal channels, scale parameter Q_0 , as well as the parameters m_T and m_L driving the Q^2 dependence of extrapolated structure functions in Eq.(38) and (40). We apply an iterative procedure to find the best fit parameters in our model.

We first applied our model to fit the total photoproduction cross section data at $Q^2 = 0$ in Table III. This allows us to determine the set of parameters of our model, in particular the resonance masses and widths as well as the normalization of resonance amplitudes $A(0)^2 = a_1^2$ together with parameters of the B_T function, which we use as input for further combined fit including both the photoproduction and electroproduction cross section data in Table II and III. In the studies of photoproduction cross section we also tried to optimize the angular momenta as well as the branching fractions of effective resonances, which then were fixed to the values listed in Table I.

In a combined fit we have a number of sequential iterations. In initial trials we kept the resonance parameters fixed and perform the adjustment of the parameters describing the background, b_i , as well as the exponents $m_{T,L}$ and $n_{T,L}$ controlling low- Q behavior of the structure functions. Then we tried to adjust the resonance parameters having the

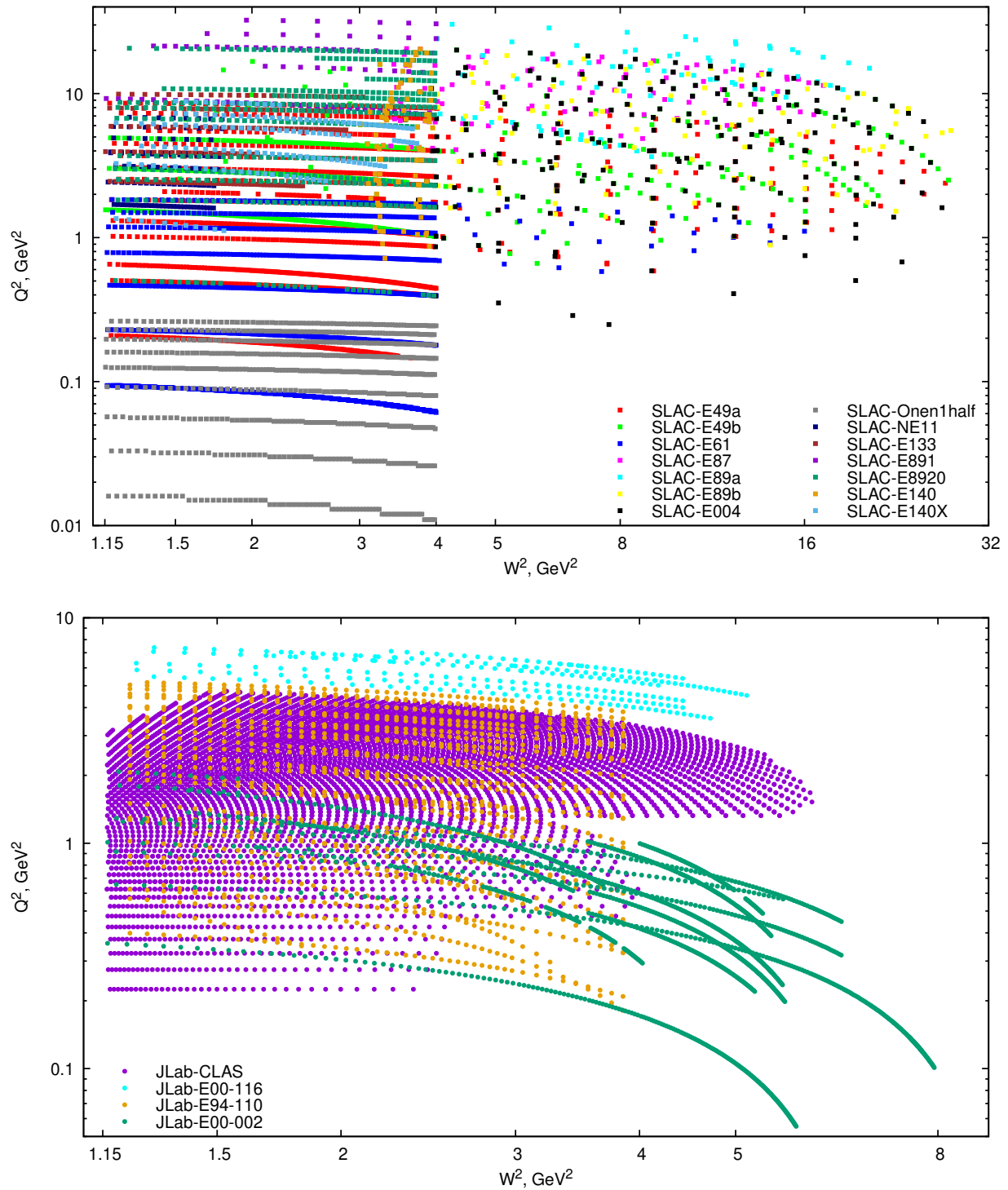


FIG. 1. (Color online) The (W^2, Q^2) space populated by data points of the electroproduction data sets in Table II. The upper (lower) panel is for SLAC (JLab) experiments. The color code and symbols for each of the data set are shown in the panels.

TABLE IV. The best fit parameters (uncertainty in per cent shown in parentheses) describing the resonant contributions to the transverse helicity amplitude by Eq.(32).

	a_1	a_2	a_3	a_4
$\Delta(1232)$	0.31153(0.34)	2.2237(0.46)	1.7711(0.20)	2.7695(0.12)
$N(1440)$	-0.061785(8.25)	0.71884(2.51)	0.8077(1.23)	2.8355(0.27)
R_1	0.10649(2.93)	0.36660(1.37)	0.79883(0.75)	2.7894(0.61)
R_2	0.33954(0.63)	-0.23593(1.62)	0.25799(3.51)	4.1098(2.10)
R_3	0.10645(1.19)	0.025199(4.95)	0.23215(1.53)	2.9477(1.89)

TABLE V. The best fit parameters (uncertainty in per cent is shown in parentheses) describing the resonant contributions to the longitudinal helicity amplitude by Eq.(33).

	c_1	c_2	c_3
$\Delta(1232)$	0.028105(13.9)	0.030275(9.53)	0.61827(2.68)
$N(1440)$	0.046808(18.7)	-0.13996(8.59)	1.1552(3.04)
R_1	0.079226(7.59)	-0.15799(5.59)	1.2034(2.45)
R_2	0.17213(11.8)	-1.5873(6.96)	4.6286(3.08)
R_3	-0.069282(3.08)	0	0.57903(3.84)

TABLE VI. The best fit parameters (uncertainty in per cent is shown in parentheses) describing the background function by Eq.(42).

	b_1	b_2	$m_{T,L}$
B_T	0.16906(1.20)	2.9065(0.55)	1.6463(0.23)
B_L	1.4161(3.38)	0.61408(1.68)	1.1

background fixed. This way allowed us to study the parameter correlations and also to locate the parameters to which the fit is most (less) sensitive.

In the course of our analysis we also observed that the fit prefers $n \rightarrow m$ limit on the exponents describing extrapolation of the structure functions (see Sec. III B). We then fixed $n = m$ for both F_T and F_L . We also tried to optimize the scale parameter t_0 , from which we start the extrapolation of the DIS structure functions down to $Q^2 = 0$, as described in Sec. III B, and found an optimal description at $t_0 = 1.3 \text{ GeV}^2$. This parameter was fixed in a final trial.

Thus on the final step we had 56 adjustable parameters, which were fit to minimize χ^2 by Eq.(47) over the combined set of electroproduction and photoproduction cross section data. It should be also commented that the fit results in numerically very small value of parameter $c_2(R_3)$ and in the final trial we fix $c_2(R_3) = 0$. Also, our fit prefers the numerical value of m_L exponent close to 1. Note that for the reason $R = F_L/F_T \rightarrow 0$ at $Q^2 \rightarrow 0$, the exponent $m_L > 1$. In the final trial we fix $m_L = 1.1$, which is also consistent with observed behavior of R at low Q^2 (see Sec. V and Fig. 11), and thus have 54 free parameters.

The best fit parameters together with relative uncertainties are listed in Table I, and Table IV to VI. The resulting values of χ^2 normalized per the number of data points (NDP) are listed in Table II for all electron-hydrogen differential cross section data sets used in the fit, and the corresponding χ^2 values for hydrogen photoproduction data are given in Table III. The last column in Table II and III lists the values of χ^2 computed for the model of Ref.[5], where applicable. We observe significant improvement over the fit results of Ref.[5] for all studied data sets except JLab E94-110 experiment.

In order to better illustrate our results, Fig.2 shows the frequency plot, *i.e.* the distribution of the data points vs. $\text{data}/\text{model} - 1$, where data/model is the ratio between observed and model value for the given cross section data point. Figure 2 is organized in histograms with the width of 0.01 separately for the DIS ($W^2 > 4 \text{ GeV}^2$) and the resonance ($W^2 < 4 \text{ GeV}^2$) region and for the full set of data points. We observe that the model predictions for the most of data points deviate from experiment by less than 5%.

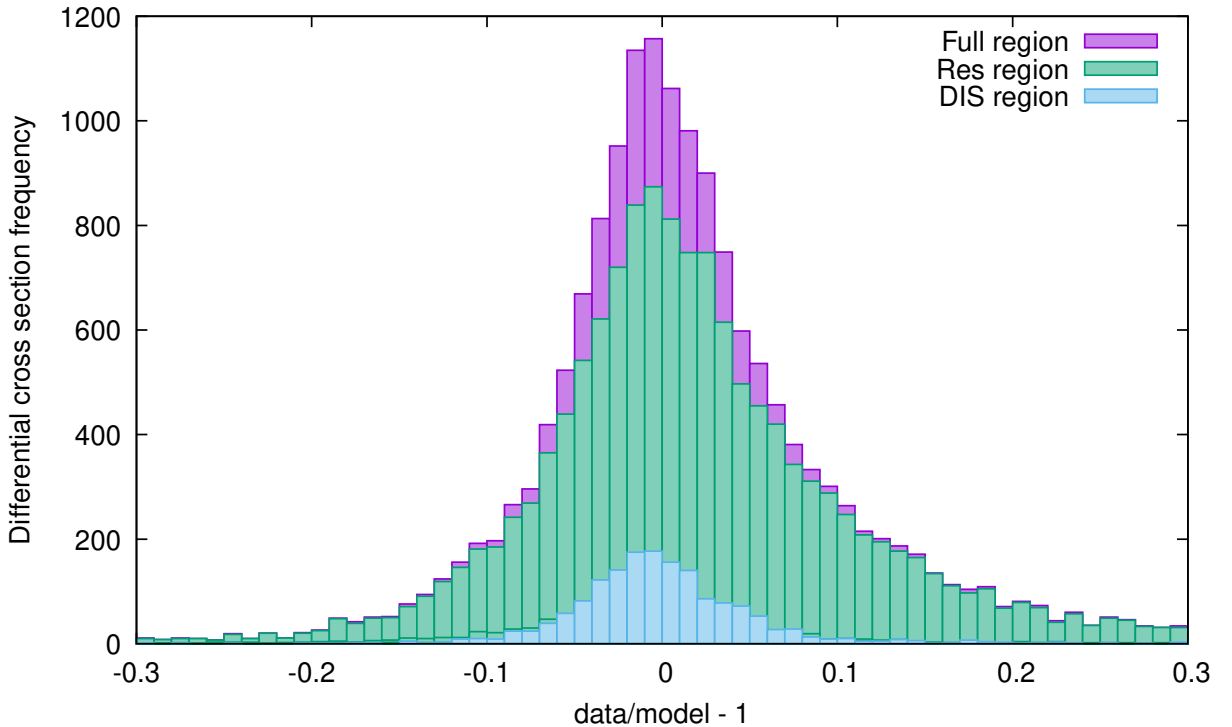


FIG. 2. (Color online) The frequency plot for the cross-section data points for DIS, resonance and the full region (see text).

In Fig. 3 to 6 we show a detailed data/model pulls for different cross section data subsets. Figure 3 refers to the photoproduction cross section at $Q^2 = 0$. The data/model pulls for electron inelastic cross section are illustrated in Fig. 4 to 6. The matrix of panels in those figures show the pulls for the Q^2 bins, which are indicated in the plot. Figure 4 illustrate the region $W^2 > 4 \text{ GeV}^2$ with the set of Q^2 bins covering the region $0.05 < Q^2 < 11 \text{ GeV}^2$, while Fig. 5 is focused on the resonance region $W^2 < 4 \text{ GeV}^2$ and $0.01 < Q^2 < 6.5 \text{ GeV}^2$. In view of a large number of data points from the JLab CLAS experiment [25–28], which are presented for fixed Q^2 bins, we show the comparison with JLab CLAS data points in Fig.6. Overall, our model shows a very good agreement with data in a wide region of Q^2 and W^2 and most of the central points of the data/model ratio fall into 1 ± 0.05 band. However,

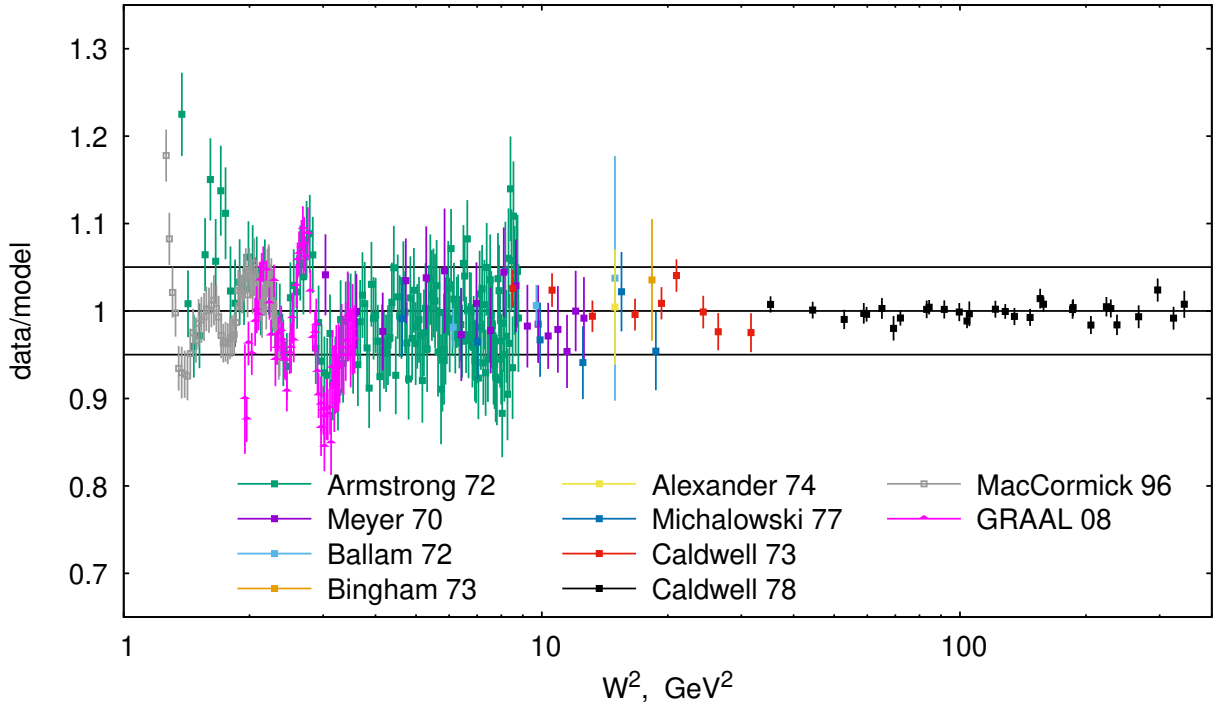


FIG. 3. (Color online) The data/model pulls computed for the best fit parameters of our model for photoproduction cross section data of Table III. The error bars include statistical and systematic uncertainties of data taken in quadrature. Also shown is the band 1 ± 0.05 . The legend for the data points is shown in the plot.

we also observe rather strong fluctuations of the data/model ratio for some data sets. In particular, the pulls for different beam energies of JLab CLAS cross section data are not always fully consistent (see, *e.g.*, the bins with $Q^2 > 1.3 \text{ GeV}^2$ in Fig. 6). The fluctuations of the data/model ratio are high in the region $W^2 < 1.5 \text{ GeV}^2$, as can be seen in Fig. 5. The last column in Table II lists the values of χ^2 computed for the model of Ref.[5], where applicable. We observe significant improvement over the results of Ref.[5] for all studied data sets except for JLab E94-110 experiment.

A detailed comparison of our predictions with cross section data on both, the electron-proton inelastic differential cross section from Table II and the total photoproduction cross section from Table III, can be found in Sec. A.

V. DISCUSSION

As described above, in our cross section analysis we determine both structure functions, F_L and F_T . In order to verify our results, here we compare the model predictions with data which were not used in our fit, in particular the measurements of the structure function F_2 and $R = F_L/F_T$.

We first discuss the extraction of the structure function F_2 . Table VII lists the data sets on the proton F_2 together with the values of χ^2 computed in our model using the corresponding experimental uncertainties which include statistical and systematic errors

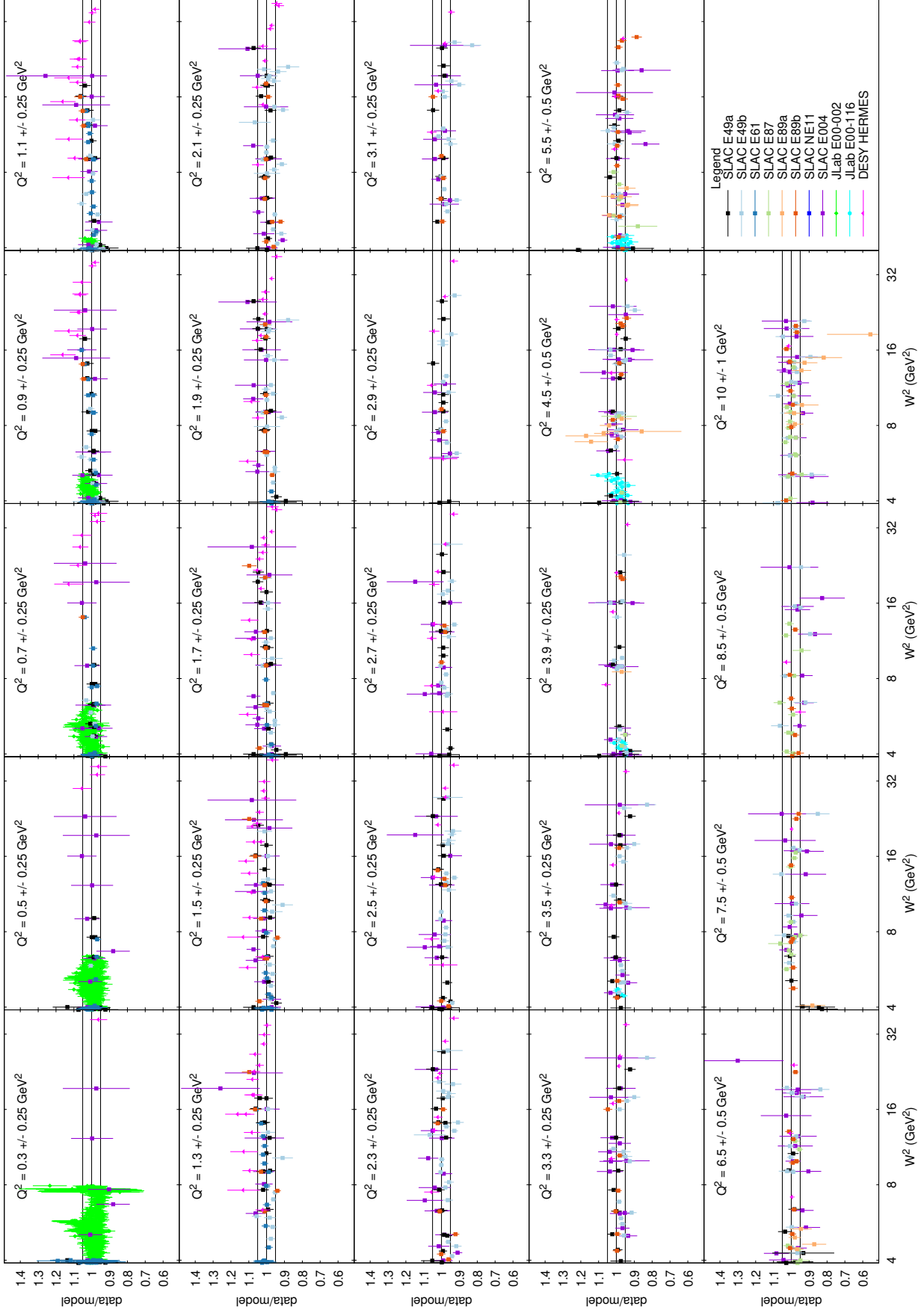


FIG. 4. (Color online) The cross section data/model pulls computed for the best fit parameters of our model for data of Table II with $W^2 > 4$ GeV 2 . Data points are grouped in Q^2 bins indicated in the panels. The error bars include statistical and systematic uncertainties of data taken in quadrature. Also shown is the band 1 ± 0.05 . The legend for the data points is shown in the last panel.

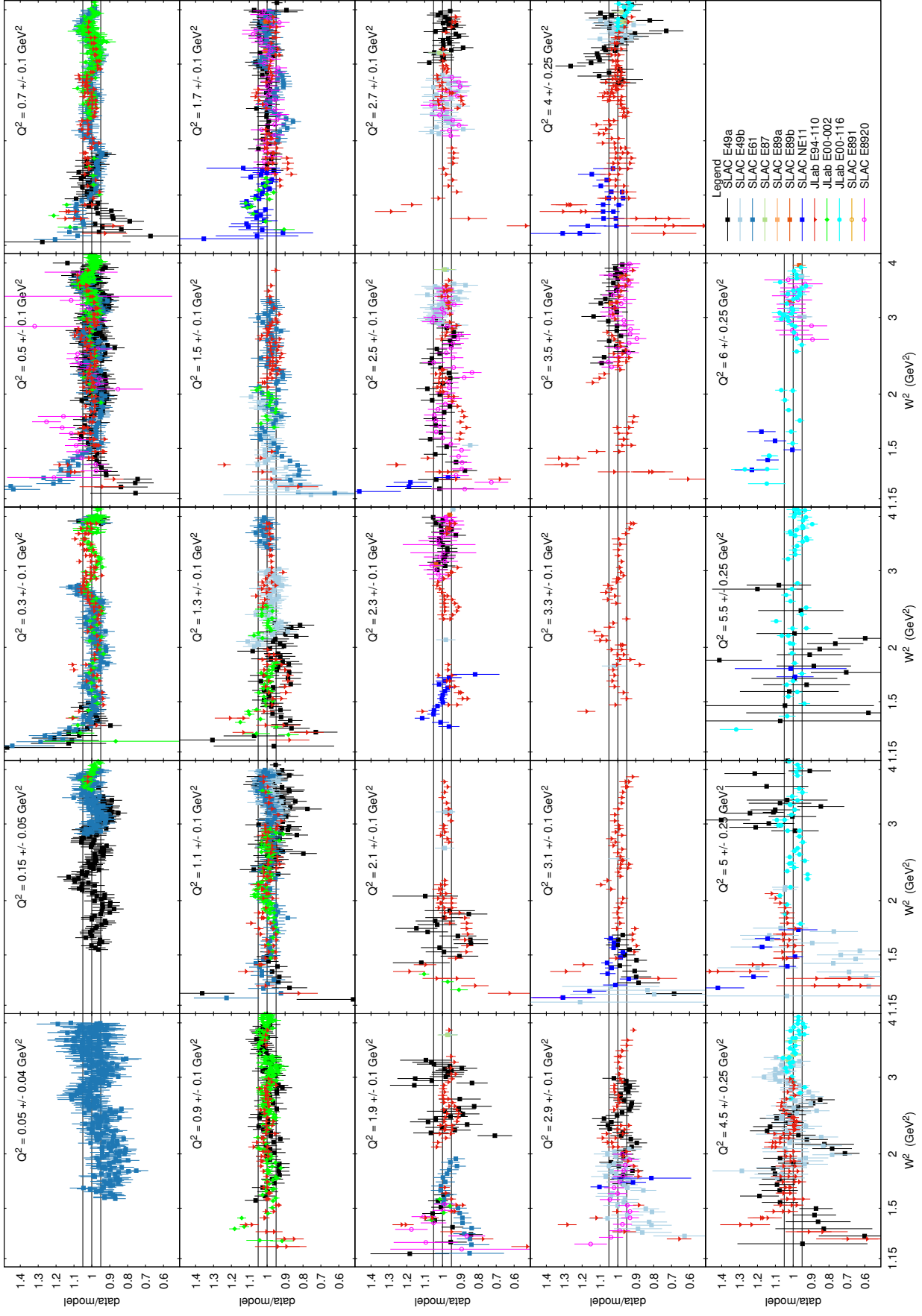


FIG. 5. (Color online) The cross section pulls similar to Fig. 4 but focused at the resonance region $1.15 < W^2 < 4 \text{ GeV}^2$. Note a different Q^2 binning.

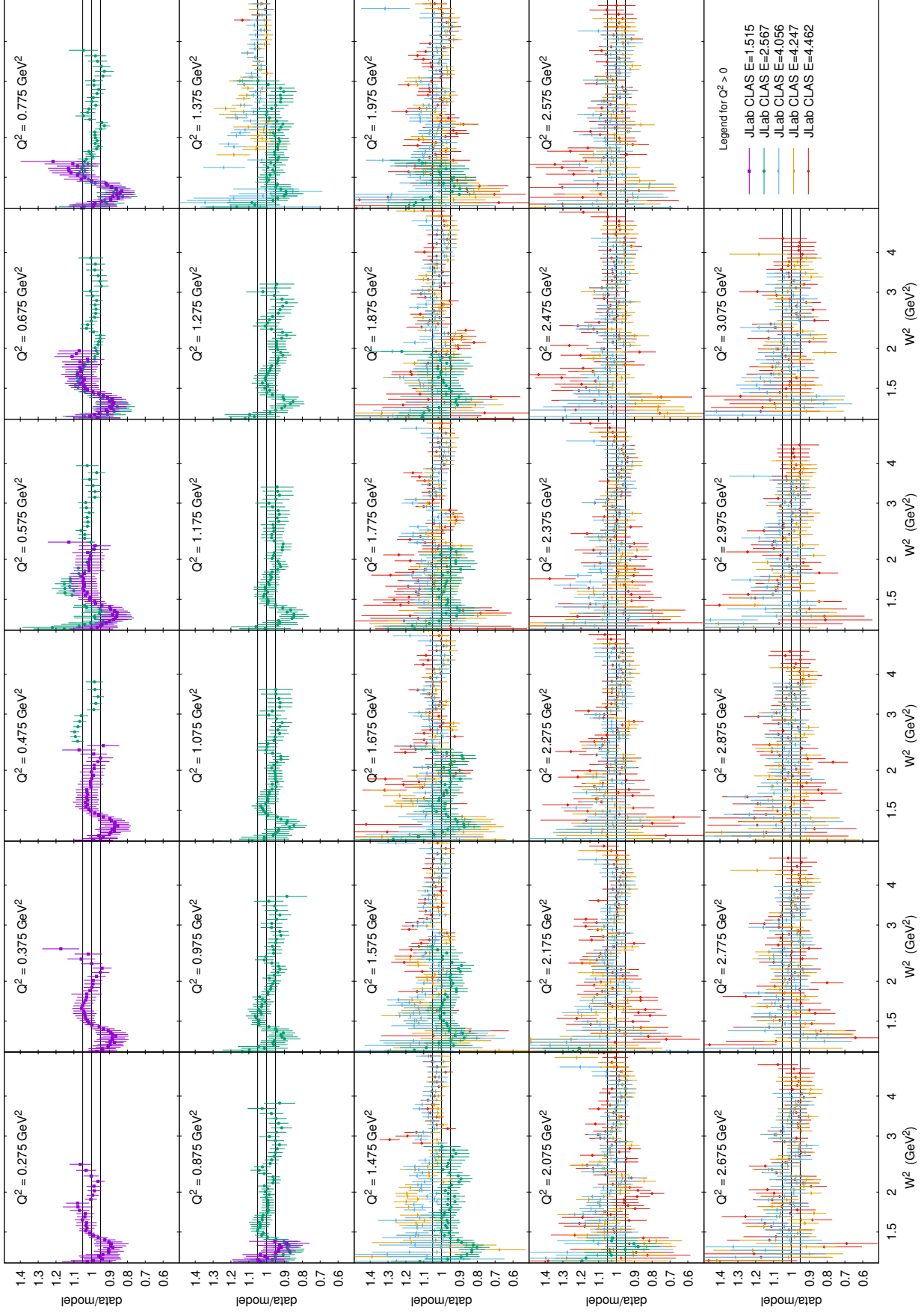


FIG. 6. (Color online) The cross section data/model pulls computed for JLab CLAS data listed in Table II. Data points are grouped in Q^2 bins indicated in the panels. The error bars include statistical and systematic uncertainties of data taken in quadrature. Also shown is the band 1 ± 0.05 . The legend for data points is shown in the last panel.

added in quadrature. The F_2 data include the results of Ref.[22] on SLAC data as well as the measurements from JLab experiments [25, 26, 29–31, 47]. Table VII lists the values of χ^2 per one data point for each F_2 data set. Note that the extractions of the structure functions from cross section data depend on the input for R . In this comparison we use the F_2 extractions of Ref.[29, 31] which were based on the Rosenbluth separation of F_T and F_L . The F_2 extractions from Ref.[22, 26, 30] used different models of R constrained by data.

Our results are illustrated in Fig. 7 to 10. Figure 7 shows the F_2 pulls for $W^2 > 4 \text{ GeV}^2$ and $0.25 < Q^2 < 30 \text{ GeV}^2$, which are organized in the panels of Q^2 bins indicated in the plot. Figure 8 shows similar pulls for the resonance region of $W^2 < 4 \text{ GeV}^2$ and $0.2 < Q^2 < 5.5 \text{ GeV}^2$. In addition to SLAC and JLab experiments, in Table VII and Fig. 7 we also show the F_2 measurements from DESY HERMES [48], CERN NMC [18] and CERN BCDMS [19]. We observe a very good agreement of our model with the data in the full range of kinematics. A detailed comparison of our predictions for absolute values of F_2 with data from different experiments is presented in Fig. 9 and 10. These figures are also organized in terms of panels of Q^2 bins which are indicated in the plots. The curves with our predictions are drawn for the central value of each Q^2 bin. Figure 9 covers the region up to $W^2 = 150 \text{ GeV}^2$, while Fig. 10 focuses on the resonance region $1.15 < W^2 < 4.2 \text{ GeV}^2$ and $0.25 < Q^2 < 5 \text{ GeV}^2$.

For comparison, together with our predictions in Fig. 9 and 10 we also show the predictions by the model of Ref.[5] (CB, the dashed curve). We observe that our predictions are consistent with those of the CB fit for $W^2 < 8 \text{ GeV}^2$. The inspection of χ^2 values in Table VII suggests that our approach provides better overall description of data in the resonance region for almost all data sets except for JLab E94-110 experiment. The CB model fails in the DIS region $W^2 > 8 \text{ GeV}^2$. In contrast, since our model is designed to continuously merge the SF from a global QCD fit of Ref.[8, 9] at high values of Q^2 and W^2 , our predictions can be applied in a wide range of kinematics. For completeness, in Fig. 9 and 10 we also show the background contribution which clearly dominates for $W^2 > 4 \text{ GeV}^2$ and merge with the DIS structure function at high W^2 .

Since in our analysis we determine both, F_T and F_L , we apply our results to compute $R = F_L/F_T$ and make a comparison with data on the structure function R . Figure 11 shows the measurements of R [22, 29, 31, 47, 51–53] as a function of W^2 together with our predictions (normalization uncertainties are not shown in Fig. 11). The plots in Fig. 11 are organized in terms of panels of Q^2 bins covering the region from 0.25 to 11 GeV^2 . The data points marked with the symbol “R” in the legend correspond to the measurements using the Rosenbluth separation method. Our predictions are indicated by the solid curve and for comparison we also show the predictions from the CB model [5] as well as the R_{1998} fit of Ref.[53]. We observe a good agreement of our predictions with data for the full kinematics interval considered, although the data uncertainties are rather large. It should be also remarked that while our predictions are for the proton, the data on R in Fig. 11 are collected for different nuclear targets including ^2H , ^{56}Fe , ^{197}Au (SLAC-E140 [51]), ^2H and ^9Be (SLAC-140X [52]), and ^{12}C (SLAC-E143 [53]).

Our combined fit leads to a good overall description of total photoproduction cross section, as illustrated by the pulls in Fig. 3 and the cross section plot in Fig. A1, but for the third resonance peak the model predictions are somewhat off the data. On the other hand the electron scattering data in the third resonance peak is well described by the model even at low values of Q^2 (see the pulls and cross section plots in Sec. A). Note our combined fit is dominated by electron cross section data. In a fit to the $Q^2 = 0$ photoproduction data only we achieve perfect description of data in the full region with somewhat different resonance

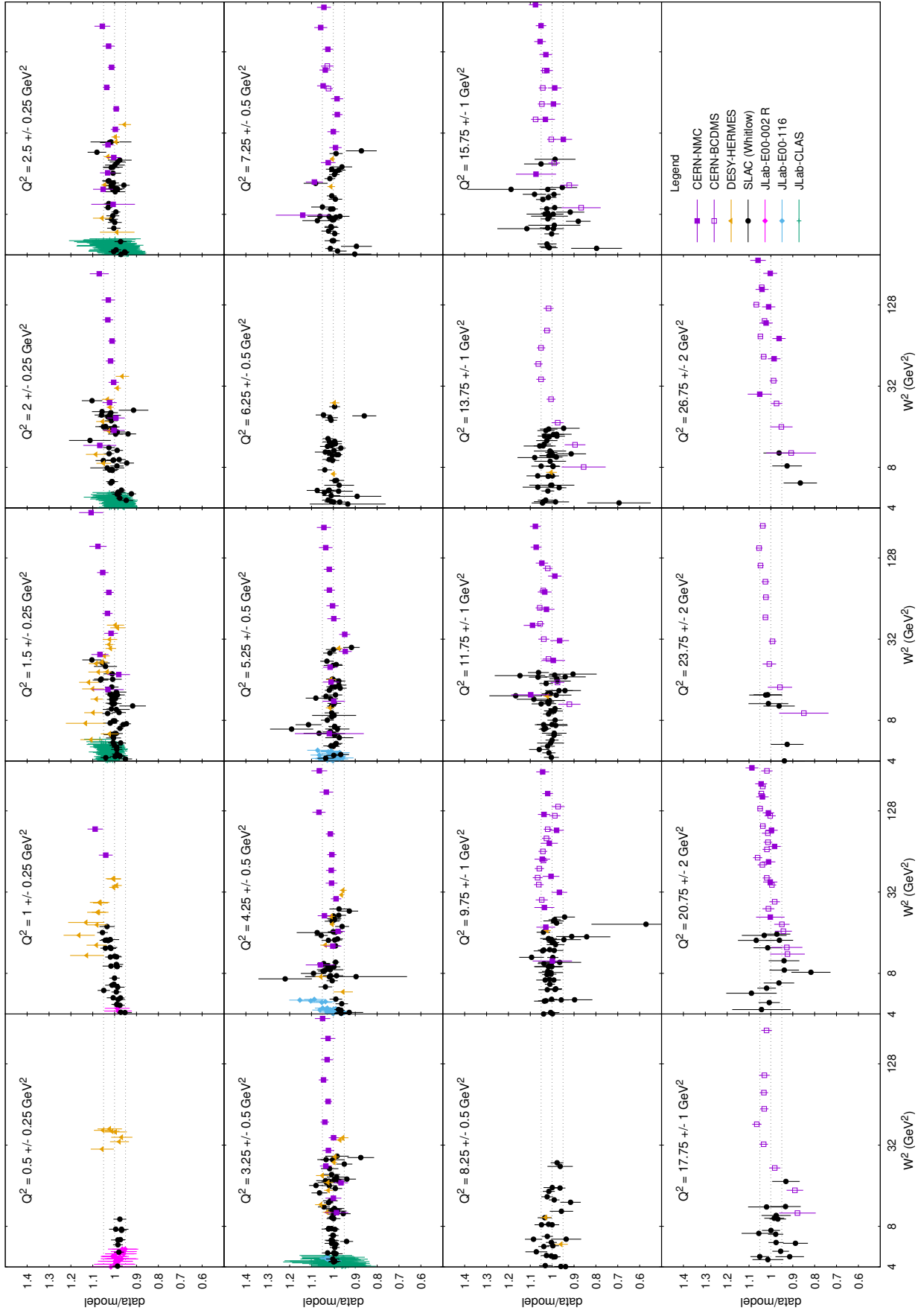


FIG. 7. (Color online) The pulls for F_2 as a function of W^2 computed for the best fit parameters of our model for the F_2 data in Table VII. Shown is the region $W^2 > 4$ GeV 2 . Data points were grouped in Q^2 bins indicated in the panels. The error bars include statistical and systematic uncertainties of data taken in quadrature. The dashed lines indicate the band 1 ± 0.05 . The legend for the data points is shown in the lower-right panel.

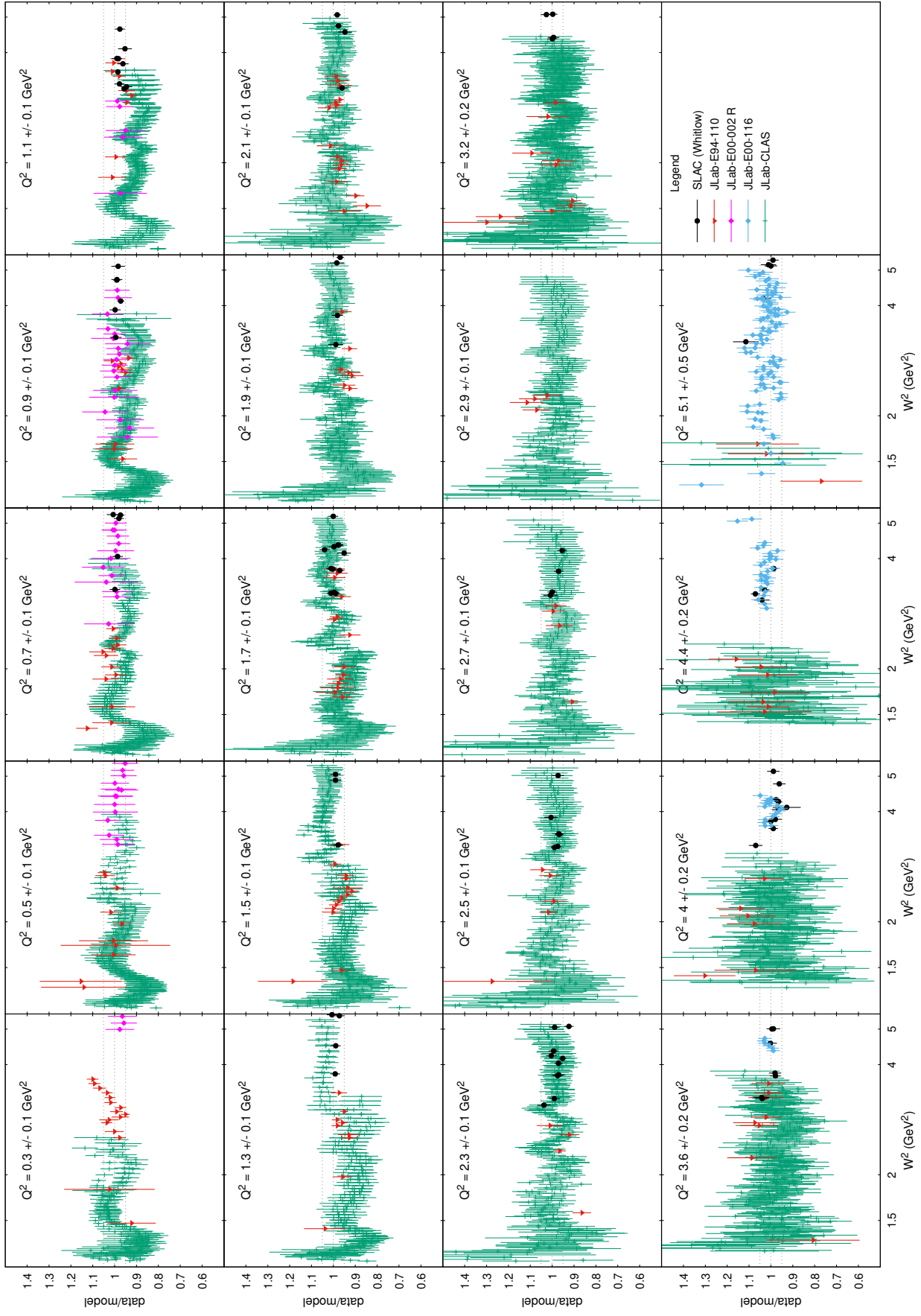


FIG. 8. (Color online) Similar to Fig.7 but for $W^2 < 4$ GeV 2 .

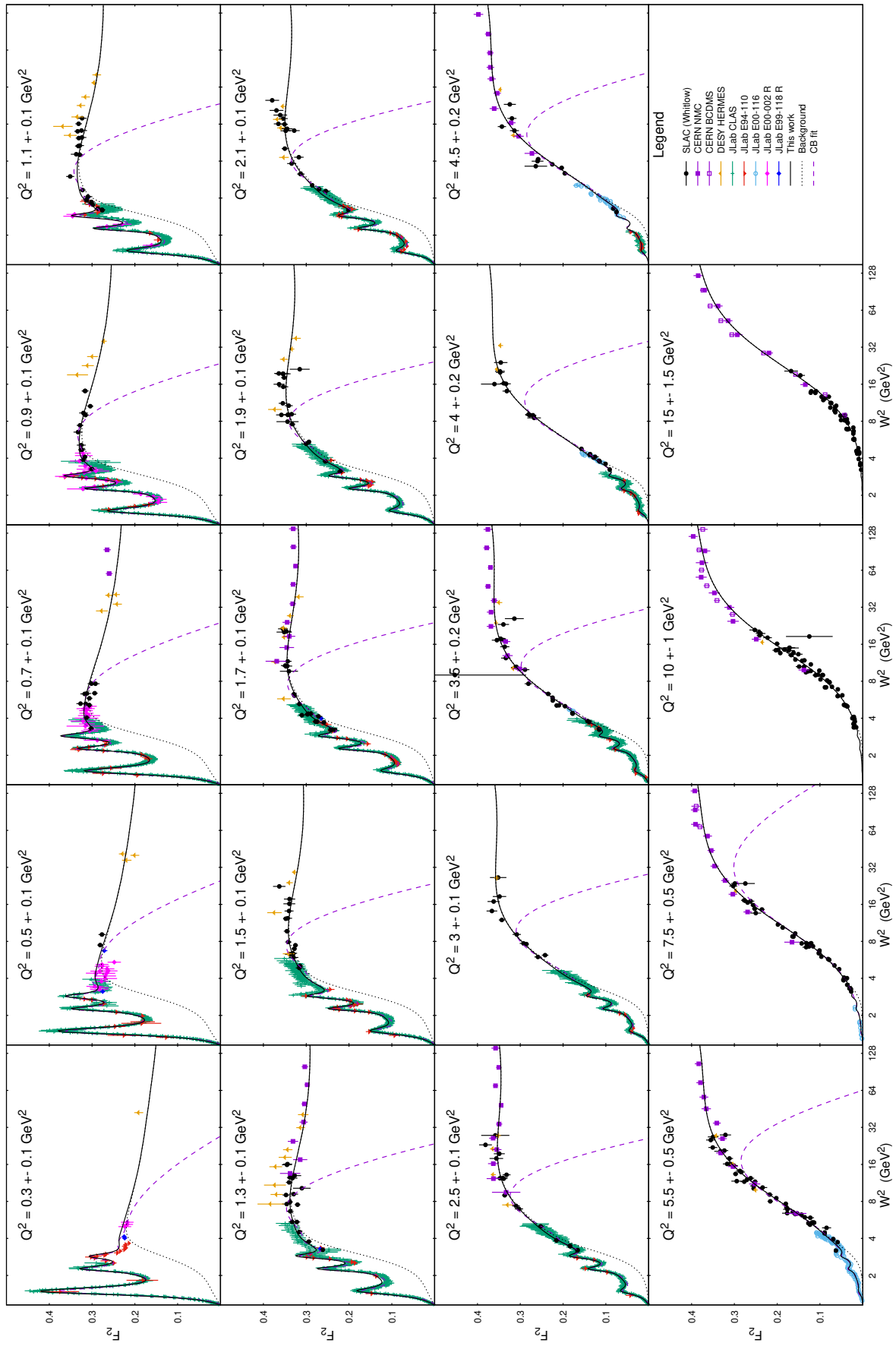


FIG. 9. (Color online) Our predictions on F_2 in comparison with data for $W^2 < 150 \text{ GeV}^2$. The legend for the data points is shown in the lower-right panel. The background contribution is shown by dotted line while the model of Ref.[5] is the dashed line.

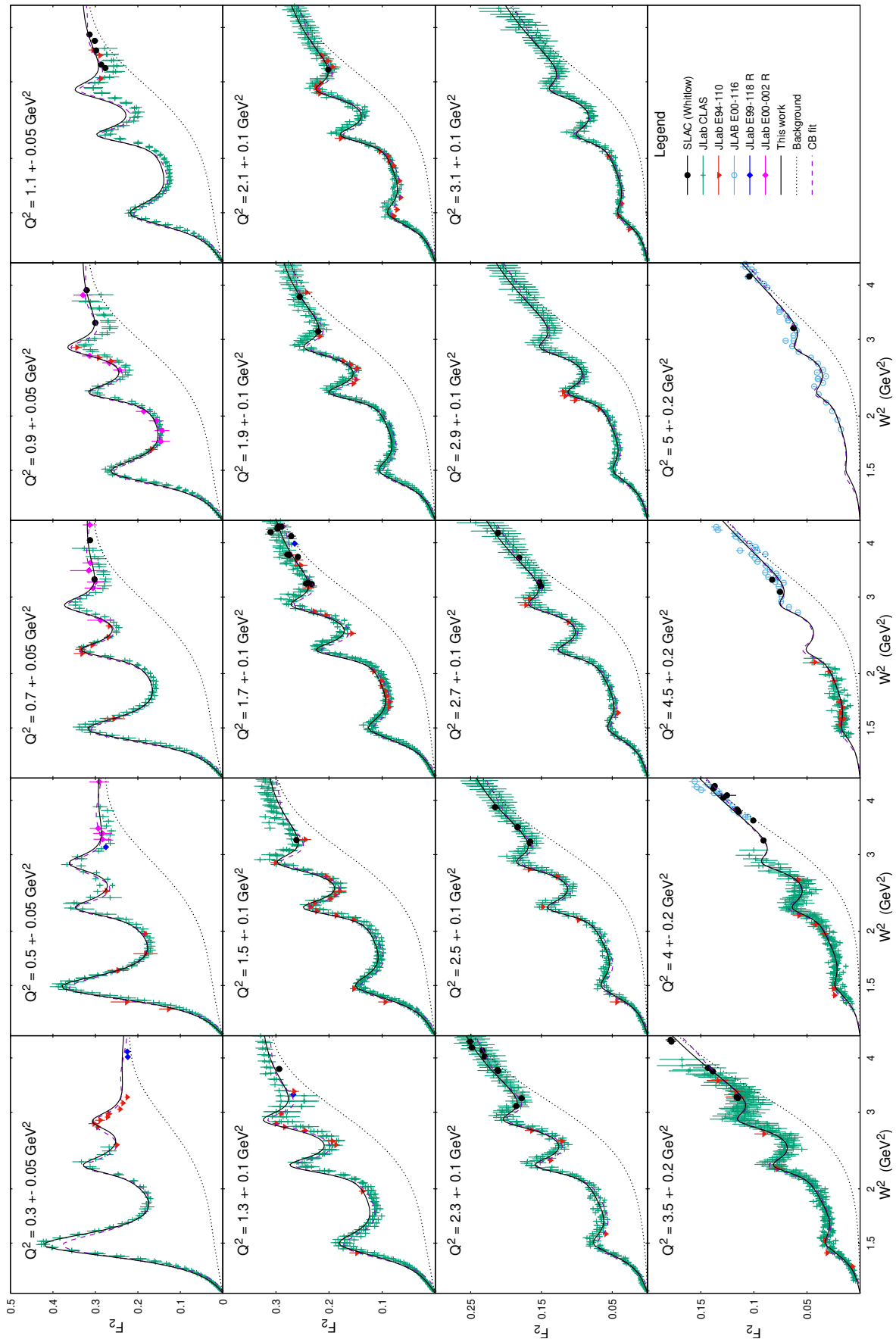


FIG. 10. (Color online) Similar to Fig. 9 but with the focus on the resonance region $1.15 < W^2 < 4.5 \text{ GeV}^2$. Note also the Q^2 binning is different from Fig. 9

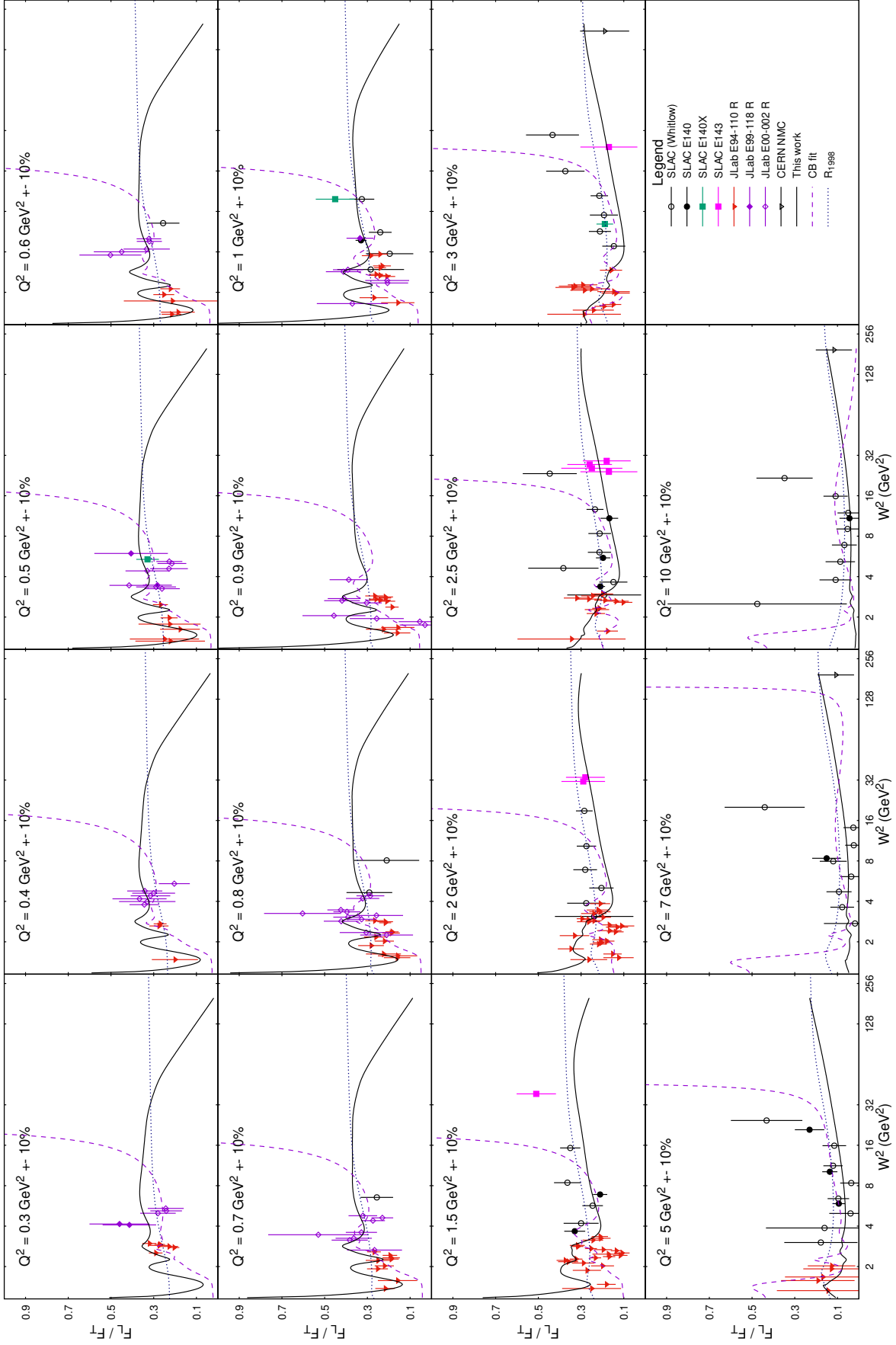


FIG. 11. (Color online) Our predictions on the ratio $R = F_T/F_L$ vs. W^2 in comparison with data for a number of Q^2 bins indicated in the plot. The curve is drawn for the central value of each Q^2 bin. The prediction from the fit of Ref.[5] is shown by dashed curve. The legend is shown in the lower-right panel.

TABLE VII. The values of χ^2 per one data point computed for various F_2 data sets. Listed are the experiments with corresponding number of data points (NDP) and kinematics coverage. The values of Q^2 and W^2 are in GeV^2 units. "DIS" label indicates data which are mostly in the DIS region while "RES" label is for data samples which are mostly in the resonance region. The last two columns are the values of χ^2 normalized per NDP computed, respectively, in our model and in the model of Ref.[5], when applicable.

Data set	NDP	Q_{\min}^2	Q_{\max}^2	W_{\min}^2	W_{\max}^2	χ^2	χ_{CB}^2
CERN-NMC [18] (DIS)	157	0.750	65.00	6.380	553.9	1.85	N/A
CERN-BCDMS [19] (DIS)	177	7.500	230.0	8.042	351.0	3.07	N/A
DESY-HERMES [48] (DIS)	80	0.354	12.78	5.751	42.17	2.22	N/A
SLAC-E49a [22, 49] (DIS)	117	0.586	8.067	3.131	27.24	0.74	N/A
SLAC-E49b [22, 49] (DIS)	208	0.663	20.08	3.007	27.51	1.09	N/A
SLAC-E61 [22, 49] (DIS)	32	0.581	1.738	3.213	16.05	0.75	N/A
SLAC-E87 [22, 49] (DIS)	109	3.959	20.41	3.287	17.16	1.03	N/A
SLAC-E89a [22, 49] (DIS)	77	3.645	30.31	3.303	20.46	1.07	N/A
SLAC-E89b [22, 49] (DIS)	118	0.887	19.18	3.099	27.78	0.99	N/A
JLab-CLAS [26] (RES)	4191	0.225	4.725	1.162	5.804	1.19	6.13
JLab-E94-110 [47] (RES)	170	0.181	4.794	1.325	3.850	1.43	0.72
JLab-E00-116 [50] (RES)	261	3.585	7.384	1.243	5.132	1.77	2.33
JLab-E00-002 [31] (RES)	54	0.300	1.000	1.650	5.419	0.13	0.05

parameters which are in tension with electron cross section data. This may indicate possible Q^2 dependence of the Breit-Wiegner pole masses, $M_R(Q^2)$. We plan to update our studies along these lines.

We also found that our result on the average transverse amplitude $A(Q^2)^2$ for $\Delta(1232)$ state is in a good agreement with the results of MAID analysis [4]. Also, for $N(1440)$ resonance we obtained the parameter a_1^2 to be consistent with the value reported in PDG review [16]. Note that the parameter a_1^2 drives the strength of corresponding resonance peak in the photoproduction cross section at $Q^2 = 0$.

In conclusion, we examine the quark-hadron duality property of our model. The duality principle suggests an integral relation between the observed structure function, which includes the resonance contributions, and a smooth DIS structure function [54]. We examine the duality between our hybrid model by Eq.(30) and the DIS structure function by Eq.(11) by verifying the integral relation

$$\int_{W_{\text{th}}^2}^{W_0^2} dW^2 F_2(W^2, Q^2) = \int_{W_{\text{th}}^2}^{W_0^2} dW^2 F_2^{\text{DIS}}(W^2, Q^2), \quad (48)$$

where the integration is taken from the pion production threshold $W_{\text{th}}^2 = (M + m_\pi)^2$ to the boundary of the resonance region for which we take $W_0^2 = 4 \text{ GeV}^2$. We found this relation holds with rather high accuracy for F_2 with deviation ranging between 1 and 2% for $1.3 < Q^2 < 5 \text{ GeV}^2$. We also studied Eq.(48) individually for both, F_T and F_L . We found somewhat lower accuracy of the duality relation for F_T with the deviation up to 5% for $1 < Q^2 < 3 \text{ GeV}^2$. For higher Q^2 the accuracy of the duality relation for F_T is on the level

of that for F_2 . The accuracy of the duality relation is poor for F_L for $1 < Q^2 < 3 \text{ GeV}^2$, where the deviation from Eq.(48) is between 15 and 25%. However, its accuracy gradually increases with Q^2 .

VI. SUMMARY

To summarize, in this paper we discussed a hybrid model of the proton structure functions applicable in a wide region of Q^2 and W^2 . The DIS region is well described in terms of the proton PDFs and the higher-twist terms extracted from a global QCD analysis. The present study is based on the results of the global QCD fit [8, 9] performed with particular emphasis on the region of low Q^2 . In the nucleon resonance region, the excitation of the resonant states is described in terms of the Breit-Wigner pole contributions from $\Delta(1232)$ resonance, Roper $N(1440)$ resonance, and three more heavy effective resonances responsible for the second and third resonance regions in the spectra. Along with the resonant processes, the inelastic cross section receives contributions from non-resonant (background) processes. We model the background in terms of the DIS structure functions properly continued into the low- Q and low- W region. To this end we discuss a smooth extrapolation of the DIS structure functions down to $Q^2 = 0$ and $W^2 = (M + m_\pi)^2$ respecting the the real photon limit as well as the behavior near the inelastic threshold.

The model parameters, such as resonance masses and widths, parameters of resonance helicity amplitudes, scale factor for the transition region, as well as parameters responsible for extrapolation to low- Q and low- W values, were adjusted from a combined fit to data on the electron-proton differential cross section together with the total photoproduction cross section. This approach allows us to determine both, F_T and F_L structure functions, and reproduce available cross-section data to a very good accuracy, for most of the data points the deviation of the ratio data/model from 1 is within a 5% band, as illustrated in Fig. 3 to 6. A detailed comparison of our model with cross section data is presented in Sec.A.

We verify performance of the model by comparing our predictions with available data on the proton F_2 and the ratio $R = F_L/F_T$. Figure 7 to 10 and Table VII show a very good overall agreement of our predictions with F_2 data. Also for R , our predictions are in accord with available measurements, as shown in Fig. 11. We also verified that our hybrid model of structure functions is dual in the integral sense to the underlying DIS structure functions. The duality relation, Eq.(48), holds with a good accuracy for F_2 . However, the accuracy of that relation is somewhat worse for F_T and poor for F_L .

The work is in progress on the application of the present analysis to the determination of the neutron structure functions from a combined set of the proton and the deuterium data. Also in progress is the generalization of this model to neutrino-nucleon scattering in the resonance and the DIS region, which is of primary importance for interpretation and analysis of data from current and future neutrino experiments.

The tables of values of the structure functions F_T and F_L computed with the best fit parameters on a grid of W^2 and Q^2 are available upon email request from the authors.

VII. ACKNOWLEDGMENTS

We thank S. Alekhin, A. Kataev, and R. Petti, for useful discussions, M. Osipenko for providing the data of CLAS collaboration. V. V. Barinov was supported by the BASIS

Appendix A: Comparison of model predictions with cross section data

Here we present a detailed comparison of our model predictions with the absolute values of differential cross section data from the experiments with hydrogen.

Figure A1 shows the total photoproduction cross section vs. W^2 . The data points are from experiments listed in Table III and the legend is given in the figure. The solid line corresponds to our model with the best fit parameters from Sec.IV, while the dotted line shows the background part of the cross section.

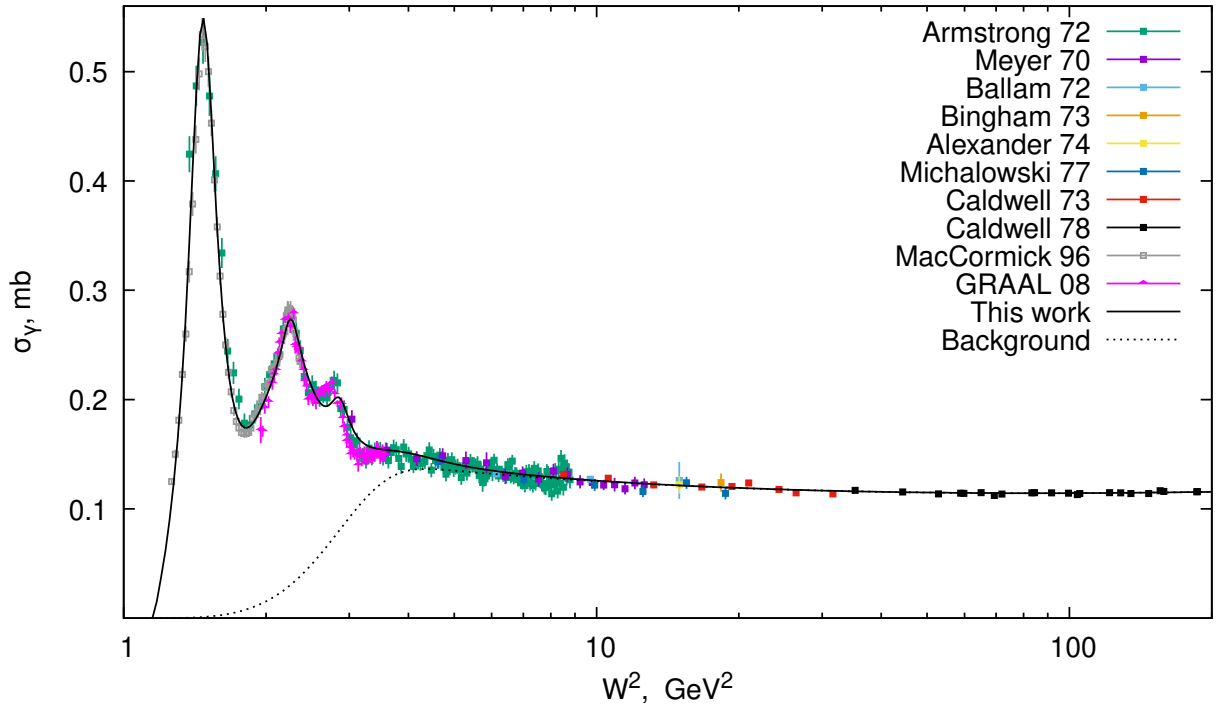


FIG. A1. (Color online) Comparison of predictions of our model (solid line) with data on the total photoproduction cross section off the hydrogen vs. W^2 . The legend for various photoproduction data are given in the figure.

In Fig. A2 to A15 we show our results (solid line) in comparison with electron inelastic differential cross section data from experiments listed in Table II. The figures are organized in terms of panels of given beam energy and scattering angle whose values are shown in the panels. The data points for the resonance ($W^2 < 4 \text{ GeV}^2$) and DIS ($W^2 > 4 \text{ GeV}^2$) region are marked with different symbols/color. The error bars on data points include statistical and systematic errors of corresponding experiment taken in quadrature.

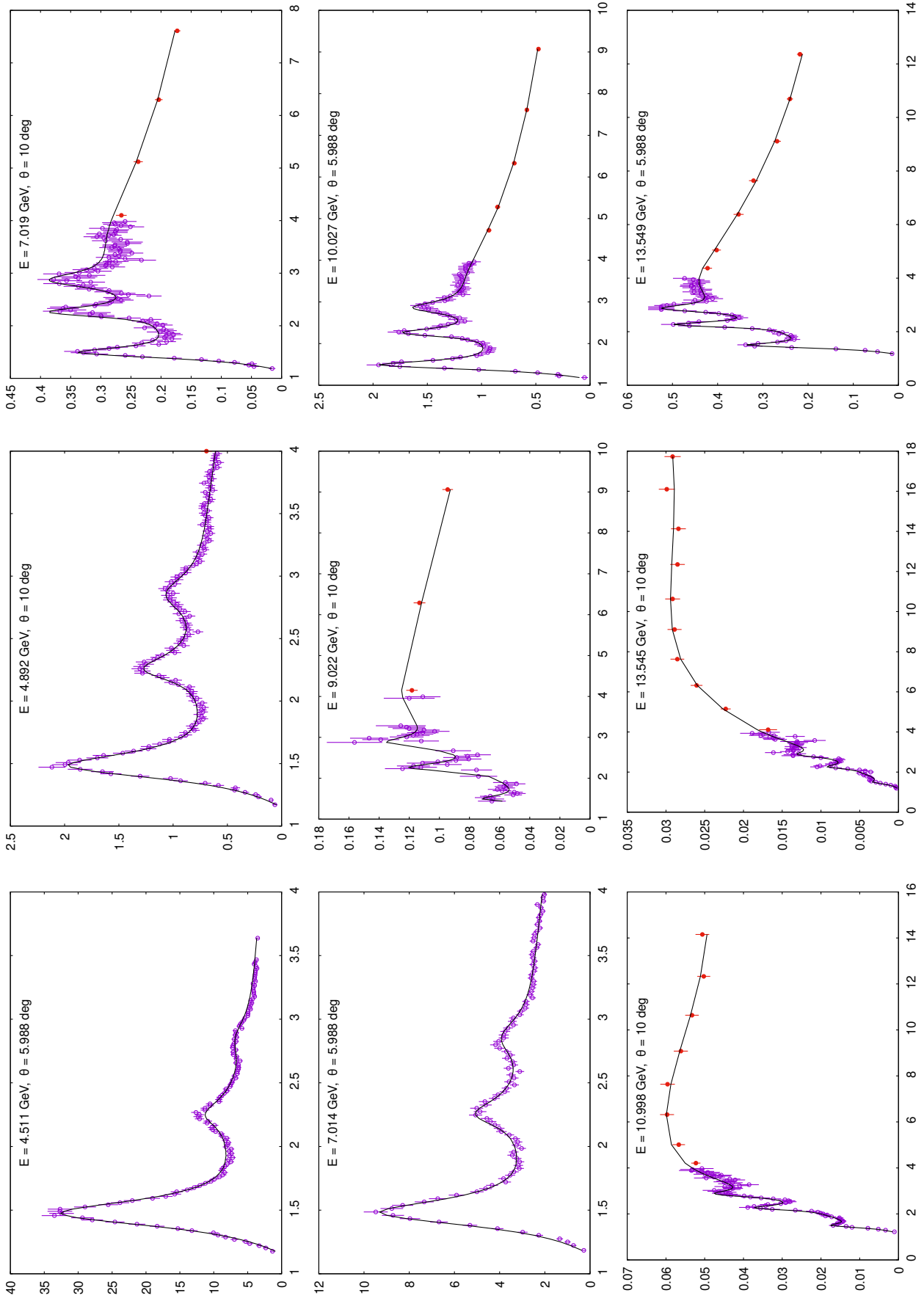


FIG. A2. (Color online) Comparison of our model (solid line) with SLAC-E49a data on differential cross section $d^2\sigma/(d\Omega dE')$ in $\mu\text{b}/(\text{Sr GeV})$ vs. W^2 in GeV^2 . Beam energy and scattering angle value are given in the figure panels.

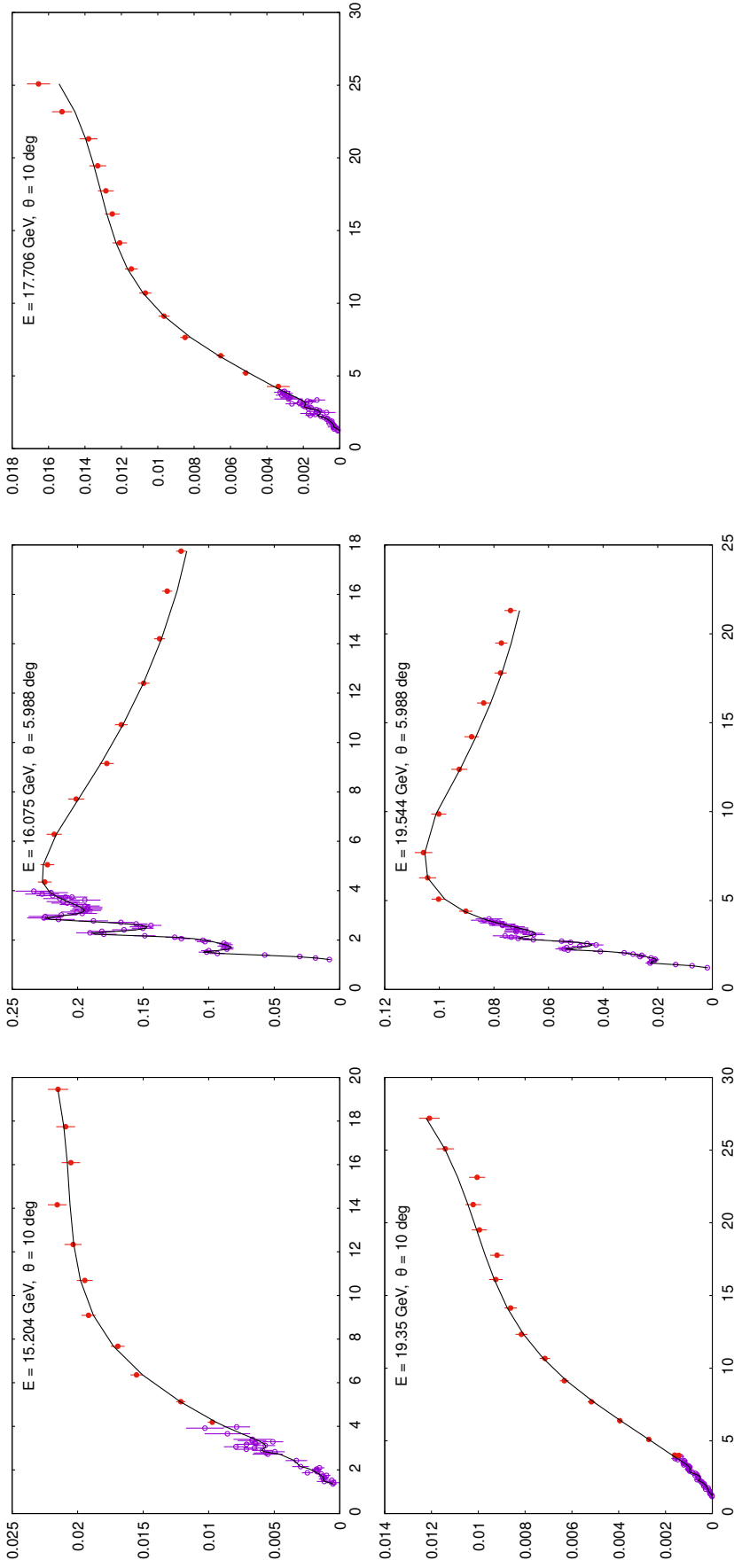


FIG. A2. Continued

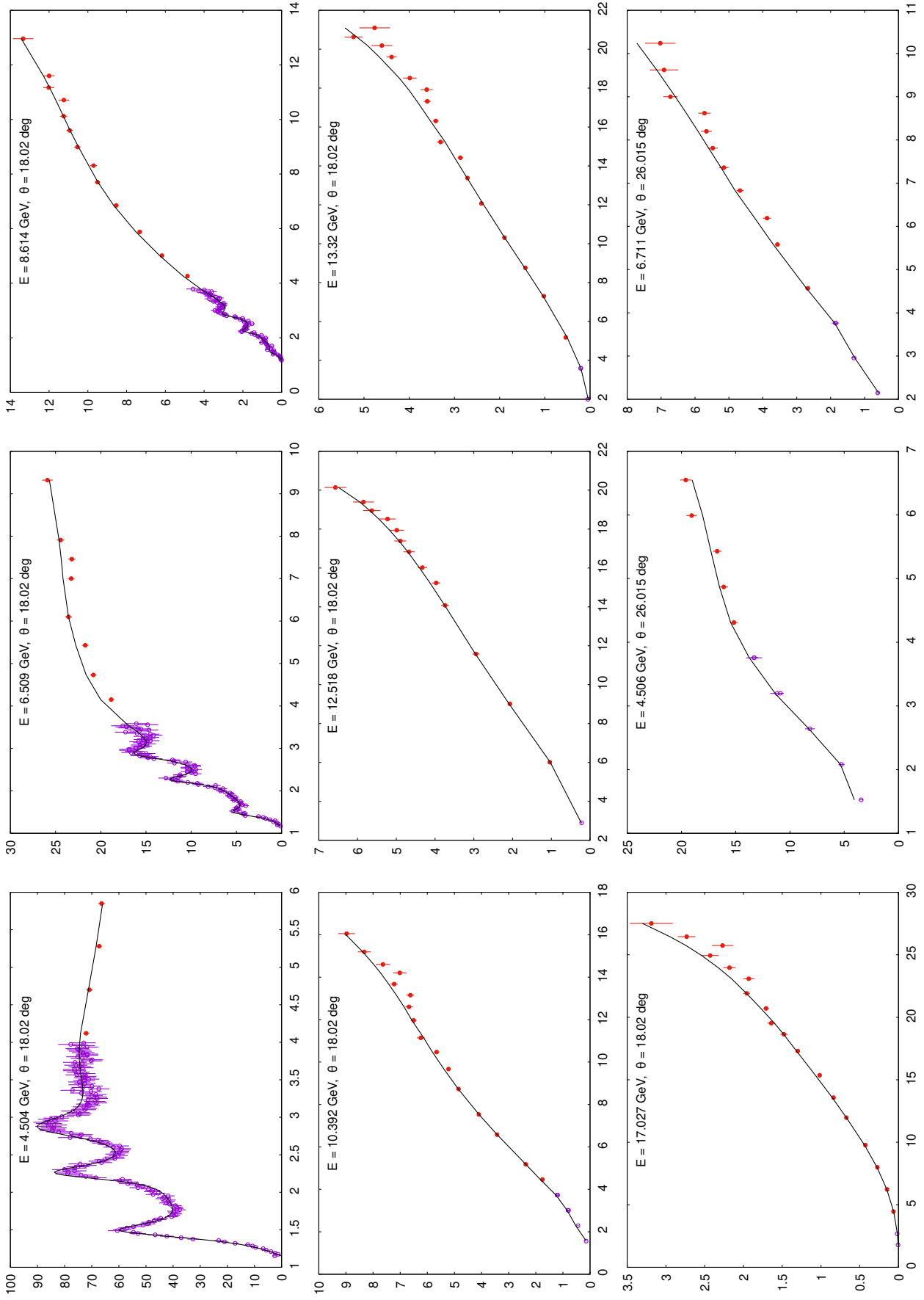


FIG. A3. (Color online) Comparison of our model (solid line) with SLAC-E49b data on differential cross section $d^2\sigma/(d\Omega dE')$ in nanobarn/(Sr GeV) vs. W^2 in GeV^2 . Beam energy and scattering angle value are given in the figure panels.

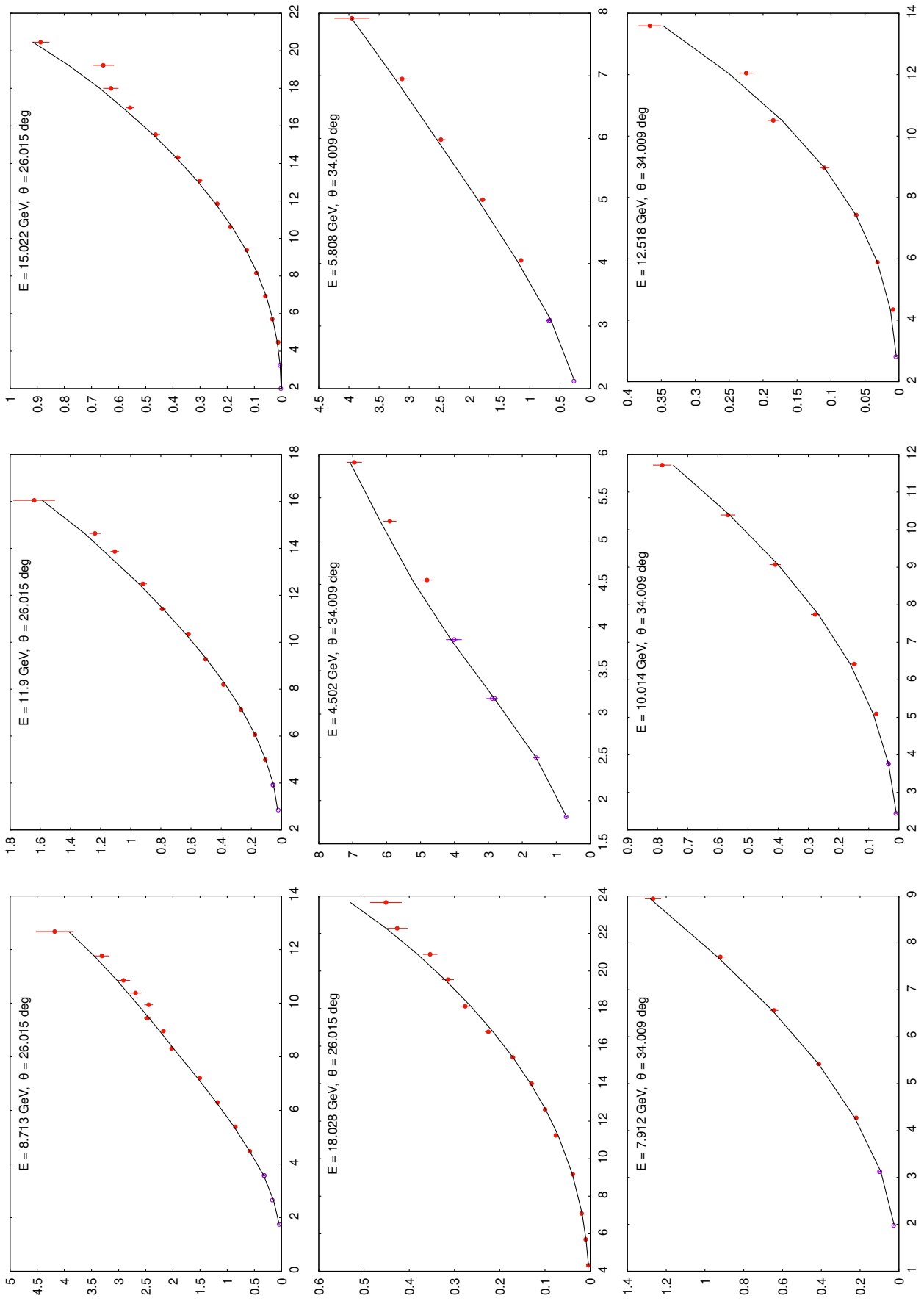


FIG. A3. Continued

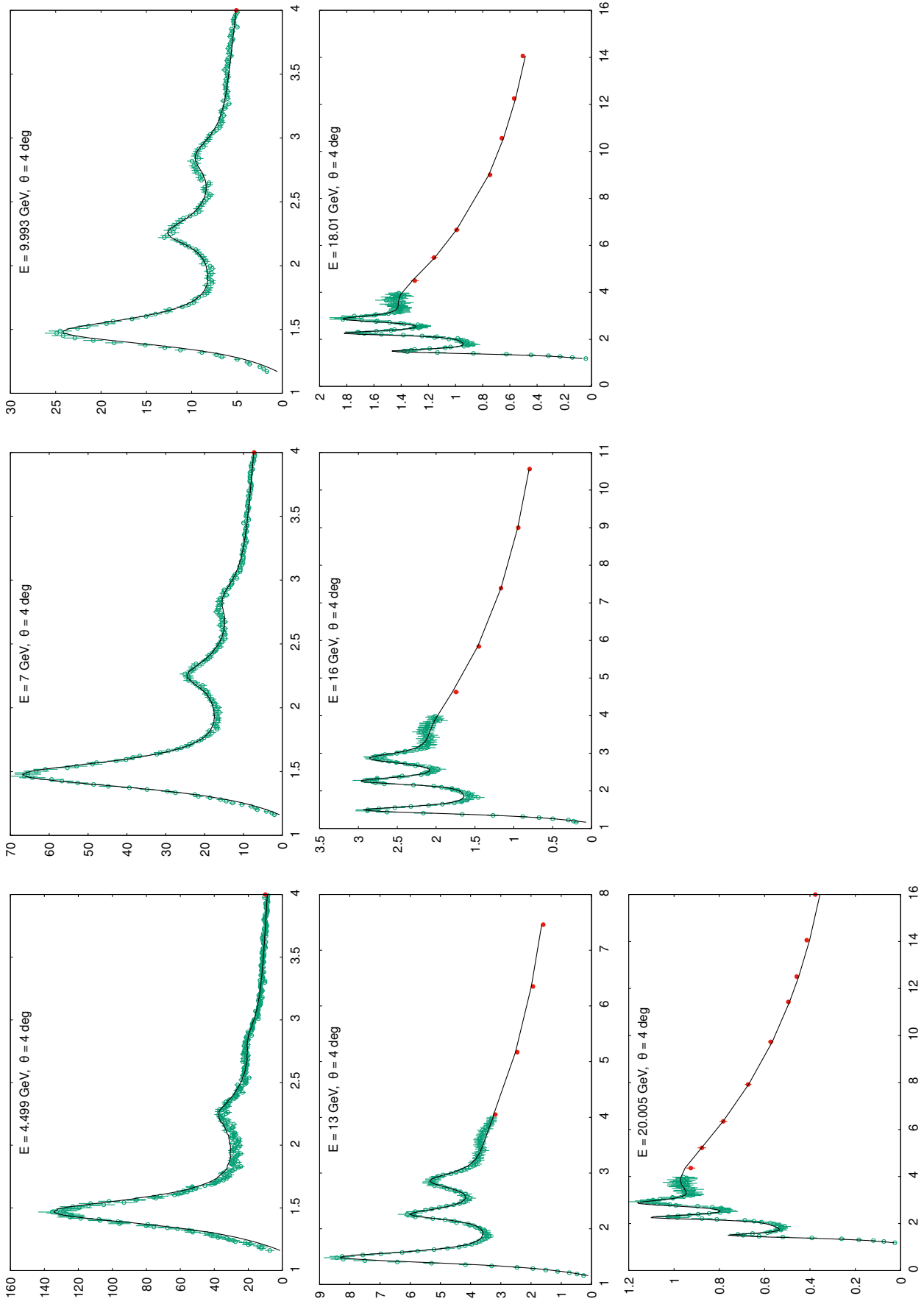


FIG. A4. (Color online) Comparison of our model (solid line) with SLAC-E61 data on differential cross section $d^2\sigma/(d\Omega dE')$ in nanobarn/(Sr GeV) vs. W^2 in GeV^2 . Beam energy and scattering angle value are given in the figure panels.

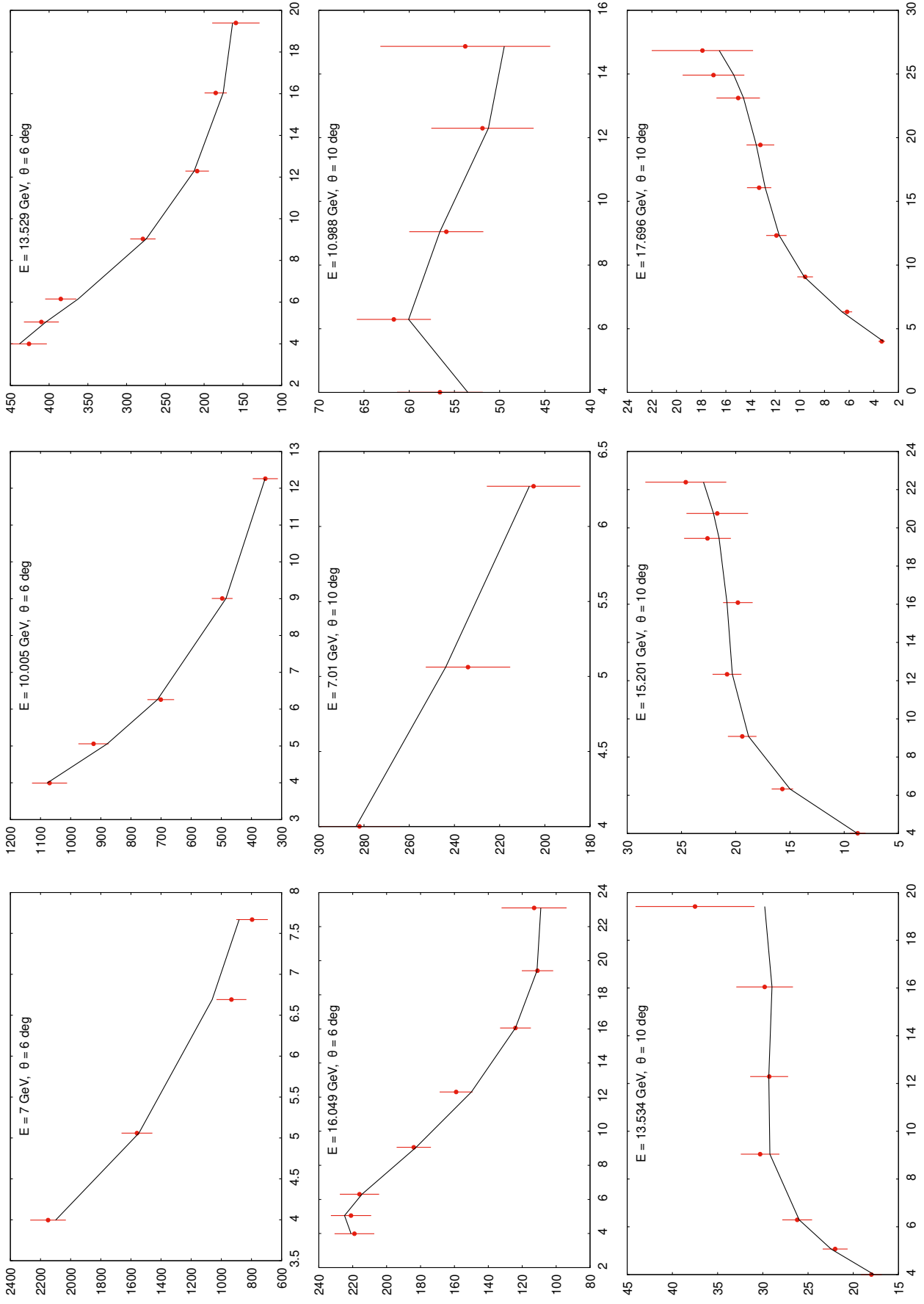


FIG. A5. (Color online) Comparison of our model (solid line) with SLAC-E004 data on differential cross section $d^2\sigma/(d\Omega dE')$ in nanobarn/(Sr GeV) vs. W^2 in GeV^2 . Beam energy and scattering angle value are given in the figure panels.

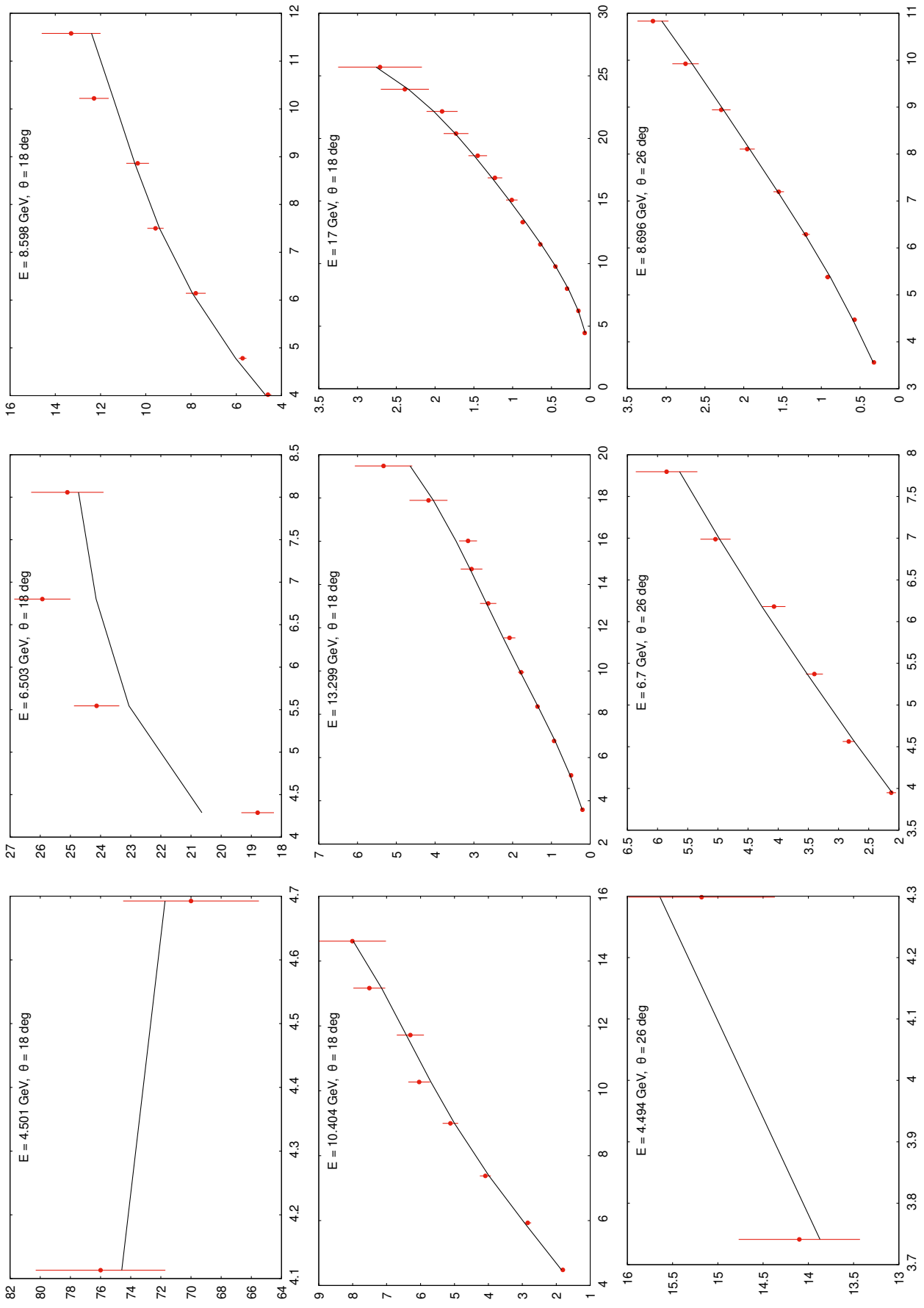


FIG. A5. Continued

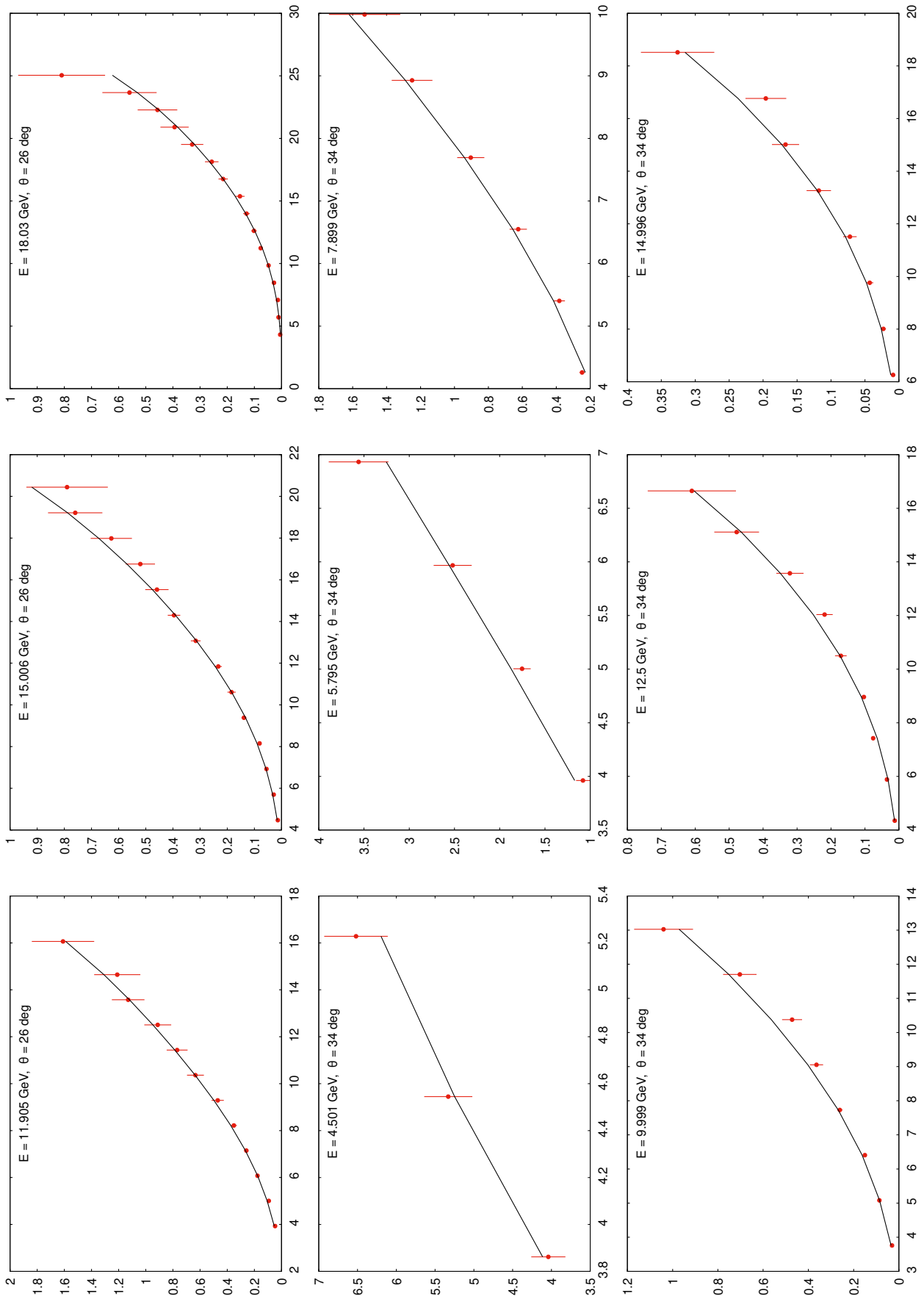


FIG. A5. Continued

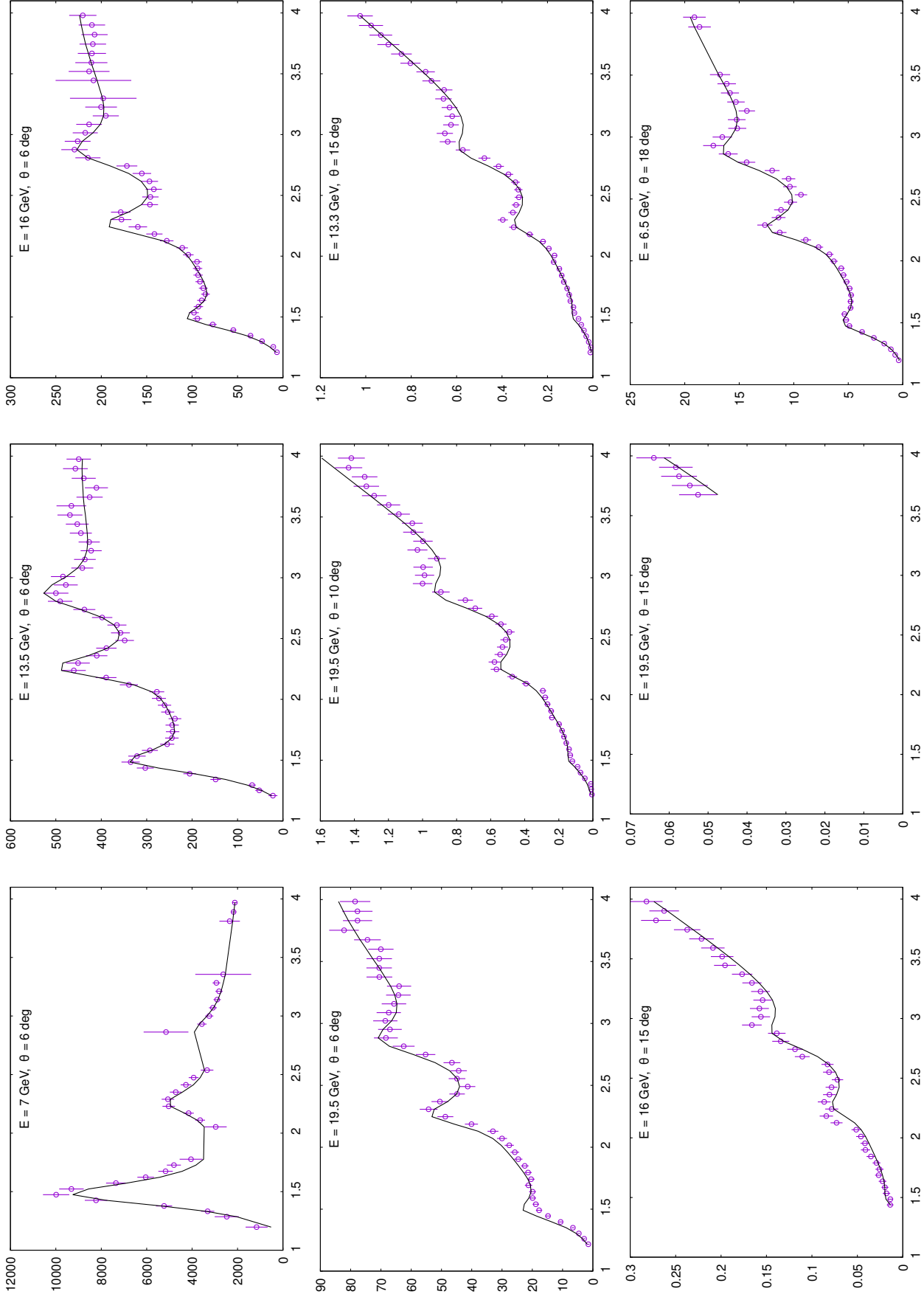


FIG. A6. (Color online) Comparison of our model (solid line) with SLAC-E8920 data on differential cross section $d^2\sigma / (d\Omega dE')$ in nanobarn / (Sr GeV) vs. W^2 in GeV^2 . Beam energy and scattering angle value are given in the figure panels.

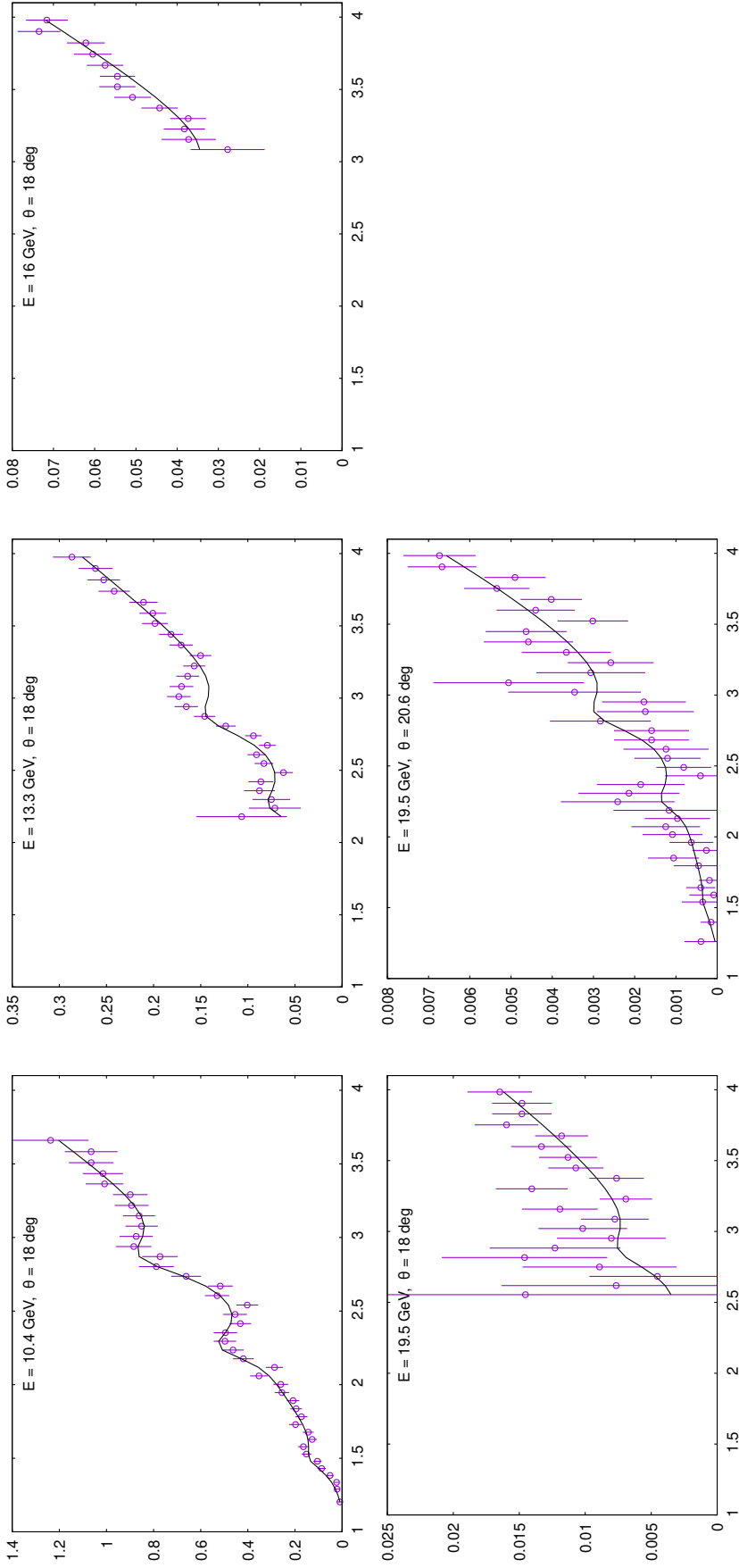


FIG. A6. Continued

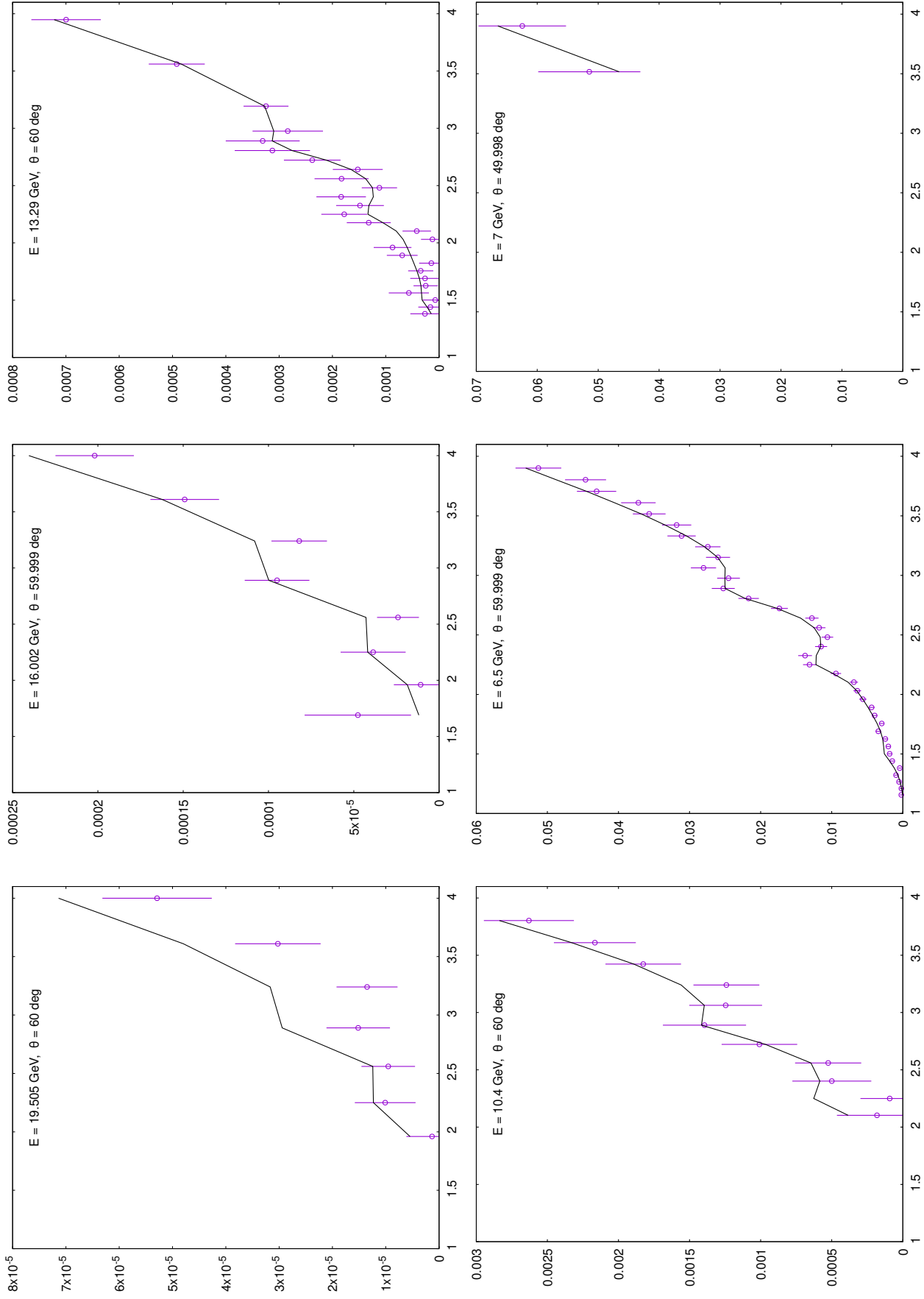


FIG. A7. (Color online) Comparison of our model (solid line) with SLAC-E891 data on differential cross section $d^2\sigma/(d\Omega dE')$ in nanobarn/(Sr GeV) vs. W^2 in GeV^2 . Beam energy and scattering angle value are given in the figure panels.

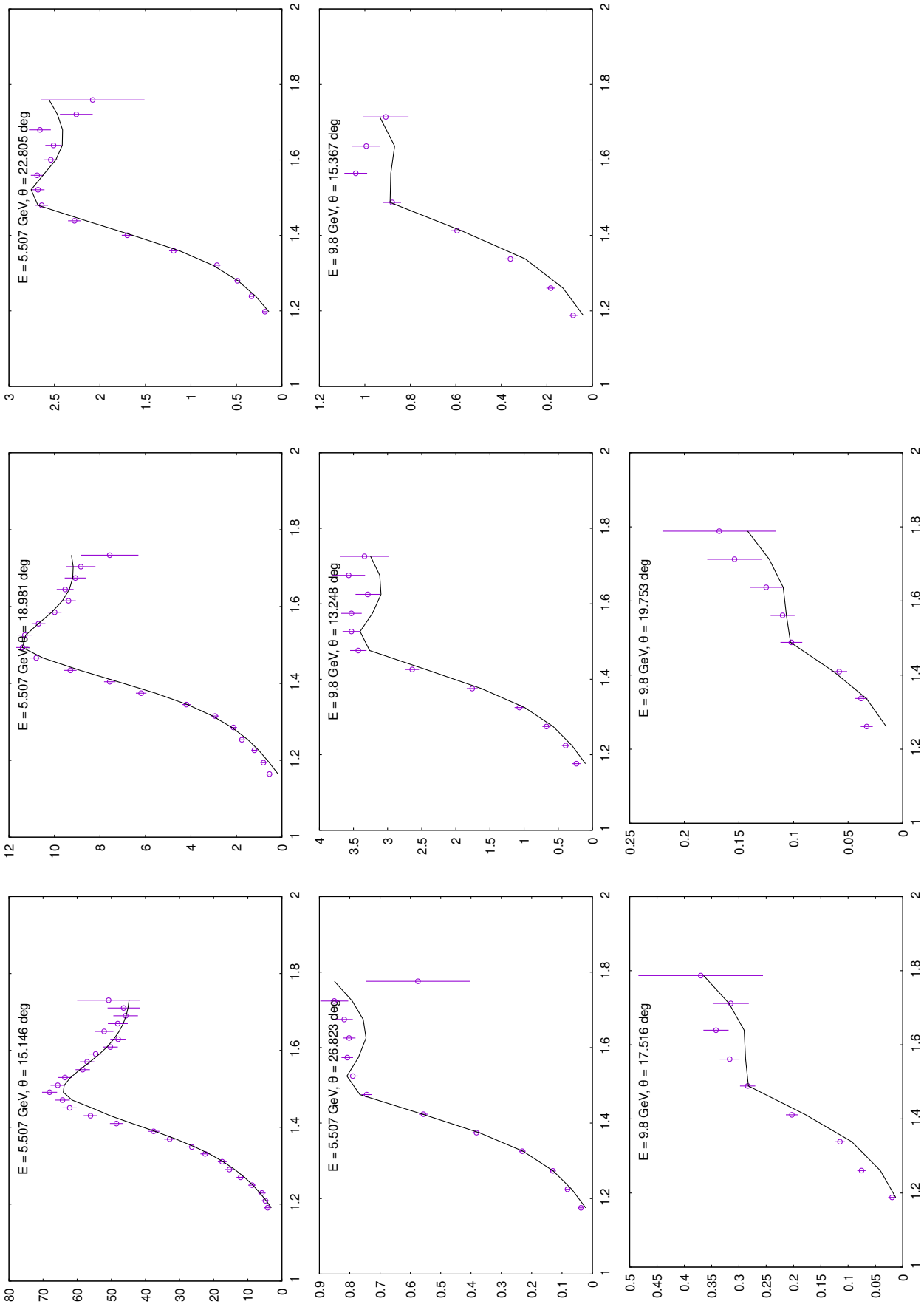


FIG. A8. (Color online) Comparison of our model (solid line) with SLAC-NE11 data on differential cross section $d^2\sigma / (d\Omega dE')$ in nanobarn / (Sr GeV) vs. W^2 in GeV^2 . Beam energy and scattering angle value are given in the figure panels.

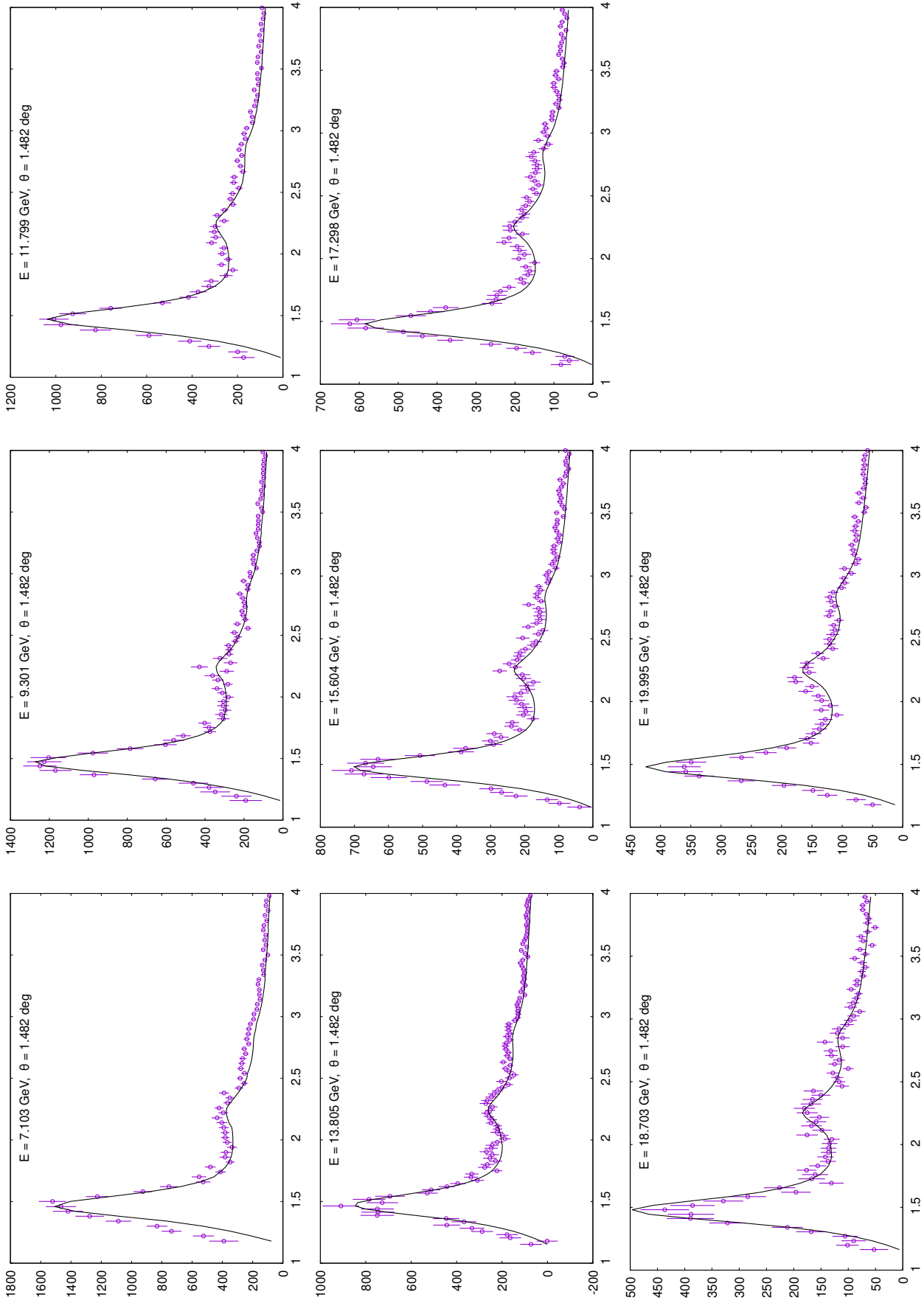


FIG. A9. (Color online) Comparison of our model (solid line) with SLAC-OnenHalf data on differential cross section $d^2\sigma/(d\Omega dE')$ in $\mu\text{b}/(\text{Sr GeV})$ vs. W^2 in GeV^2 . Beam energy and scattering angle value are given in the figure panels.

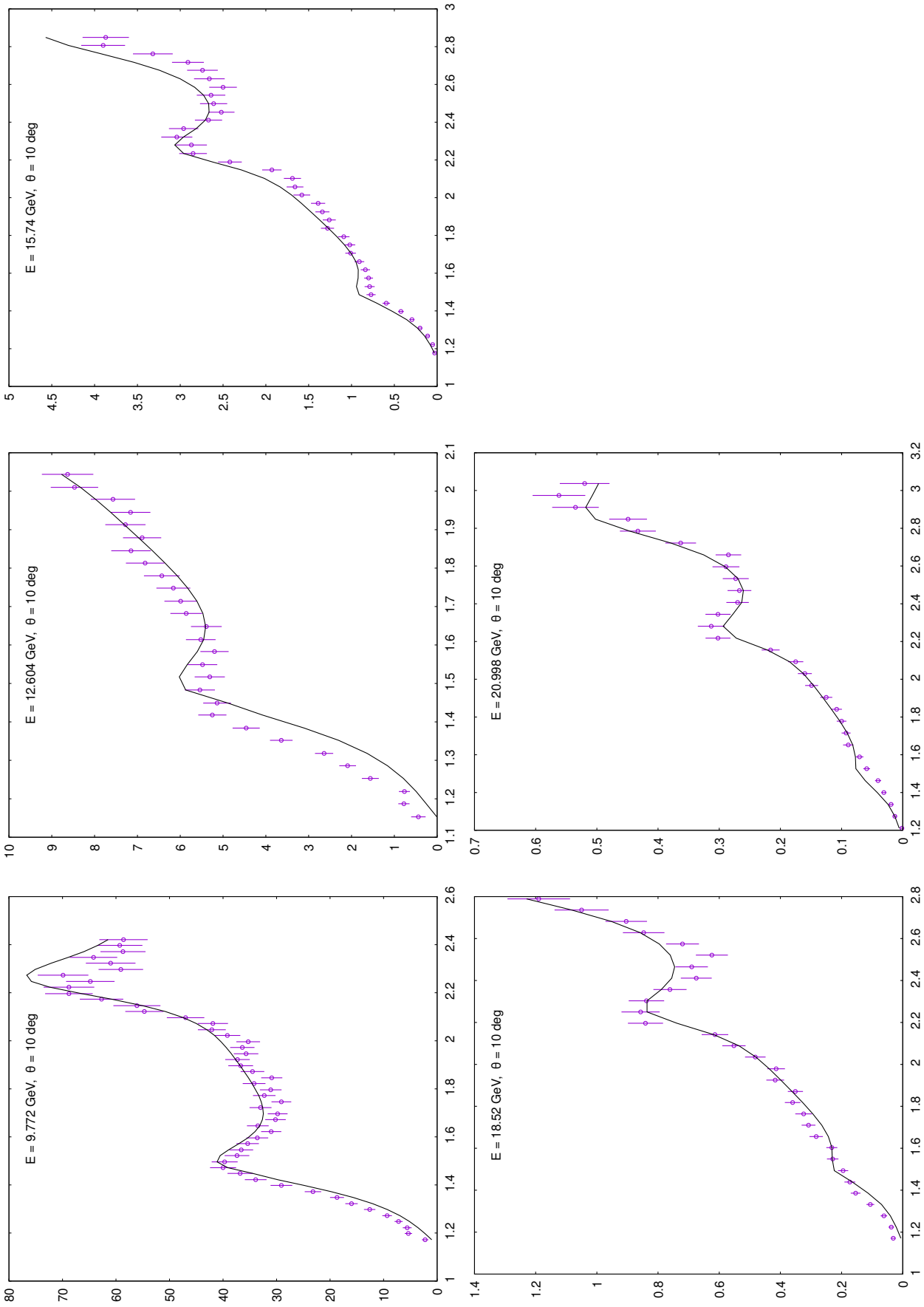


FIG. A10. (Color online) Comparison of our model (solid line) with SLAC-E133 data on differential cross section $d^2\sigma/(d\Omega dE')$ in nanobarn/(Sr GeV) vs. W^2 in GeV^2 . Beam energy and scattering angle value are given in the figure panels.

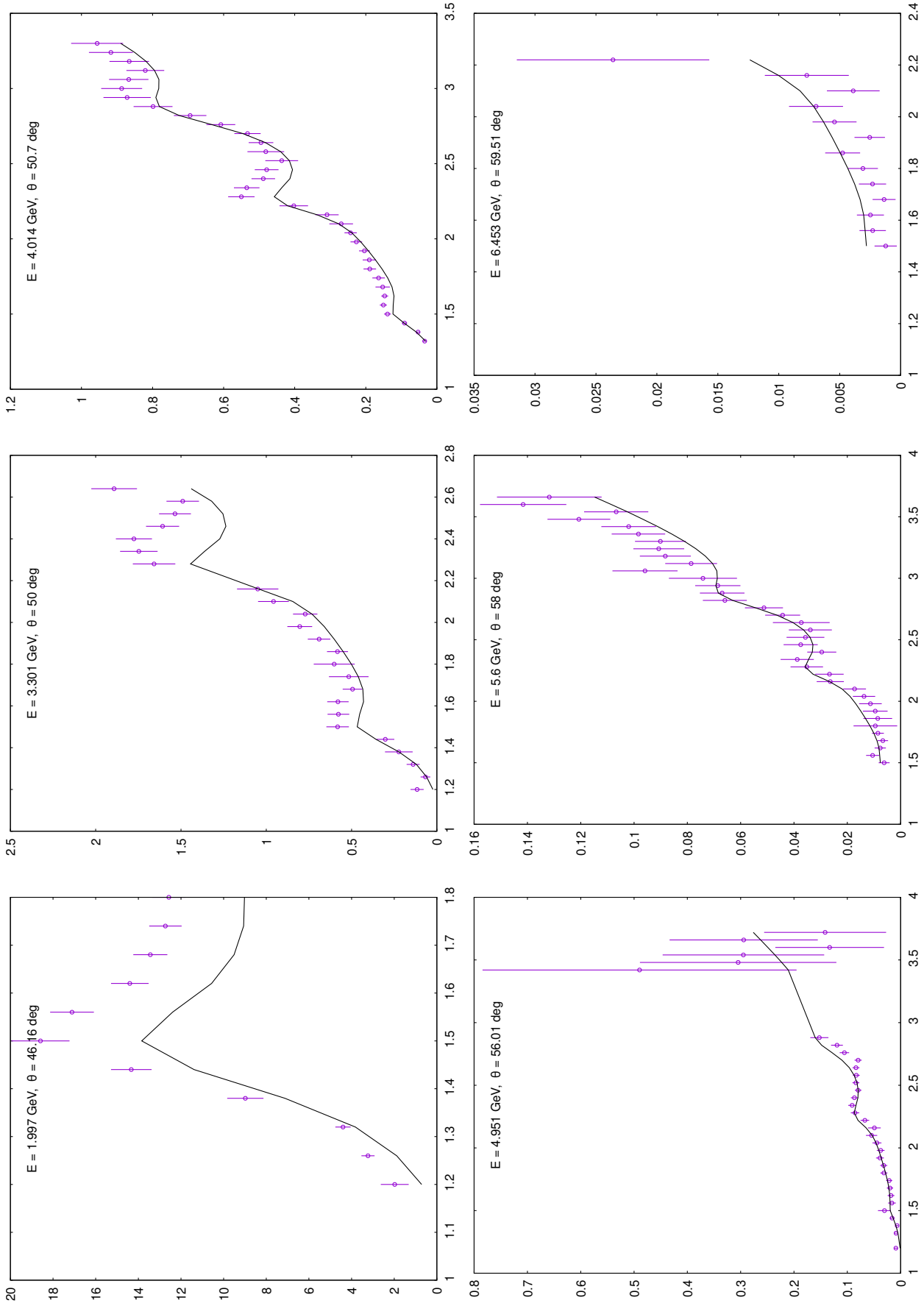


FIG. A11. (Color online) Comparison of our model (solid line) with SLAC-E140X data on differential cross section $d^2\sigma/(d\Omega dE')$ in nanobarn/(Sr GeV) vs. W^2 in GeV^2 . Beam energy and scattering angle value are given in the figure panels.

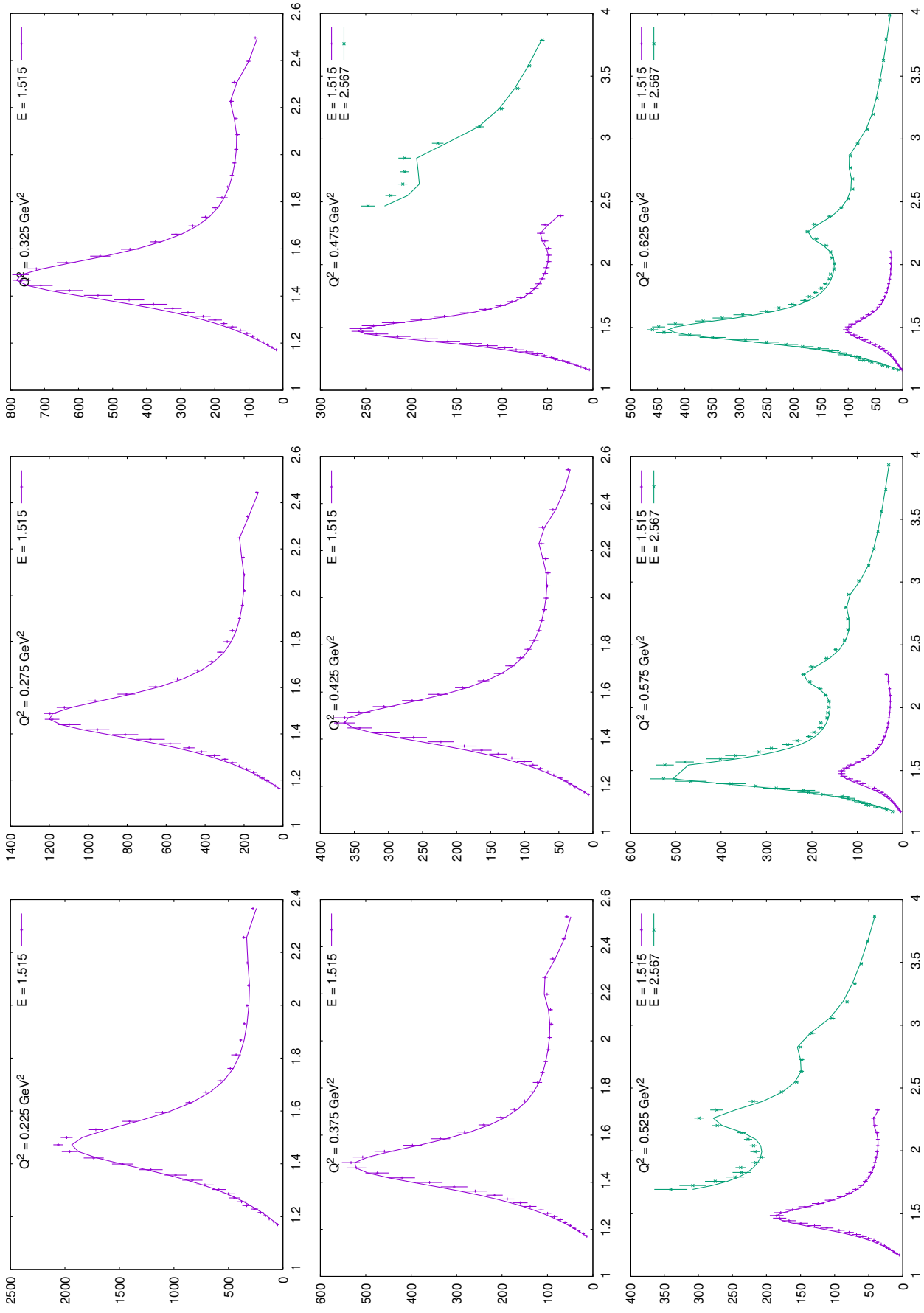


FIG. A12. (Color online) Comparison of our model (solid lines) with JLab-CLAS data on differential cross section $d^2\sigma/(d\Omega dE')$ in nanobarn/(Sr GeV) vs. W^2 in GeV^2 . The value of the beam energy and Q^2 bin are given in the figure panels.

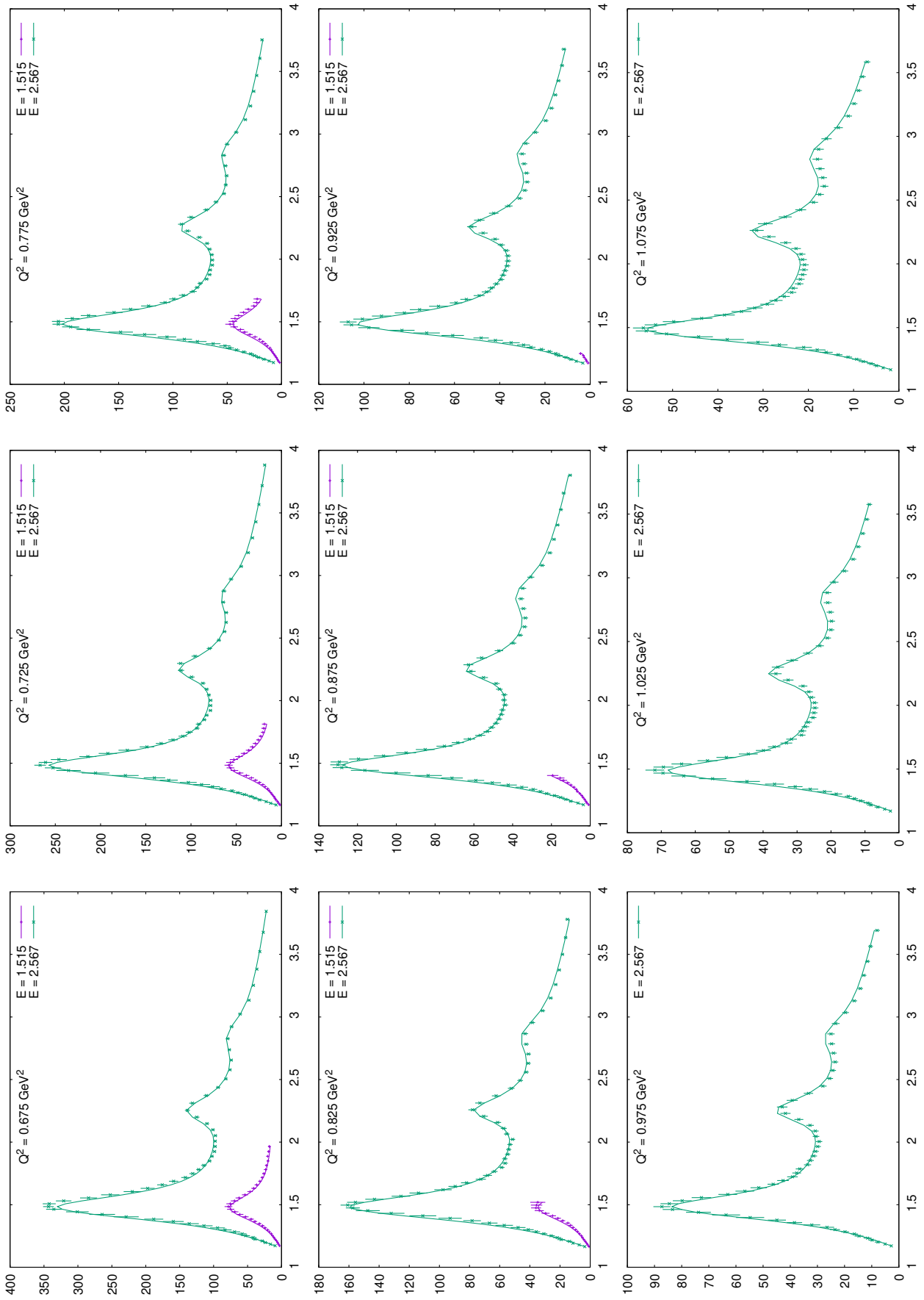


FIG. A12. Continued

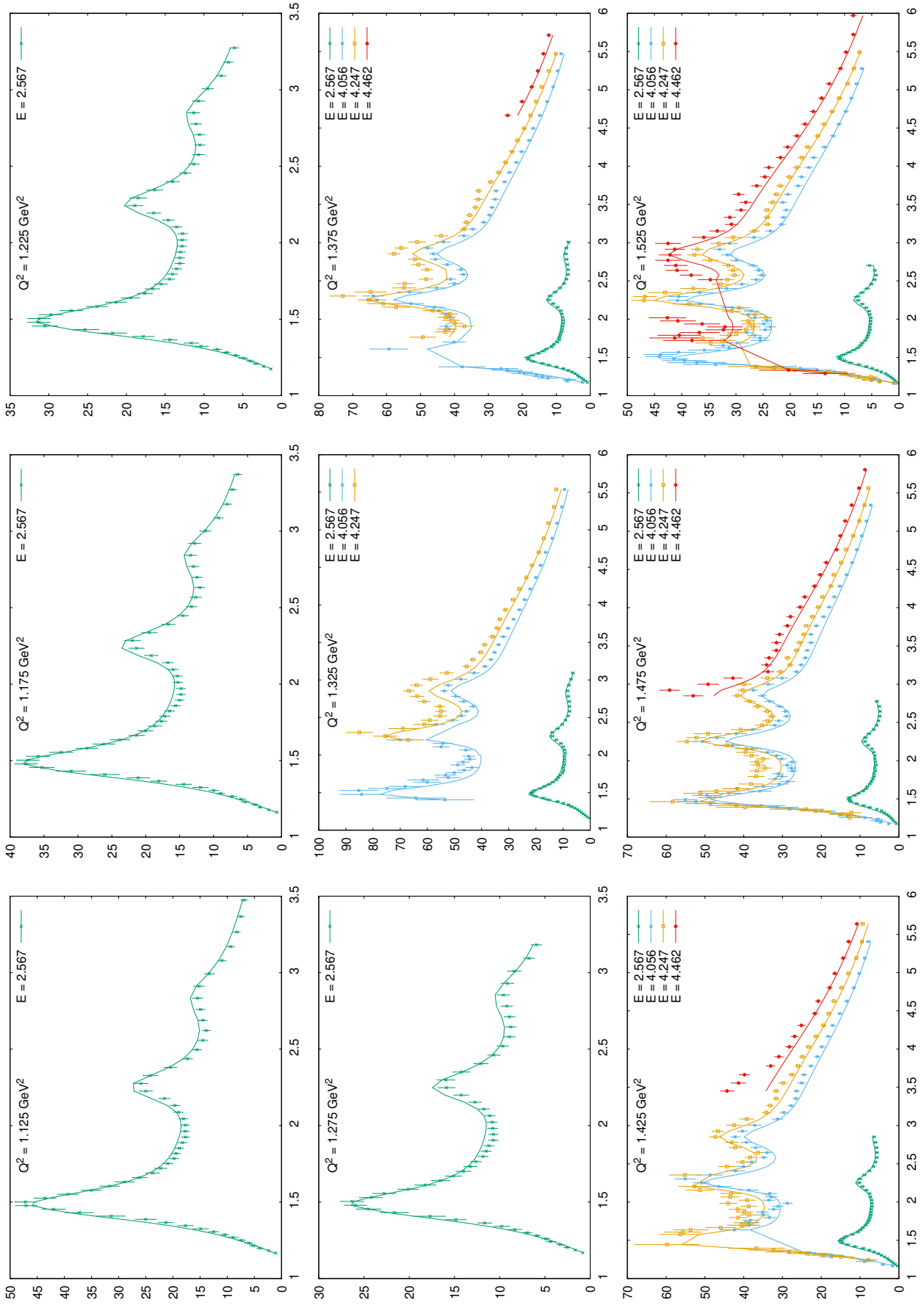


FIG. A12. Continued

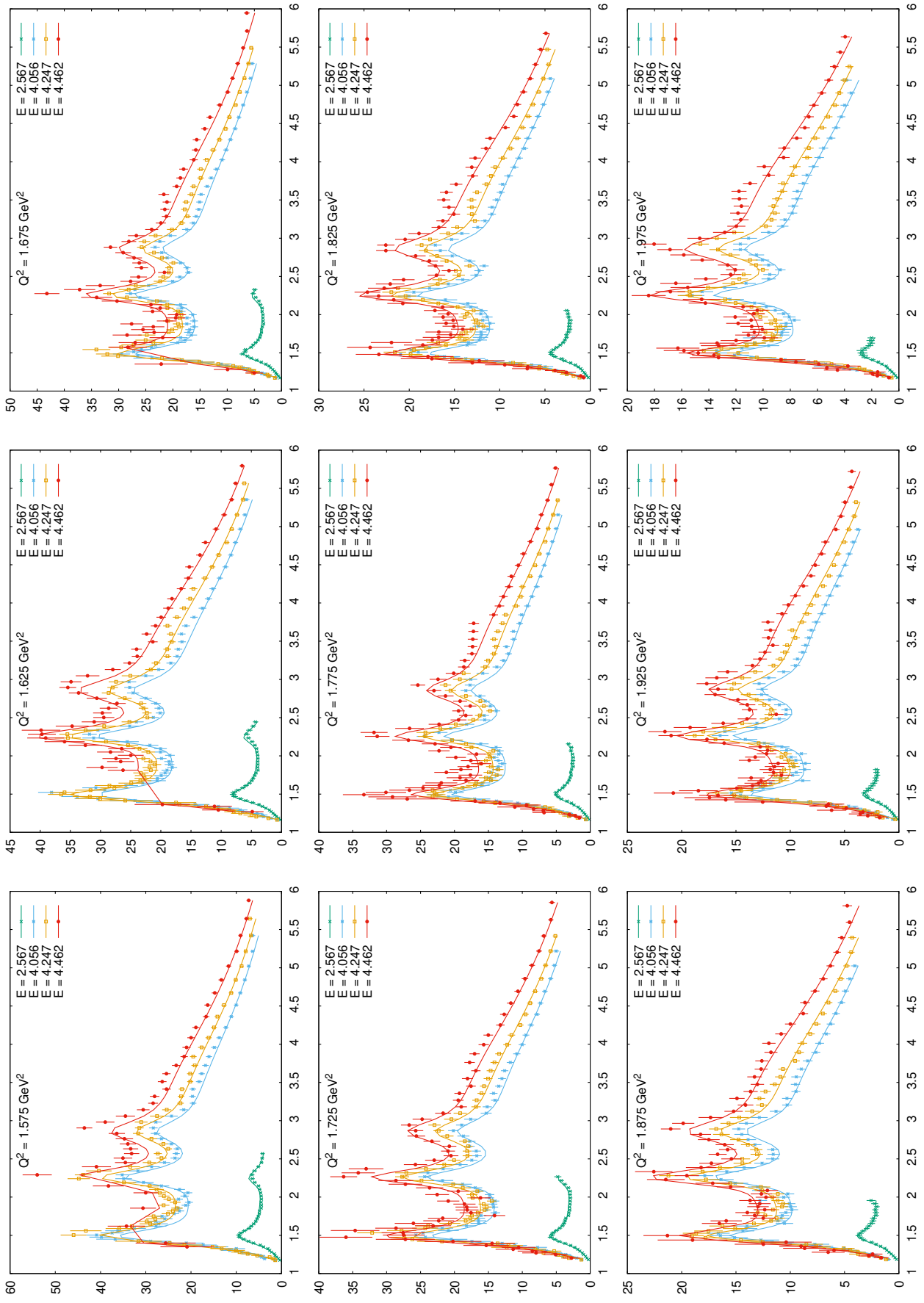


FIG. A12. Continued

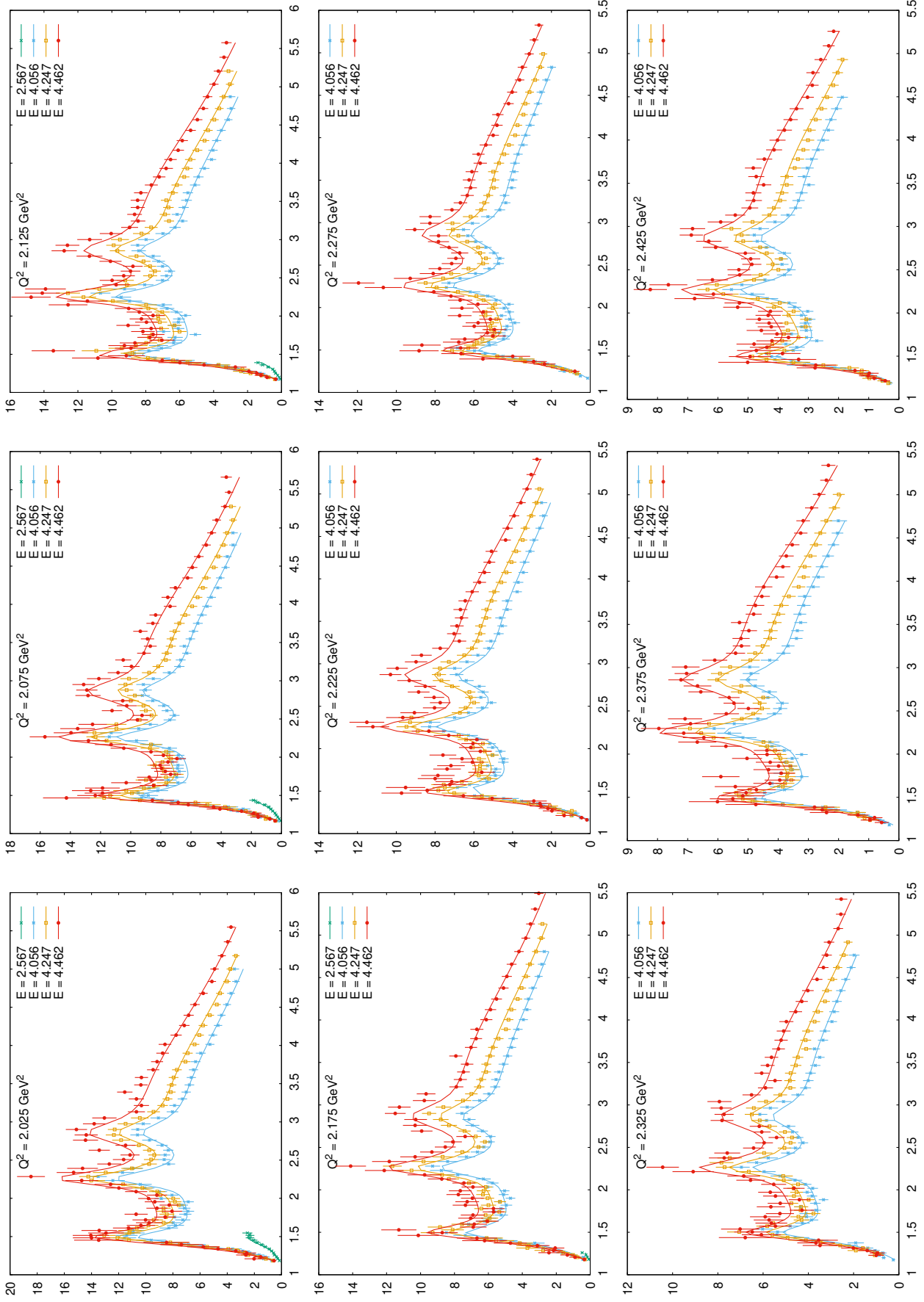


FIG. A12. Continued

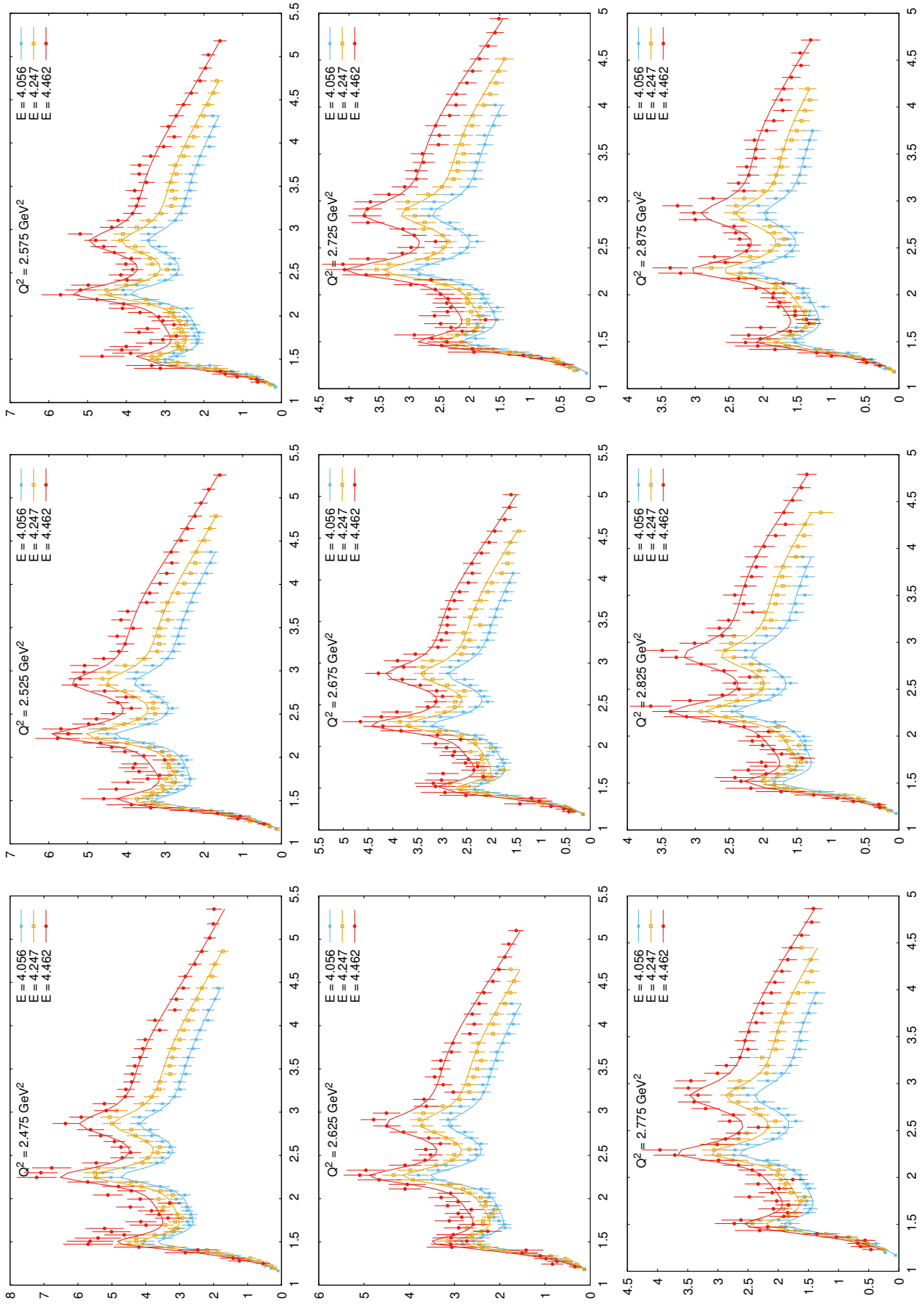


FIG. A12. Continued

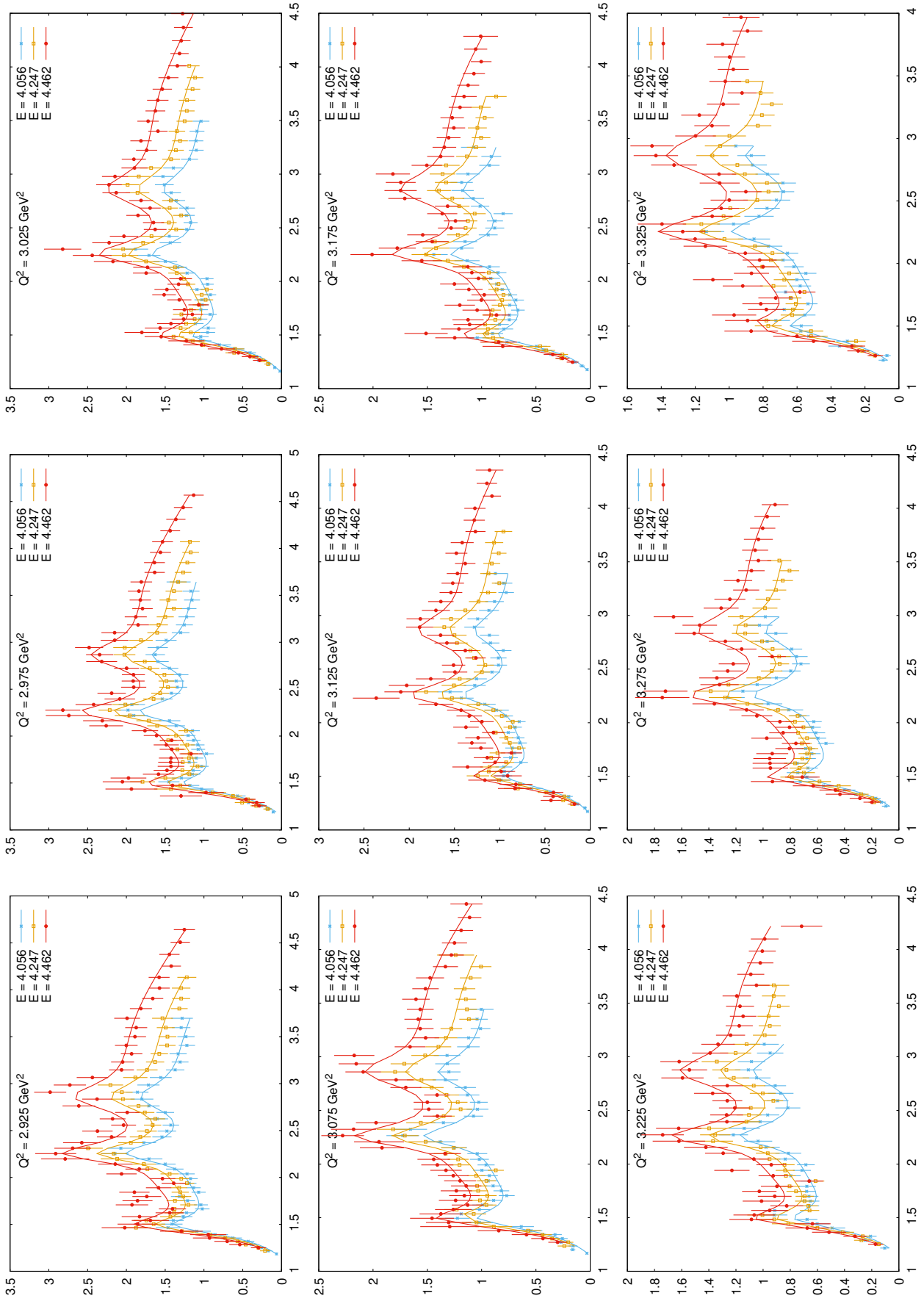


FIG. A12. Continued

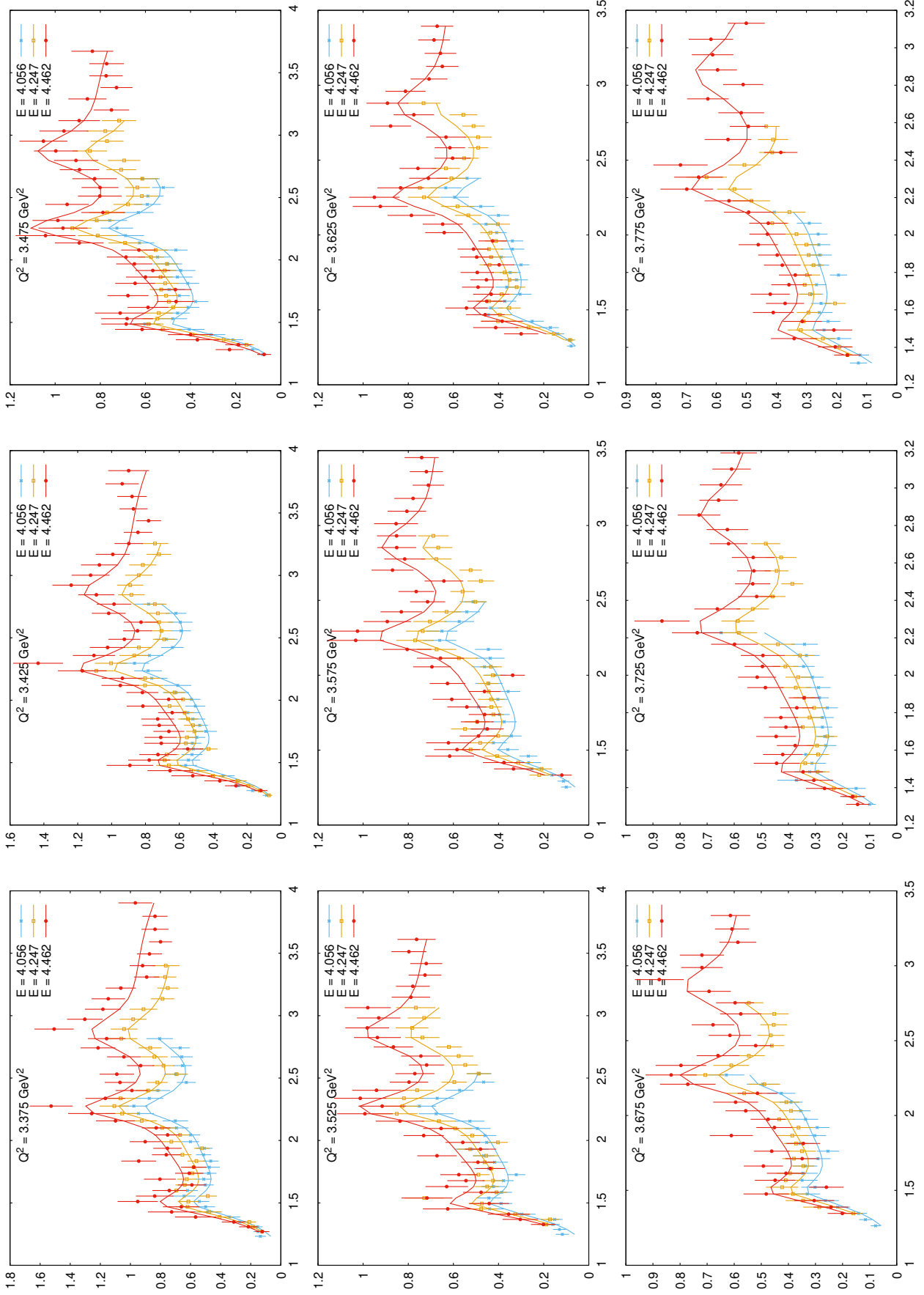


FIG. A12. Continued

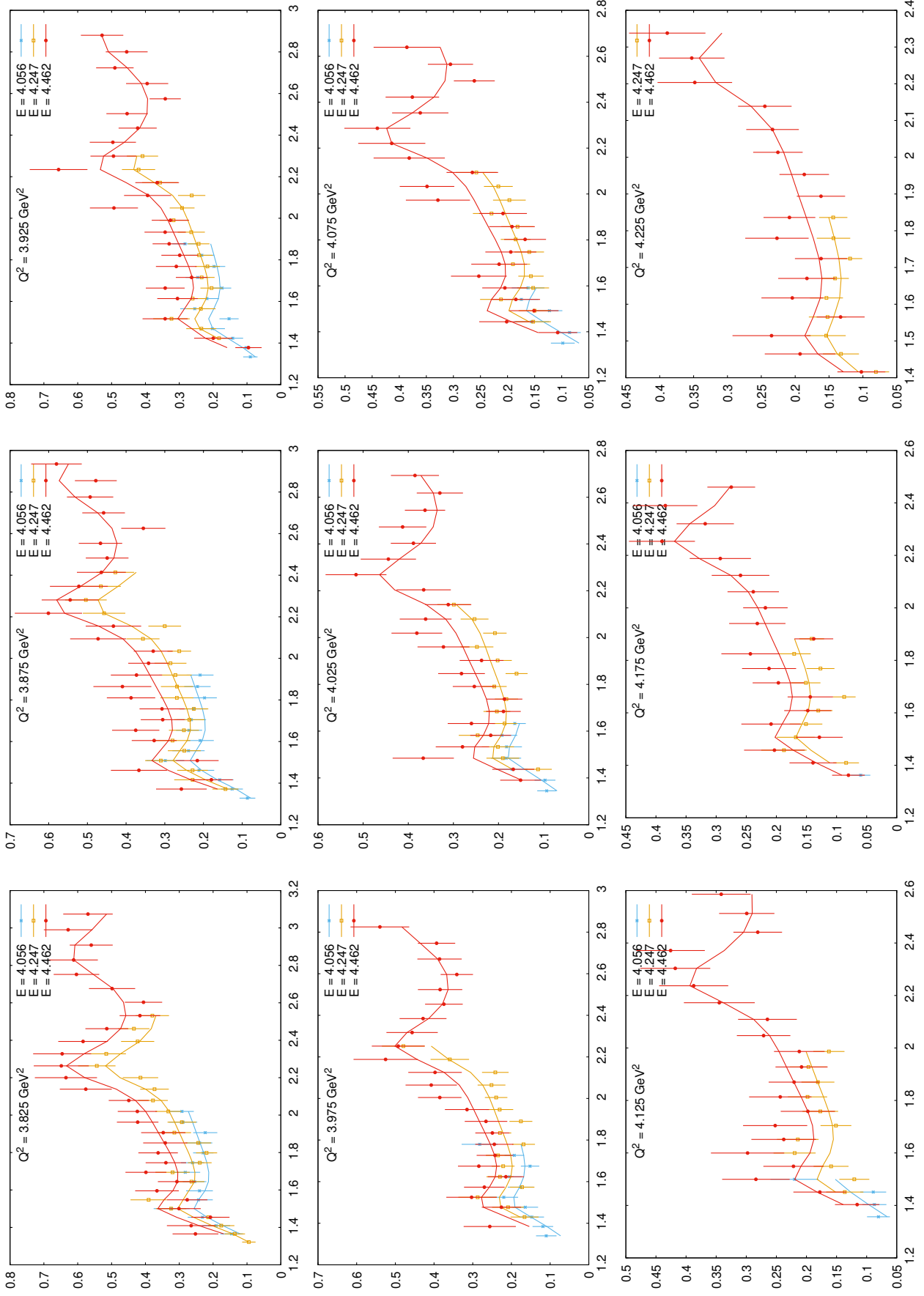


FIG. A12. Continued

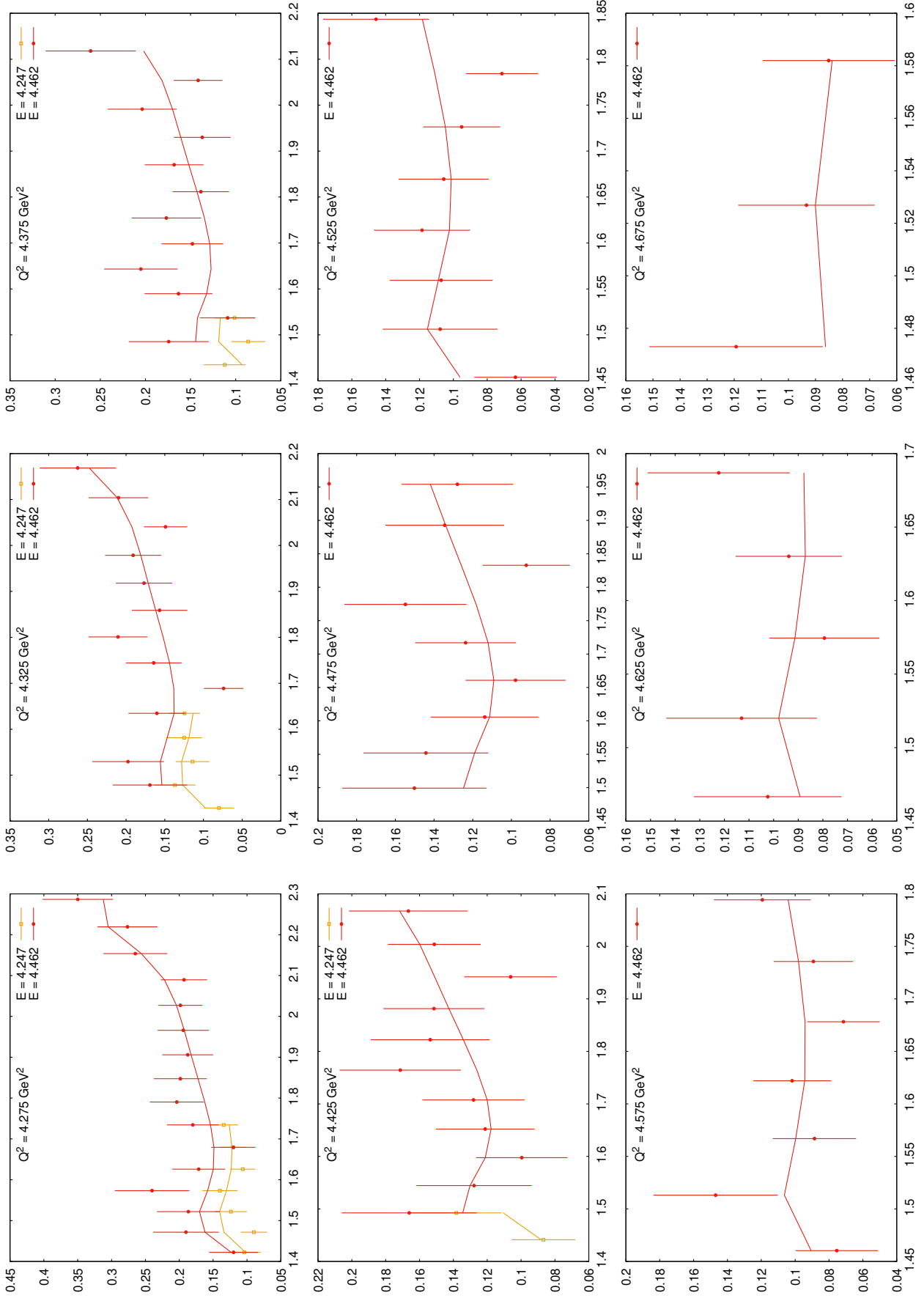


FIG. A12. Continued

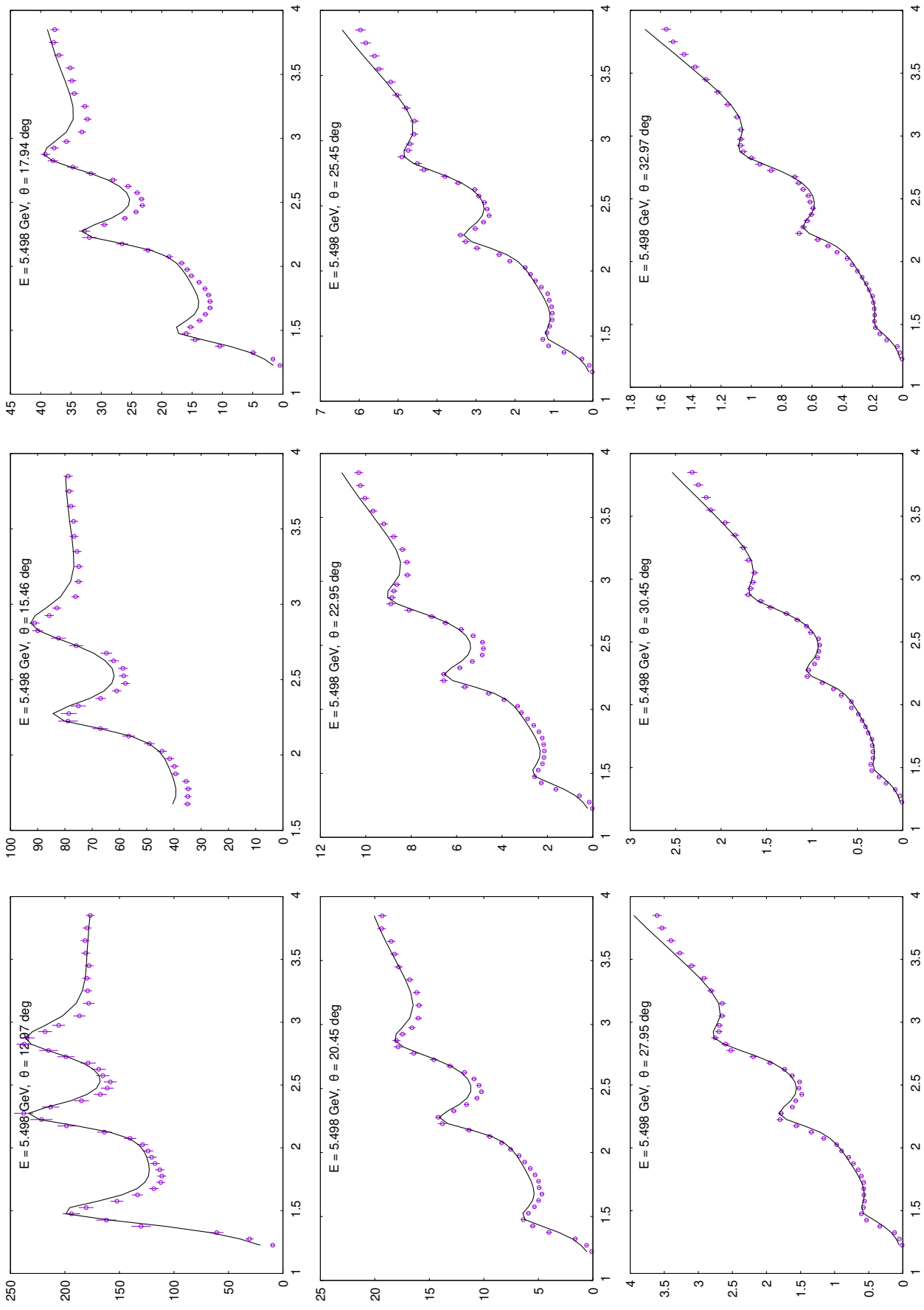


FIG. A13. (Color online) Comparison of our model (solid line) with JLab-E94-110 data on differential cross section $d^2\sigma/(d\Omega dE')$ in nanobarn/(Sr GeV) vs. W^2 in GeV^2 . Beam energy and scattering angle value are given in the figure panels.

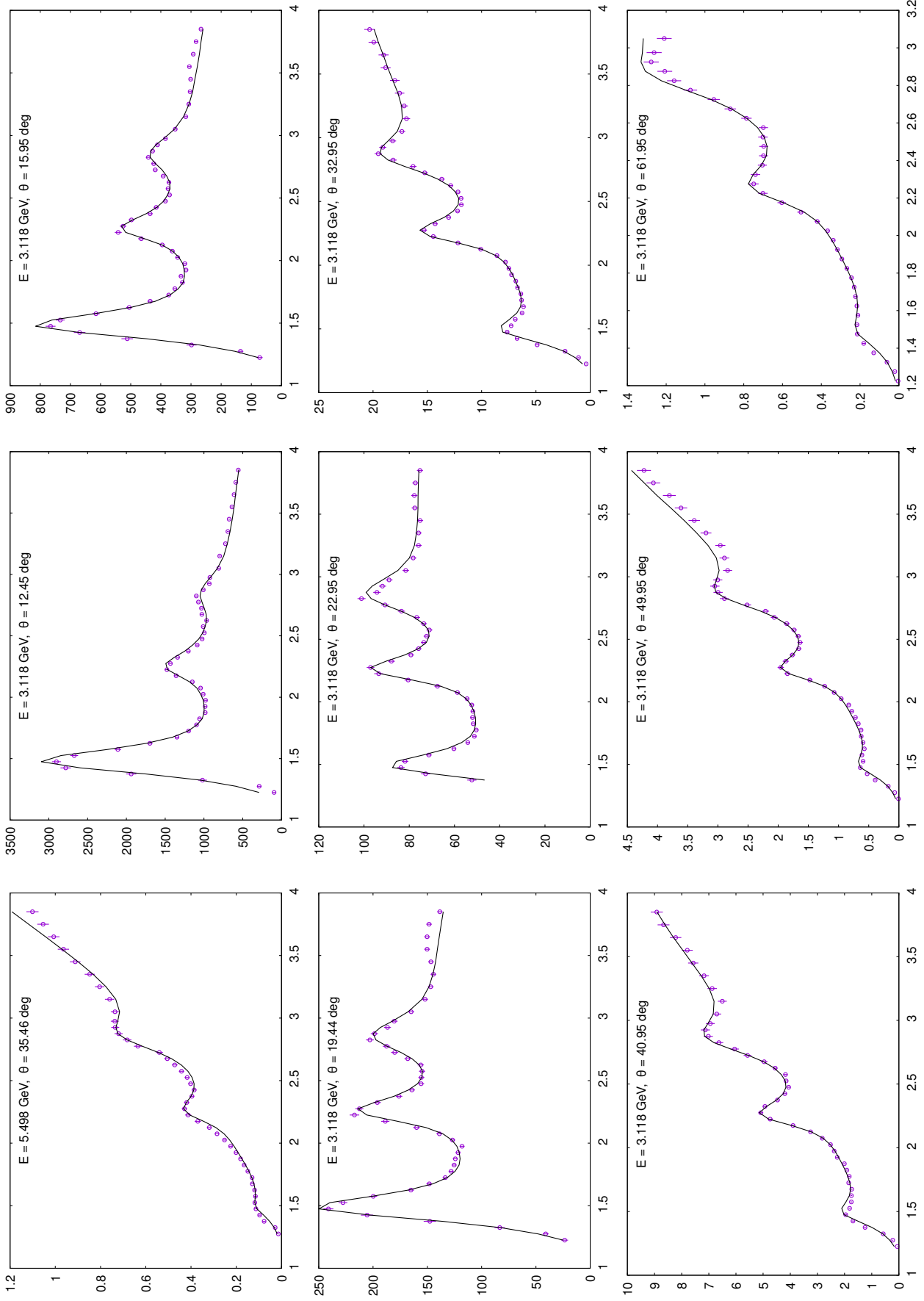


FIG. A13. Continued

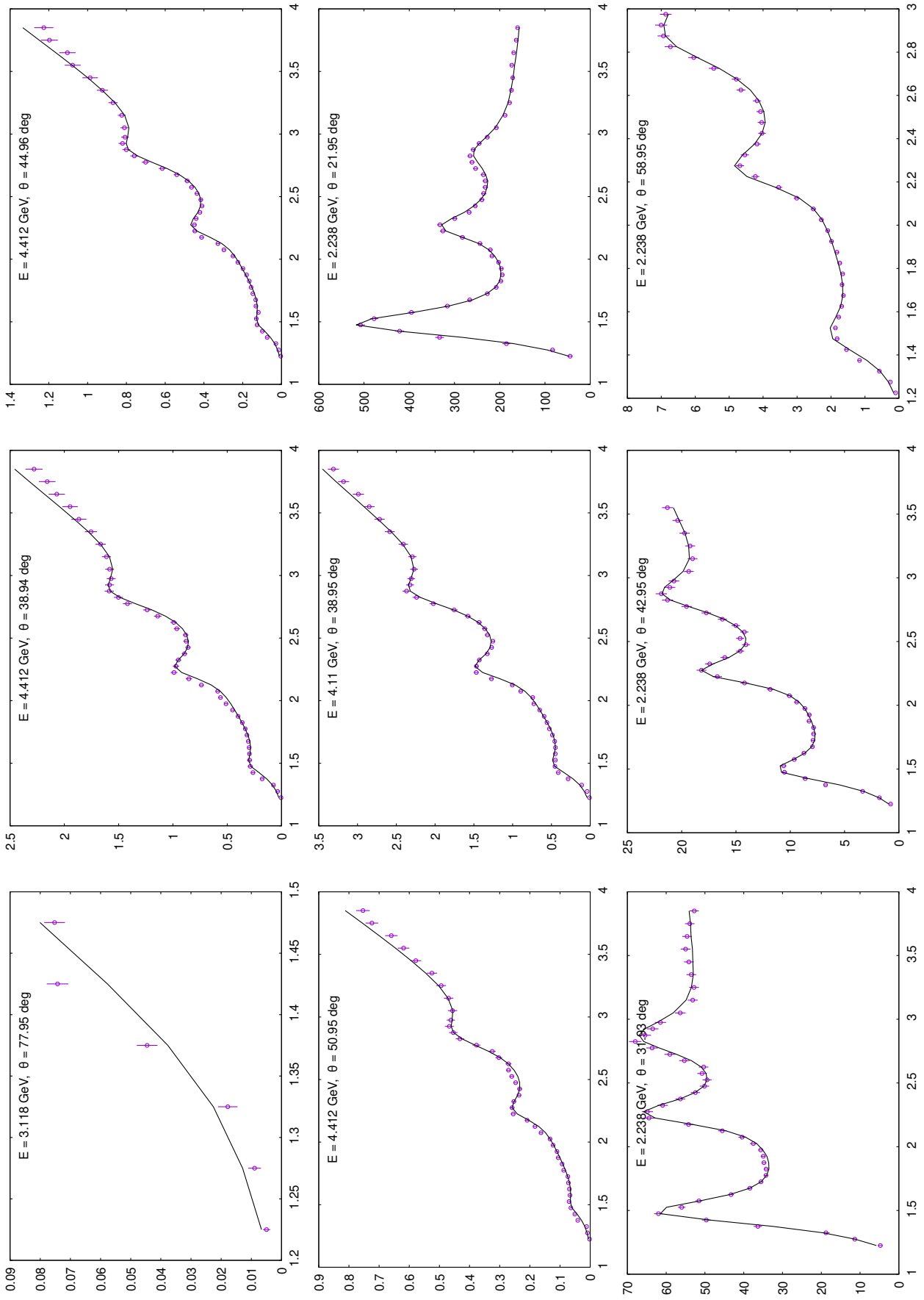


FIG. A13. Continued

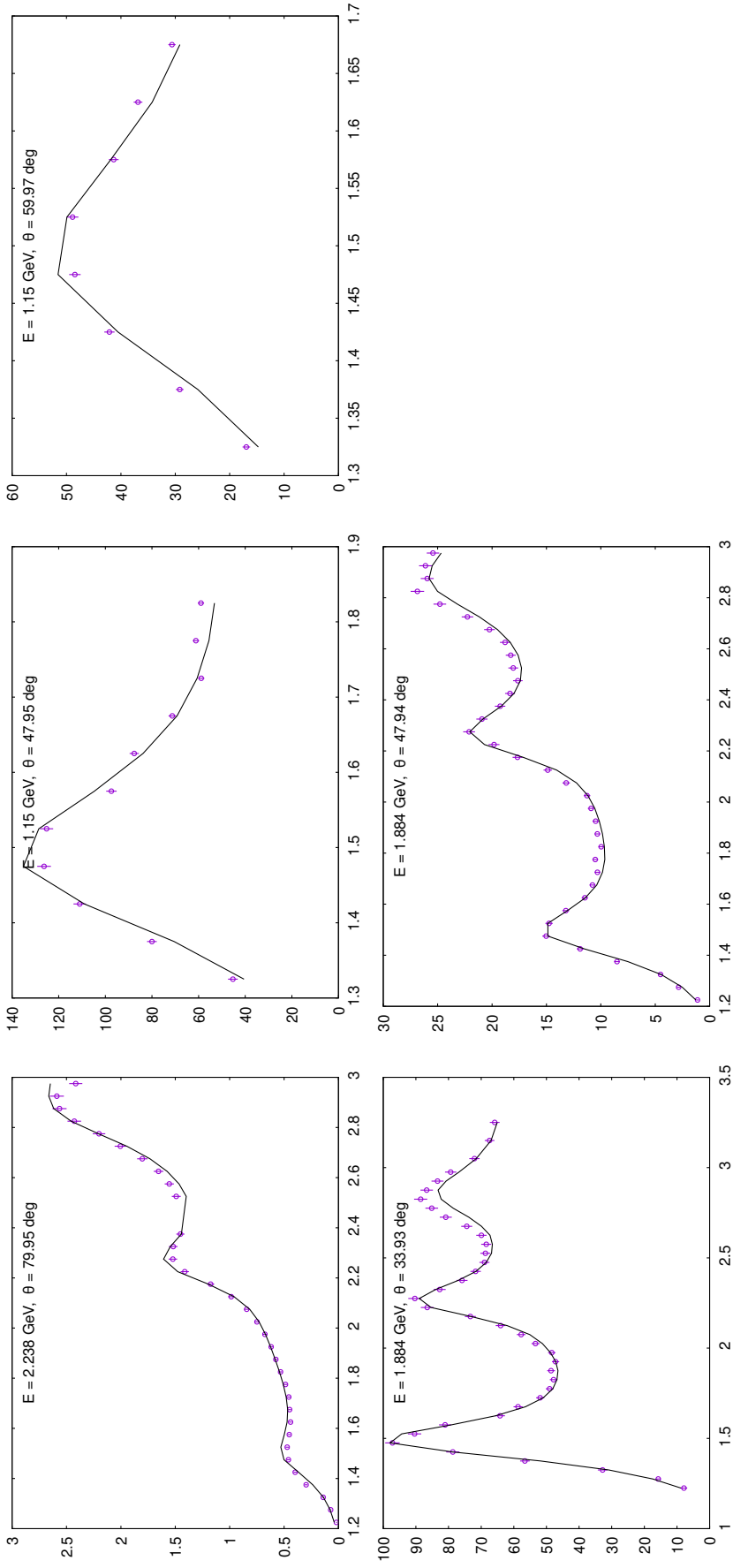


FIG. A13. Continued

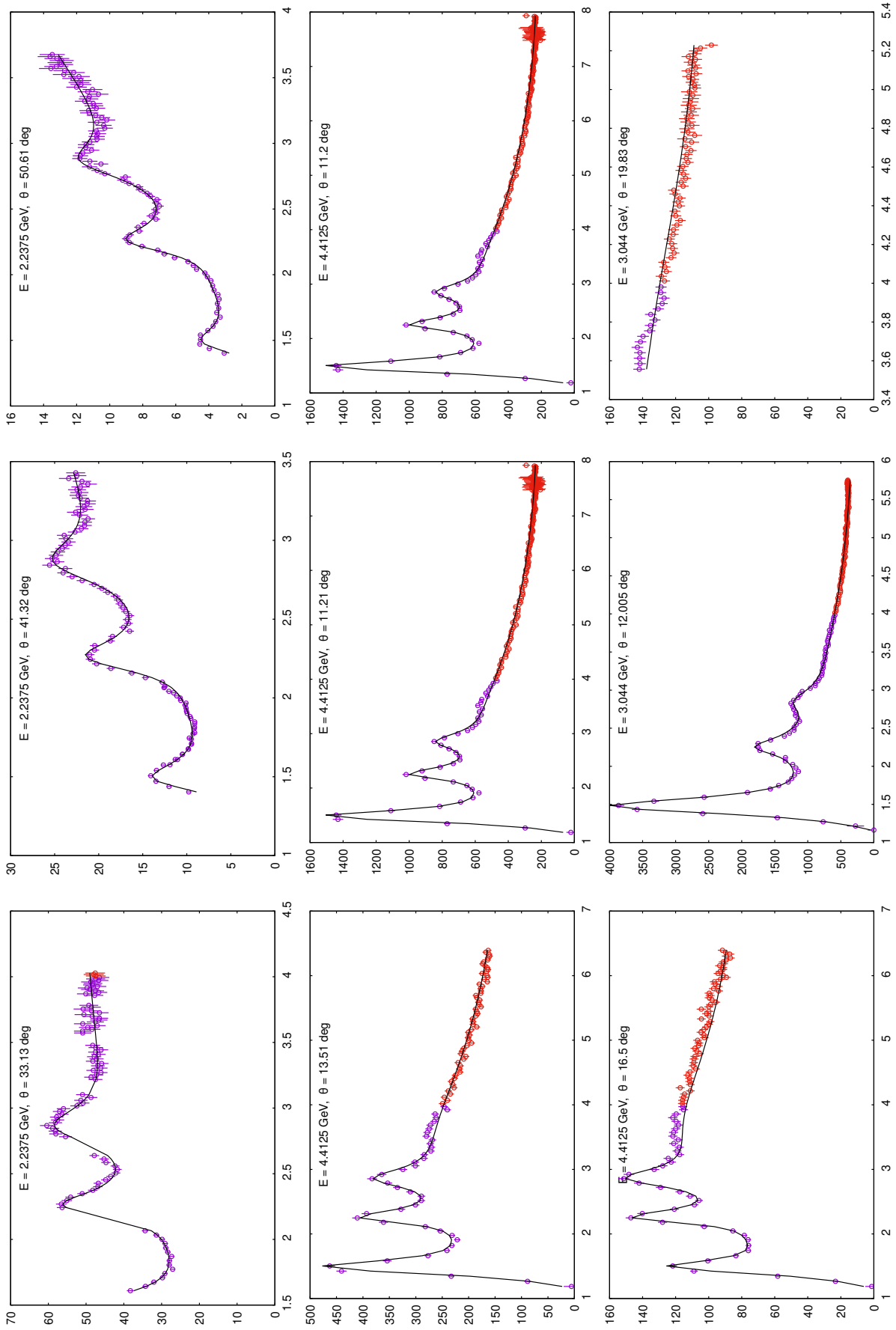


FIG. A14. (Color online) Comparison of our model (solid line) with JLab-E00-002 data on differential cross section $d^2\sigma/(d\Omega dE')$ in nanobarn/(Sr GeV) vs. W^2 in GeV^2 . Beam energy and scattering angle value are given in the figure panels.

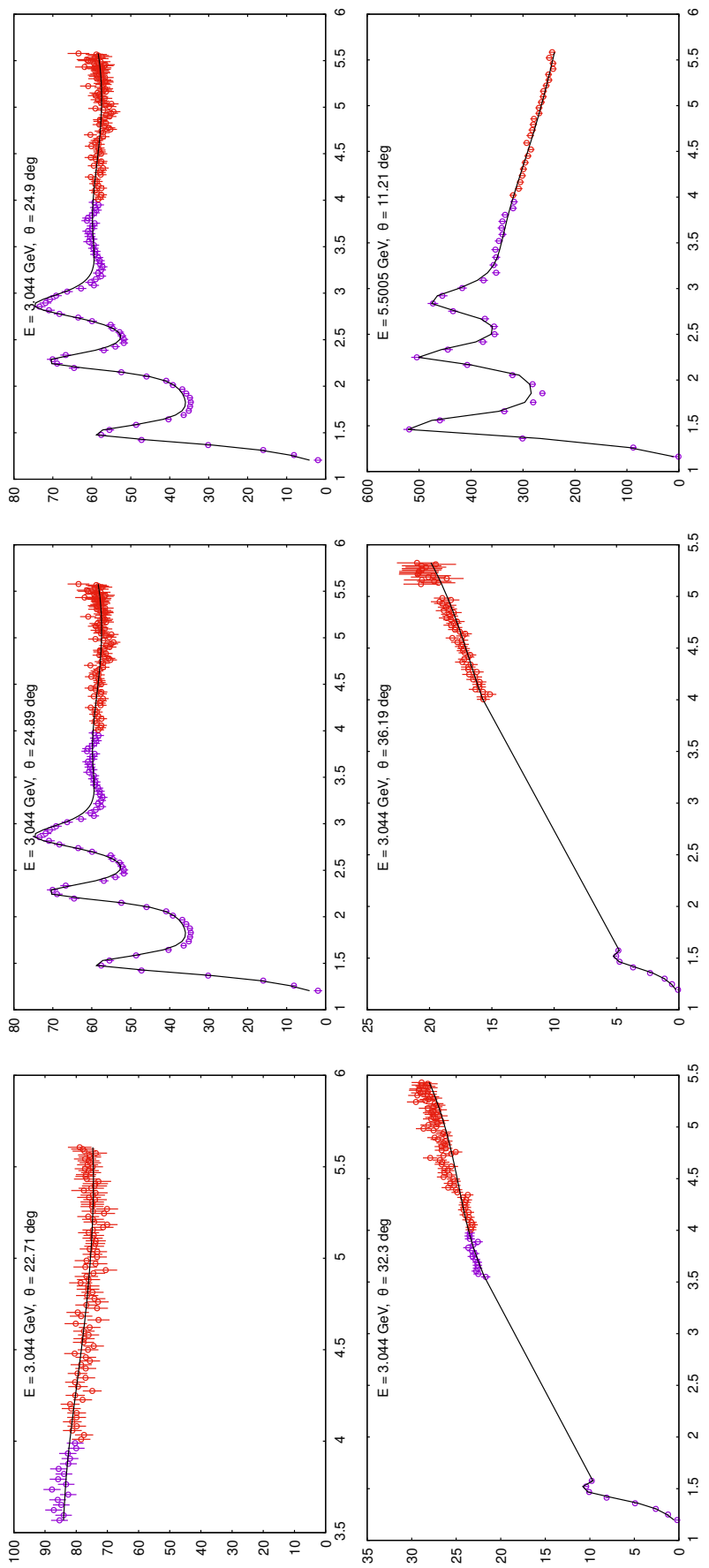


FIG. A14. Continued

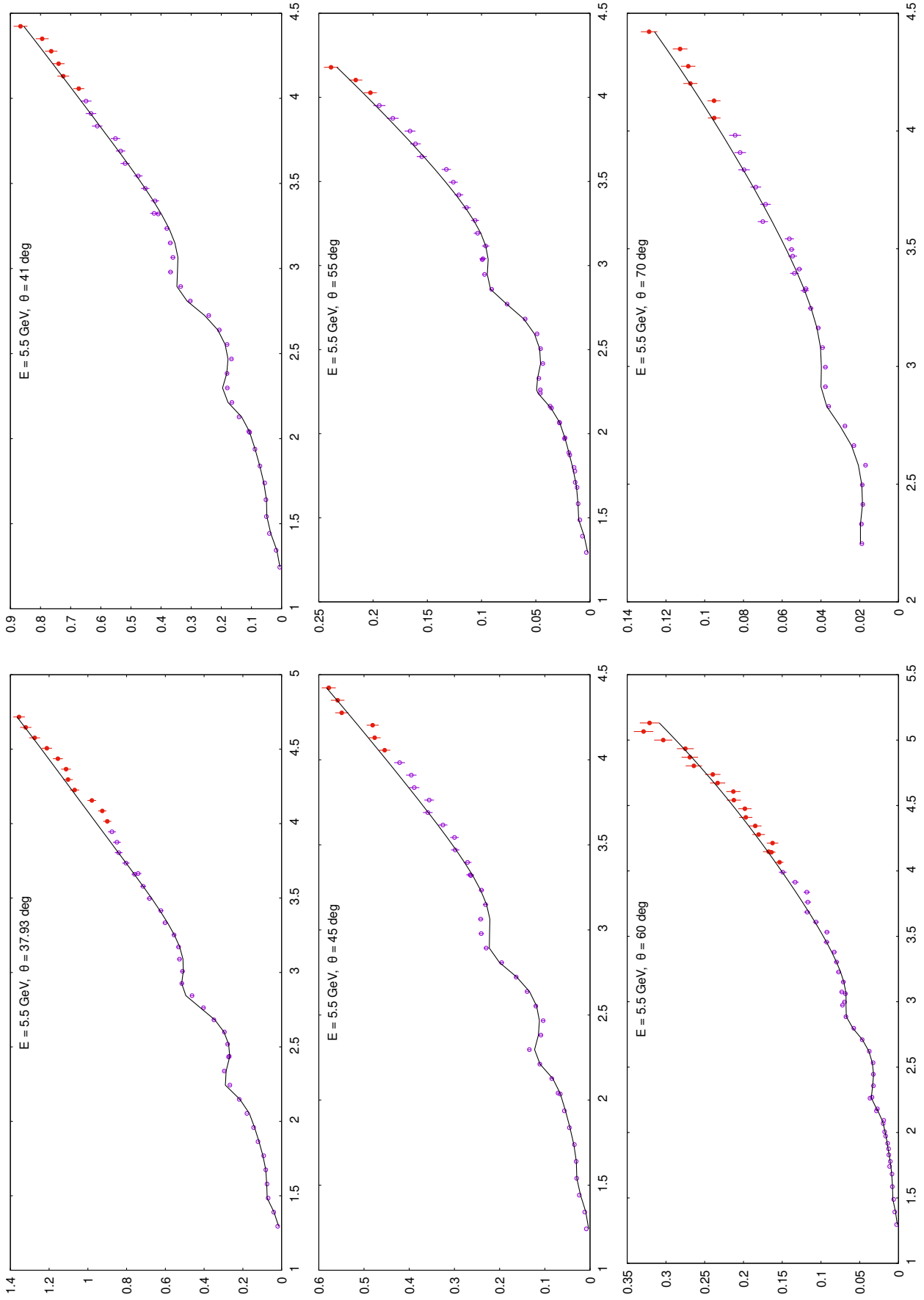


FIG. A15. (Color online) Comparison of our model (solid line) with JLab-E00-116 data on differential cross section $d^2\sigma / (d\Omega dE')$ in nanobarn/(Sr GeV) vs. W^2 in GeV^2 . Beam energy and scattering angle value are given in the figure panels.

-
- [1] A. Accardi *et al.*, “A critical appraisal and evaluation of modern PDFs,” *Eur. Phys. J.* **C76**, 471 (2016), [arXiv:1603.08906 \[hep-ph\]](#).
- [2] J. Gao, L. Harland-Lang, and J. Rojo, “The structure of the proton in the LHC precision era,” *Phys. Rept.* **742**, 1–121 (2018), [arXiv:1709.04922 \[hep-ph\]](#).
- [3] R. L. Walker, “Phenomenological analysis of single pion photoproduction,” *Phys. Rev.* **182**, 1729–1748 (1969).
- [4] D. Drechsel, O. Hanstein, S. Kamalov, and L. Tiator, “A unitary isobar model for pion photoproduction and electroproduction on the proton up to 1-GeV,” *Nucl. Phys.* **A645**, 145–174 (1999), [arXiv:nucl-th/9807001](#).
- [5] M. E. Christy and P. E. Bosted, “Empirical fit to precision inclusive electron-proton cross sections in the resonance region,” *Phys. Rev.* **C81**, 055213 (2010), [arXiv:0712.3731 \[hep-ph\]](#).
- [6] A. N. Hiller Blin *et al.*, “Nucleon resonance contributions to unpolarised inclusive electron scattering,” *Phys. Rev.* **C100**, 035201 (2019), [arXiv:1904.08016 \[hep-ph\]](#).
- [7] I. G. Aznauryan and V. D. Burkert, “Electroexcitation of nucleon resonances,” *Prog. Part. Nucl. Phys.* **67**, 1–54 (2012), [arXiv:1109.1720 \[hep-ph\]](#).
- [8] S. Alekhin, S. A. Kulagin, and R. Petti, “Modeling lepton-nucleon inelastic scattering from high to low momentum transfer,” *Proceedings, 5th International Workshop on Neutrino-Nucleus Interactions in the Few GeV Region (NuInt07): Batavia, USA, May 30-June 3, 2007*, *AIP Conf. Proc.* **967**, 215–224 (2007), [arXiv:0710.0124 \[hep-ph\]](#).
- [9] S. Alekhin, S. A. Kulagin, and R. Petti, “Update of the global fit of PDFs including the low- Q DIS data,” in *Proceedings, 16th International Workshop on Deep Inelastic Scattering and Related Subjects (DIS 2008): London, UK, April 7-11, 2008* (2008) p. 43, [arXiv:0810.4893 \[hep-ph\]](#).
- [10] B. L. Ioffe, V. A. Khoze, and L. N. Lipatov, *Hard Processes. Vol. 1: Phenomenology. Quark-Parton Model* (Elsevier Science Publishers B.V. (North-Holland Physics Publishing Division), 1984).
- [11] S. Alekhin, J. Blümlein, S. Moch, and R. Placakyte, “Parton distribution functions, α_s , and heavy-quark masses for LHC Run II,” *Phys. Rev. D* **96**, 014011 (2017), [arXiv:1701.05838 \[hep-ph\]](#).
- [12] H. Georgi and H. D. Politzer, “Freedom at moderate energies: masses in color dynamics,” *Phys. Rev.* **D14**, 1829 (1976).
- [13] S. A. Kulagin and R. Petti, “Global study of nuclear structure functions,” *Nucl. Phys.* **A765**, 126–187 (2006), [arXiv:hep-ph/0412425](#).
- [14] S. Kulagin, “Nuclear effects in the deuteron in the resonance and deep-inelastic scattering region,” *Phys. Part. Nucl.* **50**, 506–512 (2019), [arXiv:1812.11738 \[nucl-th\]](#).
- [15] J. D. Bjorken and J. D. Walecka, “Electroproduction of nucleon resonances,” *Annals Phys.* **38**, 35–62 (1966).
- [16] M. Tanabashi *et al.* (Particle Data Group), “Review of Particle Physics,” *Phys. Rev.* **D98**, 030001 (2018).
- [17] J. Cudell, V. Ezhela, K. Kang, S. Lugovsky, and N. Tkachenko (COMPAS Group, IHEP), “High-energy forward scattering and the pomeron: simple pole versus unitarized models,” *Phys. Rev. D* **61**, 034019 (2000), [Erratum: *Phys.Rev.D* 63, 059901 (2001)], [arXiv:hep-ph/9908218](#).
- [18] M. Arneodo *et al.* (New Muon), “Measurement of the proton and deuteron structure functions,

- F_2^p and F_2^d , and of the ratio σ_L/σ_T ,” Nucl. Phys. B **483**, 3–43 (1997), arXiv:hep-ph/9610231.
- [19] A. Benvenuti *et al.* (BCDMS), “A high statistics measurement of the proton structure functions $F_2(x, Q^2)$ and R from deep inelastic muon scattering at high Q^2 ,” Phys. Lett. B **223**, 485–489 (1989).
- [20] C. Adloff *et al.* (H1), “Deep inelastic inclusive ep scattering at low x and a determination of α_S ,” Eur. Phys. J. C **21**, 33–61 (2001), arXiv:hep-ex/0012053.
- [21] S. Chekanov *et al.* (ZEUS), “Measurement of the neutral current cross-section and F_2 structure function for deep inelastic $e + p$ scattering at HERA,” Eur. Phys. J. C **21**, 443–471 (2001), arXiv:hep-ex/0105090.
- [22] L. W. Whitlow, *Deep Inelastic Structure Functions From Electron Scattering on Hydrogen, Deuterium, and Iron at $0.6 \leq Q^2 \leq 30 \text{ GeV}^2$* , Ph.D. thesis, SLAC (1990).
- [23] Resonance Data, <https://hallcweb.jlab.org/resdata/database/>.
- [24] L. M. Stuart *et al.*, “Measurements of the $\Delta(1232)$ transition form-factor and the ratio σ_n/σ_p from inelastic electron-proton and electron-deuteron scattering,” Phys. Rev. **D58**, 032003 (1998), arXiv:hep-ph/9612416 [hep-ph].
- [25] M. Osipenko *et al.* (CLAS), “A kinematically complete measurement of the proton structure function F_2 in the resonance region and evaluation of its moments,” Phys. Rev. **D67**, 092001 (2003), arXiv:hep-ph/0301204 [hep-ph].
- [26] M. Osipenko *et al.*, “The proton structure function F_2 with CLAS,” (2003), arXiv:hep-ex/0309052 [hep-ex].
- [27] M. Osipenko, Private communication.
- [28] CLAS Physics Database, <https://clas.sinp.msu.ru/cgi-bin/jlab/db.cgi>.
- [29] Y. Liang *et al.* (Jefferson Lab Hall C E94-110), “Measurement of $R = \sigma_L/\sigma_T$ and the separated longitudinal and transverse structure functions in the nucleon resonance region,” (2004), arXiv:nucl-ex/0410027 [nucl-ex].
- [30] S. P. Malace *et al.* (Jefferson Lab E00-116), “Applications of quark-hadron duality in F_2 structure function,” Phys. Rev. **C80**, 035207 (2009), arXiv:0905.2374 [nucl-ex].
- [31] V. Tvaskis *et al.*, “Measurements of the separated longitudinal structure function F_L from hydrogen and deuterium targets at low Q^2 ,” Phys. Rev. **C97**, 045204 (2018), arXiv:1606.02614 [nucl-ex].
- [32] T. Armstrong *et al.*, “Total hadronic cross-section of gamma rays in hydrogen in the energy range 0.265 GeV to 4.215 GeV,” Phys. Rev. D **5**, 1640–1652 (1972).
- [33] M. MacCormick *et al.*, “Total photoabsorption cross-sections for ^1H , ^2H and ^3He from 200 to 800 MeV,” Phys. Rev. C **53**, 41–49 (1996).
- [34] H. Meyer, B. Naroska, J. Weber, M. Wong, V. Heynen, E. Mandelkow, and D. Notz, “Total cross section for photoproduction of hadrons on hydrogen and deuterium between 1.0 and 6.4 GeV,” Phys. Lett. B **33**, 189–192 (1970).
- [35] H. Hilpert *et al.*, “Total cross section for photoproduction of hadrons on protons up to 5 GeV,” Phys. Lett. B **27**, 474–476 (1968).
- [36] M. L. Perl, T. Braunstein, J. Cox, F. Martin, W. Toner, B. Dieterle, T. Zipf, W. Lakin, and H. C. Bryant, “Muon-proton inelastic scattering and vector dominance,” Phys. Rev. Lett. **23**, 1191–1194 (1969).
- [37] J. Ballam *et al.*, “Bubble chamber study of photoproduction by 2.8 and 4.7-GeV polarized photons. 1. Cross-Section Determinations and Production of ρ^0 and Δ^{++} in the reaction $\gamma p \rightarrow p\pi^+\pi^-$,” Phys. Rev. D **5**, 545 (1972).
- [38] H. Bingham *et al.*, “Total and partial γp cross-sections at 9.3 GeV,” Phys. Rev. D **8**, 1277

- (1973).
- [39] D. O. Caldwell, V. Elings, W. Hesse, R. Morrison, F. V. Murphy, and D. Yount, “Total hadronic photoabsorption cross-sections on hydrogen and complex nuclei from 4 to 18 GeV,” *Phys. Rev. D* **7**, 1362 (1973).
 - [40] D. O. Caldwell *et al.*, “Measurements of the photon total cross-section on protons from 18 to 185 GeV,” *Phys. Rev. Lett.* **40**, 1222 (1978).
 - [41] S. Michalowski, D. Andrews, J. Eickmeyer, T. Gentile, N. B. Mistry, R. Talman, and K. Ueno, “Experimental study of nuclear shadowing in photoproduction,” *Phys. Rev. Lett.* **39**, 737–740 (1977).
 - [42] G. Alexander, J. Gandsman, L. Jacobs, A. Levy, D. Lissauer, and L. Rosenstein, “Total and partial γd , γn and γp cross sections at 7.5 GeV,” *Nucl. Phys. B* **68**, 1–11 (1974).
 - [43] S. Aid *et al.* (H1), “Measurement of the total photon-proton cross-section and its decomposition at 200 GeV center-of-mass energy,” *Z. Phys. C* **69**, 27–38 (1995), arXiv:hep-ex/9509001.
 - [44] G. Vereshkov, O. Lalakulich, Y. Novoseltsev, and R. Novoseltseva, “Total cross section for photon nucleon interaction in the energy range $\sqrt{s} = 40 - 50$ GeV,” *Phys. Atom. Nucl.* **66**, 565–574 (2003).
 - [45] O. Bartalini *et al.*, “Measurement of the total photoabsorption cross section on a proton in the energy range 600 – 1500 MeV at the GRAAL,” *Phys. Atom. Nucl.* **71**, 75–82 (2008).
 - [46] F. James and M. Roos, “MINUIT - a system for function minimization and analysis of the parameter errors and correlations,” *Comput. Phys. Commun.* **10**, 343–367 (1975).
 - [47] Y. Liang, *Measurement of $R = \sigma_L/\sigma_T$ in the nucleon resonance region*, Ph.D. thesis, American Univ. (2003).
 - [48] A. Airapetian *et al.* (HERMES), “Inclusive measurements of inelastic electron and positron scattering from unpolarized hydrogen and deuterium targets,” *JHEP* **05**, 126 (2011), arXiv:1103.5704 [hep-ex].
 - [49] L. W. Whitlow, E. M. Riordan, S. Dasu, S. Rock, and A. Bodek, “Precise measurements of the proton and deuteron structure functions from a global analysis of the SLAC deep inelastic electron scattering cross-sections,” *Phys. Lett.* **B282**, 475–482 (1992).
 - [50] S. Malace, *Measurements of Inclusive Resonance Cross Sections for Quark-Hadron Duality Studies*, Ph.D. thesis (2006).
 - [51] S. Dasu *et al.* (E140), “Measurement of kinematic and nuclear dependence of $R = \sigma_L/\sigma_T$ in deep inelastic electron scattering,” *Phys. Rev. D* **49**, 5641–5670 (1994).
 - [52] L. H. Tao *et al.* (E140X), “Precision measurement of $R = \sigma_L/\sigma_T$ on hydrogen, deuterium and beryllium targets in deep inelastic electron scattering,” *Z. Phys. C* **70**, 387–390 (1996).
 - [53] K. Abe *et al.* (E143), “Measurements of $R = \sigma_L/\sigma_T$ for $0.03 < x < 0.1$ and fit to world data,” *Phys. Lett. B* **452**, 194–200 (1999), arXiv:hep-ex/9808028.
 - [54] E. D. Bloom and F. J. Gilman, “Scaling, duality, and the behavior of resonances in inelastic electron-proton scattering,” *Phys. Rev. Lett.* **25**, 1140 (1970).